

# JOURNAL OF MECHANICAL ENGINEERING

*An International Journal*

Vol 17 (1)	01 April 2020	ISSN 1823-5514	eISSN 2550-164X
------------	---------------	----------------	-----------------

1	<a href="#">Experimental Electrical Characterisation of Thermoelectric Generator using Forced Convection Water Cooling</a> <i>Raihan Abu Bakar*, Baljit Singh, Muhammad Fairuz Remeli, and Ong Kok Seng</i>	1
2	<a href="#">Development of a System to Control Flow of Coolant in Turning Operation</a> <i>Rajesh Kumar Maurya*, M. S. Niranjana, Nagendra Kumar Maurya, and Shashi Prakash Dwivedi</i>	17
3	<a href="#">Effect of Process Parameters on Surface Roughness in HPC Drilling of AISI 1055 Steel</a> <i>H.V. Shete* and M.S. Sohani</i>	32
4	<a href="#">Design and Development of the Front Wheel Hub for All-Terrain Vehicle (ATV)</a> <i>Himanshu Verma, Sandeep Kumar, Rabinder Singh Bharj, and Rajan Kumar*</i>	49
5	<a href="#">Comparative Study on CI Engine Performance and Emissions using a Novel Antioxidant Additive</a> <i>N Kapilan*</i>	63
6	<a href="#">Experimental Study on Translation Motion Characteristics of Moored Symmetrical Semi-submersible in Regular Waves</a> <i>Khairuddin, N.M.*, Jaswar Koto, NurAin, A.R., Mohd Azhari, J., and Najmie, A.</i>	77
7	<a href="#">Spiral Toolpath Definition and G-code Generation for Single Point Incremental Forming</a> <i>Zeradam Yeshiwas* and A. Krishniah</i>	91
8	<a href="#">Reduction of Copper to Steel Weld Ductility for Parts in Metallurgical Equipment</a> <i>Mohammad E. Matarneh*, Nabeel S. Gharaibeh, Valeriy V Chigarev, and Havrysh Pavlo Anatoliiovych</i>	103
9	<a href="#">ANFIS Model for Prediction of Performance-Emission Paradigm of a DICl Engine Fueled with the Blends of Fish Oil Methyl Ester, n-Pentanol and Diesel</a> <i>Kiran Kumar Billa*, G.R.K. Sastry, and Madhujit Deb</i>	115

10	Fatigue Life Assessment Approaches Comparison Based on Typical Welded Joint of Chassis Frame <i>Maksym Starykov*</i>	135
----	--	-----

# Experimental Electrical Characterisation of Thermoelectric Generator using Forced Convection Water Cooling

*Raihan Abu Bakar\*, Baljit Singh, Muhammad Fairuz Remeli*  
Faculty of Mechanical Engineering  
Universiti Teknologi MARA, Shah Alam, Malaysia  
\*master\_raikun8@yahoo.com

*Ong Kok Seng*  
Faculty of Engineering and Green Technology  
Universiti Tunku Abdul Rahman, Kampar, Malaysia

## ABSTRACT

*Thermoelectric Generator (TEG) provides unique advantages as compared to other heat engines as it is capable to convert heat to electricity directly without having any moving parts. Furthermore, TEG is compact, simple and noiseless and requires very minimal maintenance. This paper presents an experimental and analytical study of a model consisting of a TEG located between a copper water cooling jacket and an aluminium block which acts as a heat spreader. The copper water cooling jacket was used in this study as water has higher thermal capacity than air. Besides, copper is one of highest thermal conductivity materials. TEG characterisation in term of electrical was investigated in this study. Based on the result, it shows a linear proportion relationship between open-circuit voltage and temperature difference across TEG. The result also clearly shows the power output of TEG increases as the temperature gradient across TEG increases. In addition, the impact of water flowrate on TEG power output was also studied. Based on the finding, there was an optimum water flowrate of 80 ml/s. Further increasing the water flowrate is not favourable as it will not increase power output and may lead to higher pumping power for water circulation. At this optimum water flowrate, the maximum power output obtained is equal to 530 mW when TEG hot-side temperature ( $T_h$ ) is 180 °C.*

**Keywords:** Power Generation; Thermoelectric Generator; Water Flowrate, Characterisation.

## Nomenclature

$I_L$	Total current drawn in the circuit
$P_{max}$	Maximum TEG power output
$P_{TEG}$	TEG power output
$P_{TEG-exp}$	TEG power output obtained through experiment
$Q_c$	Heat transfer rate at TEG cold-side
$Q_h$	Heat transfer rate at TEG hot-side
$R_{TEG}$	TEG electrical internal resistance
$R_L$	External load resistance
$T_c$	TEG cold-side temperature
$T_h$	TEG hot-side temperature
$t$	Time
$V_{ac-o}$	Output voltage of AC variable transformer
$V_{oc}$	TEG open circuit voltage
$V_w$	Water flowrate
$\alpha_{TEG}$	TEG Seebeck coefficient
$\alpha_{TEG-exp}$	TEG Seebeck coefficient obtained through experiment
$\alpha_{wire}$	Seebeck coefficient of volt measuring probe wire
$\Delta T_{TEG}$	Temperature gradient across TEG
$\kappa_{TEG}$	TEG thermal conductance
$v_b$	Bottle volume

## Introduction

Electricity plays a vital role in our daily lives. From providing means of basic necessities such as cooking, heating and cooling to luxury and entertainment which include powering home appliances such as televisions and smart phones. Electricity generation mainly comes from thermal power plants and these power plants burn fossil fuels such as coal and gas to produce electricity [1]. These fossil fuels are not only non-renewable, they also contribute towards global warming.

Furthermore, by using Rankine Cycle or Kalina Cycle, these thermal power plants require intermediate-to-high grade heat to convert into mechanical energy and eventually to produce electricity by rotating turbines and generators. Thermal power plants which harness low grade heat may be possible but it is not economical since there are many equipments and complex system required to convert heat to electricity.

Thermoelectric Generator (TEG) provides a best solution to this, as it is able to harness low grade heat to produce electricity directly with the Seebeck Effect. As shown in Figure 1, two dissimilar thermoelectric materials (p-type and n-type semiconductors) are being sandwiched between two ceramics.

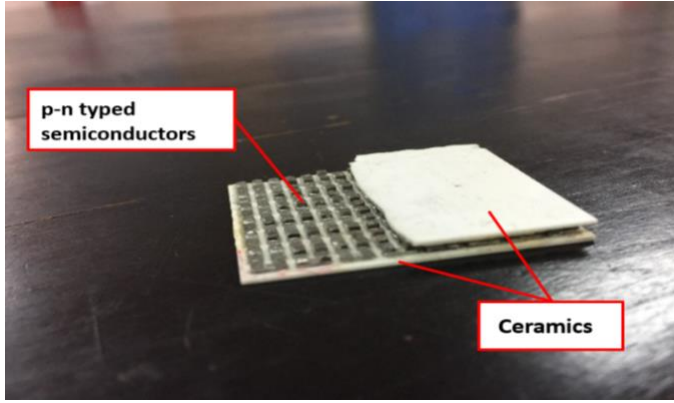


Figure 1: Thermoelectric Generator

While thermal power plants require large space and equipment such as boilers, combustion chambers and turbines to generate electricity, TEG does not require these equipment to generate electricity. In addition, TEG is simple and compact, noiseless, and it requires very minimal maintenance as no moving parts is involved [2].

Nevertheless, the common problems arising with TEG is low power output as well as low electrical efficiency [2]–[7]. TEG material performance is associated with its dimensionless figure of merit:

$$ZT = \frac{\alpha^2}{\kappa\lambda} T \quad (1)$$

where  $\alpha$ ,  $\kappa$ ,  $\lambda$ ,  $T$  are Seebeck coefficient, thermal conductivity, electrical resistivity and absolute temperature respectively. Low  $ZT$  value produces low electrical efficiency and vice versa.

Because of these problems, the use of TEG has been limited to certain applications such as in remote and extreme remote conditions (space exploration), and also in waste-heat recovery [6]. Radioisotope Thermoelectric Generator (RTG) is used in powering two space crafts namely Voyager 1 and 2 started since 1977 until now [8]. RTG produced 158 W at the early stage of the mission. Amerigon, together with its partners (BMW and Fords) carried out a TEG research program for seven years [9]. At the research final stage, they conducted a road test of a cylindrical TEG on two vehicles namely BMW X6 and Lincoln MKT vehicles. Around 450W of power output was obtained as a result of the road test [9].

Nevertheless, numerous studies were carried out to increase TEG efficiency. One of methods is to increase  $ZT$  value by performing rare earth

element doping on TEG material. Ivanov et al. [10] investigated Lu and Tm doping effect and TEG performance. The doping result showed a significant increase of  $ZT$  value. Meanwhile, Zianni [11] demonstrated  $ZT$  enhancement by proposing width-modulated Si nanowires. The author found out as a constriction width (which modulates the nanowire) decreased,  $ZT$  value of modulated nanowires increased remarkably.

Most of the time, power output produced by TEG depends on the temperature gradient across it. The higher the temperature gradient, the higher the power output produced by TEG. Kiflemariam and Lin [12] researched the self-cooling mechanism for an array of TEG modules. The power generated by TEGs is able to run a fan which cools down the device temperature up to 20%. Tu et al. [13] explored utilising phase change material (PCM) on TEG for space exploration application purpose. Under a wide range of temperature (from +100°C to -50°C), the researched showed that 32.32% increase of total power output by using paraffin/5% wt% EG composite. El-Adl et al. [14] investigated passively cooled techniques on TEG performance. These techniques are free convection (FC), passive water cooling (PWC) and vapor phase change cooling (VPC). It was observed that VPC with fins resulted the best performance whereas FC without fins resulted the worst performance. On using different type of cooling fluid besides air and water, a study was conducted by Karana and Sahoo [15] on the impact of two nanofluid coolants on TEG performance for automobile waste heat recovery application. By using MgO nanofluid and ZnO nanofluid, power output improved by 11.38% and 9.86% respectively than using EG-W as coolant. Rezanian et al. [16] studied the coolant flowrates on power output of a TEG with micro channel heat sink. There is an optimum flowrate which resulted in maximum net power (the difference between TEG power output and pumping power). Singh et al. [4] performed a similar indoor experiment to determine optimum parameters for TEG performance. They achieved TEG performance of 4.19W power output and 2.62% efficiency at temperature difference of 94.55°C and 245.25 kPa compressive force.

Based on the previous literatures, to the best of our knowledge, there is a lack of study in determining an optimum water flowrate in TEG electrical characterisation test. Therefore, in this study, the test was carried out by varying water flowrate to determine the optimum water flowrate. Besides, a theoretical model was established to predict the TEG power output. The TEG characterisation test was carried out through a controlled and indoor experiment. In this study, a copper water cooling jacket was used as TEG heat sink. This is due to the fact that water has higher heat capacity than air [17]. Besides, copper is one of highest thermal conductivity materials [18]. In addition, the impact on TEG power output and characteristics was evaluated with broader ranges of water flowrate and temperature difference across TEG as compared to smaller ranges in the study carried out by Singh et al. [4].

## Methodology

### Design

Figure 2 shows a schematic design of proposed TEG characterisation experiment. In this experiment, a TEG was placed between a copper water cooling jacket and an aluminium block. The aluminium block, inserted with two cartridge heaters, acts to spread heat to the hot side of TEG uniformly. The cartridge heaters are connected in parallel to an AC variable transformer. Temperature input of cartridge heaters was varied by varying output voltage of AC variable transformer. Small protrusions were made on top of aluminium block in order to prevent the TEG from sliding on the block surface, thus effective heating can be achieved. The copper water cooling jacket was placed on top of TEG and the water flowed continuously through it. Thermal paste was applied between TEG and aluminium block to increase heat conduction by reducing thermal contact resistance.

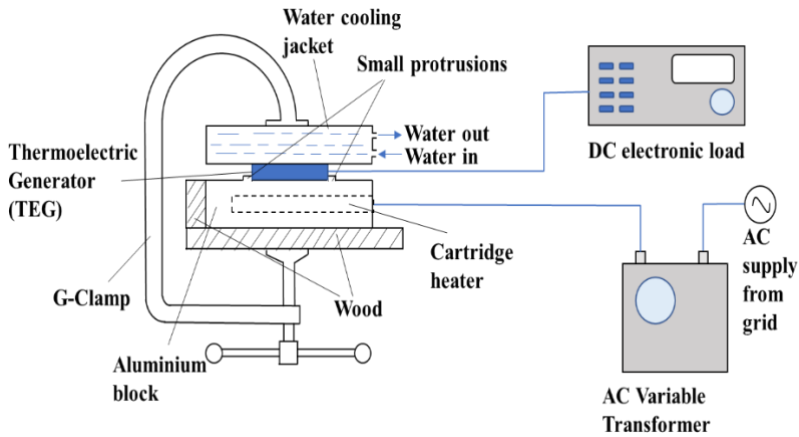


Figure 2: A schematic design of proposed TEG characterisation experiment

### Mathematical Model

A mathematical model was developed to analyse the performance of TEG. Several assumptions were made for a simplification purpose:

- 1) Thermal contact resistances between aluminium block and TEG and between TEG and water-cooling jacket are neglected
- 2) Heat loss due to convection and radiation is negligible

- 3) The Seebeck coefficient, thermal conductivity and electrical resistivity of TEG are assumed to be constant; the influence of temperature change is neglected.

The amount of heat transferred to the hot side of TEG is defined [2] as follows:

$$Q_h = \alpha_{TEG} I_L T_h - \frac{I_L^2 R_{TEG}}{2} + \kappa_{TEG} \Delta T_{TEG} \quad (2)$$

Whereas, the amount of heat transferred from the cold side of TEG is defined [2] as follows:

$$Q_c = \alpha_{TEG} I_L T_c - \frac{I_L^2 R_{TEG}}{2} + \kappa_{TEG} \Delta T_{TEG} \quad (3)$$

By applying energy conservation principle and assuming no heat loss surrounding, an energy balance equation can be written as:

$$Q_h = Q_c + P_{TEG} \quad (4)$$

Equation (4) can be rewritten as follows:

$$P_{TEG} = Q_h - Q_c \quad (5)$$

Substituting Equation (2) and Equation (3) into Equation (5), TEG power output can be expressed as:

$$P_{TEG} = \alpha_{TEG} I_L \Delta T_{TEG} - I_L^2 R_{TEG} \quad (6)$$

From Equation (6),  $P_{TEG}$  is a function of  $I_L$ ; the value of  $I_L$  determines the value of  $P_{TEG}$ . The values of  $I_L$  were obtained from by varying  $R_L$  using DC electronic load.

As mentioned in [19, 20], the experimental value of Seebeck coefficient of TEG ( $\alpha_{TEG-exp}$ ) can be obtained by using Equation (7) below:

$$\alpha_{TEG-exp} = \frac{V_{OC}}{\Delta T_{TEG}} - \alpha_{wire} \quad (7)$$

However, for simplicity reason,  $\alpha_{wire}$  is assumed to be negligible and Equation (7) reduced to Equation (8):

$$\alpha_{TEG-exp} = \frac{V_{OC}}{\Delta T_{TEG}} \quad (8)$$



The value of TEG internal resistance ( $R_{TEG}$ ) is equal to load resistance when power output is maximum. By differentiating an equation of experimental power of TEG ( $P_{TEG-exp}$ ), which is obtained experimentally and equalizing it to zero, the corresponding voltage and current can be determined. Therefore,  $R_{TEG}$ :

$$R_{TEG} = \frac{V}{I} \quad (9)$$

## Procedure

In order to validate the mathematical model developed in previous section, an experimental set up was built, as shown in Figure 3.

As shown in Figure 4, TEG used in this experiment is Bismuth Telluride with 127 number of junctions. The Bismuth Telluride Seebeck coefficient of one p-n couple is around  $190\mu V/K$  [4,21], thus TEG Seebeck coefficient ( $\alpha_{TEG}$ ) is equal to  $0.0241V/K$ . The TEG dimension is 40 mm (length), 40 mm (width) and 3.2 mm (thickness). The TEG is connected to a DC electronic load. By varying load resistance ( $R_L$ ) from  $0\ \Omega$  to  $900\ \Omega$  through the DC electronic load, the voltage and current outputs produced by TEG were also varied. Meanwhile, the copper water cooling jacket used in this experiment is shown in Figure 5.

Water flowed from the nearest water tap into the water-cooling jacket and flowed out to the sink. Water flowrate was varied according to the opening water tap valve. The calculation of water flowrate is based on how long it takes to fill up one 0.5 litre bottle. Time measurement were recorded and repeated for 5 times in order to obtain accurate average time. Table 1 below shows the details of the water flowrate calculation. Six thermocouples were placed at six different locations to measure the temperature at these locations, as illustrated in Figure 6.

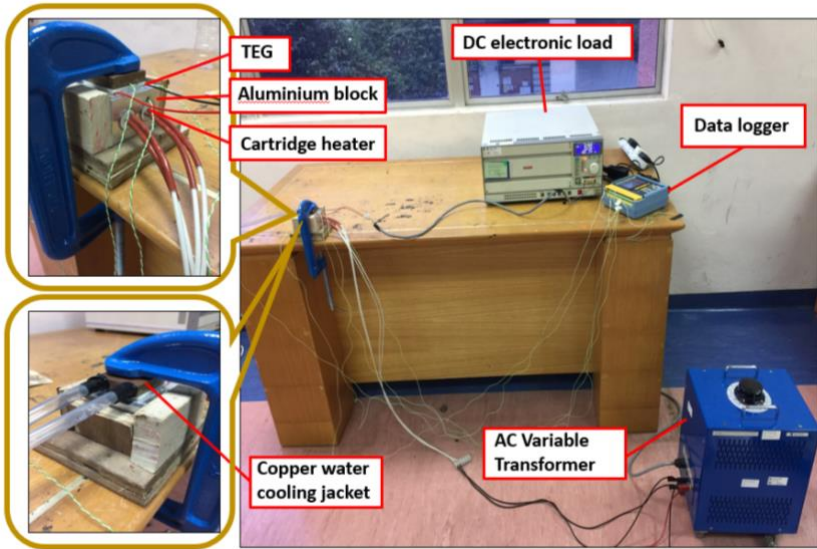


Figure 3: Experimental set up

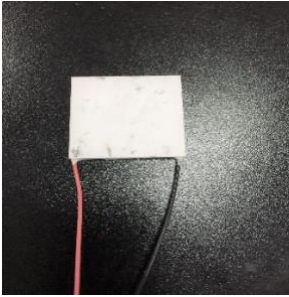


Figure 4: TEG  
(TEC1-12710T125)



Figure 5: Copper water  
cooling jacket

Table 1: Water flowrate calculation

Valve Opening	25%	50%	75%	100%
Volume, $v_b$ (litre)	0.5	0.5	0.5	0.5
Average Time, $t$ (s)	32.33	10.27	6.26	4.47
Flowrate, $V_w$ (l/s)	0.015	0.049	0.080	0.112
Flowrate, $V_w$ (ml/s)	15	49	80	112

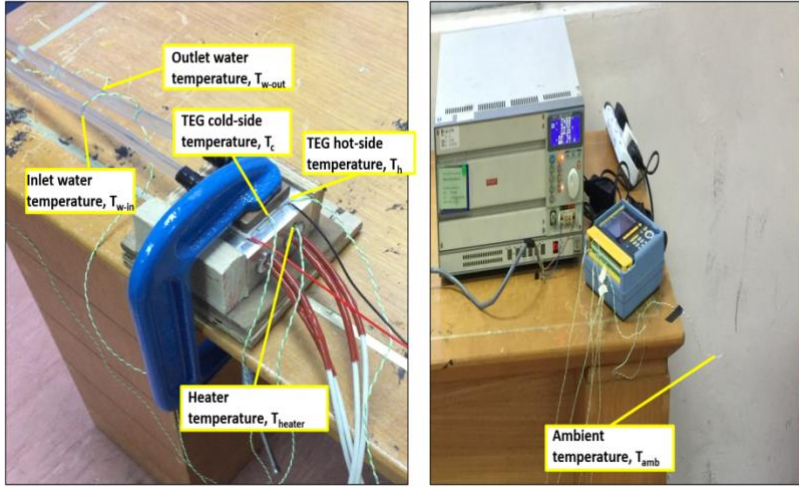


Figure 6: Six different locations of thermocouples

The experiment started by setting output voltage of AC variable transformer ( $V_{ac-o}$ ) to 60V and with the 25% tap valve opening. Sufficient times were taken to allow all the temperatures to reach steady state condition. Once they reached the steady state condition, all six temperature values were recorded. Also, an open-circuit voltage produced by TEG,  $V_{oc}$  (no load condition) was measured.

Then, the load resistance was varied from  $0 \Omega$  to  $900 \Omega$  by using the DC electronic load and the corresponding voltage and current were recorded. These steps repeated with 50%, 75% and 100% tap valve openings. Finally, the whole experiment was repeated for  $V_{ac-o} = 76V, 80V$  and  $100V$ .

## Results and Discussion

Figure 7 illustrates the current and power output curves when the load resistance was varied from  $0 \Omega$  to  $900 \Omega$  at TEG hot side temperature,  $\Delta T_{TEG} = 53^\circ C$  and water flowrate,  $V_w = 15 \text{ ml/s}$ . As load resistance increases, the voltage increases whereas the current produced decreases. This inverse linear relationship is clearly shown in Figure 7. The value of experimental power is a product of voltage and current. Power output as a function of voltage is a polynomial curve.

As mentioned in Mathematical Model section, power is maximum when TEG's internal resistance is equal to load resistance. Thus, differentiating an equation  $P_{TEG-exp} = -0.0004549V^2 + 0.5504623V + 2.1109526$  and equalizing it to zero,  $V$  is equal to 605 mV. Corresponding

current value can be determined plugging 605 mV into the equation  $I = -0.000505V + 0.610009$ , which is equal to 0.305 A. Thus, by using Equation (9),  $R_{TEG}$  value was obtained and is equal to  $1.98 \Omega$ .

These  $R_{TEG}$  and  $\alpha_{TEG}$  values, together with the corresponding current and temperature difference across TEG, were inserted into Equation (6) to obtain theoretical power output. Theoretical power was also plotted in the same graph, as illustrated in Figure 7. It is clearly shown that both theoretical power and experimental power curves are in good agreement. The maximum deviation between these two curves is about 4.05%. This small deviation is probably due to negligence on heat loss to surrounding.

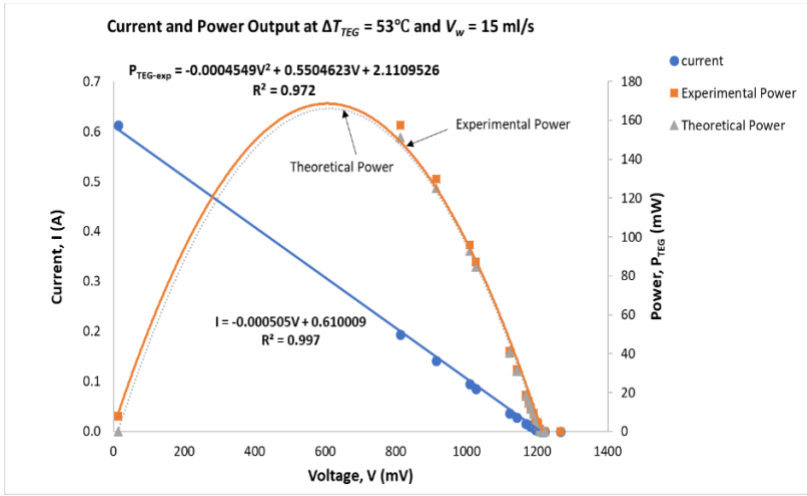


Figure 7: Current and power versus voltage at  $\Delta T_{TEG} = 53 \text{ }^{\circ}\text{C}$  and  $15 \text{ ml/s}$ .

Figure 8 shows the effect of water flowrate on power output at different TEG hot-side temperatures. These four graphs in Figure 8 clearly reveal that as water flowrate increases, the power output increases too. However, as water flowrate increases from  $80 \text{ ml/s}$  to  $112 \text{ ml/s}$ , an increase in power output is very minimal. Hence, it can be deduced that the optimum water flowrate for this experiment model is  $80 \text{ ml/s}$ . Further increasing water flowrate will not increase power output. Moreover, it will also cause a negative effect such as higher pumping power for water to circulate. The highest power achieved with this optimum water flowrate at  $T_h = 180 \text{ }^{\circ}\text{C}$  is equal to  $530 \text{ mW}$ .

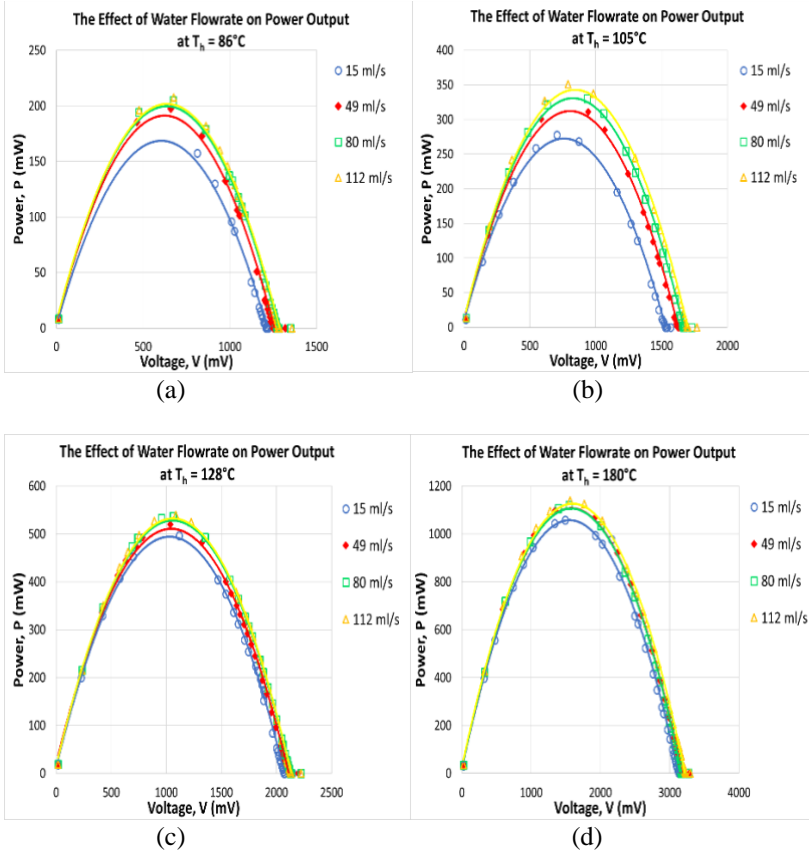


Figure 8: The effect of water flowrate on power output at different TEG hot-side temperatures (a)  $T_h = 86^\circ\text{C}$ , (b)  $T_h = 105^\circ\text{C}$ , (c)  $T_h = 128^\circ\text{C}$ , and (d)  $T_h = 180^\circ\text{C}$ .

Figure 9 illustrates current and power curves with four different temperature gradients across TEG at water flowrate,  $V_w = 15\text{ ml/s}$ ,  $49\text{ ml/s}$ ,  $80\text{ ml/s}$  and  $112\text{ ml/s}$ . As shown in Figure 9(a), as temperature difference across TEG ( $\Delta T_{\text{TEG}}$ ) increases, current and power output produced by TEG also increase. This is also true for other  $V_w$  values which are shown in Figure 9(b), 9(c) and 9(d). All I-V curves in Figure 9 have the same slope with very small errors. This means the TEG internal resistance remains constant with different values of hot side temperature and load resistance.

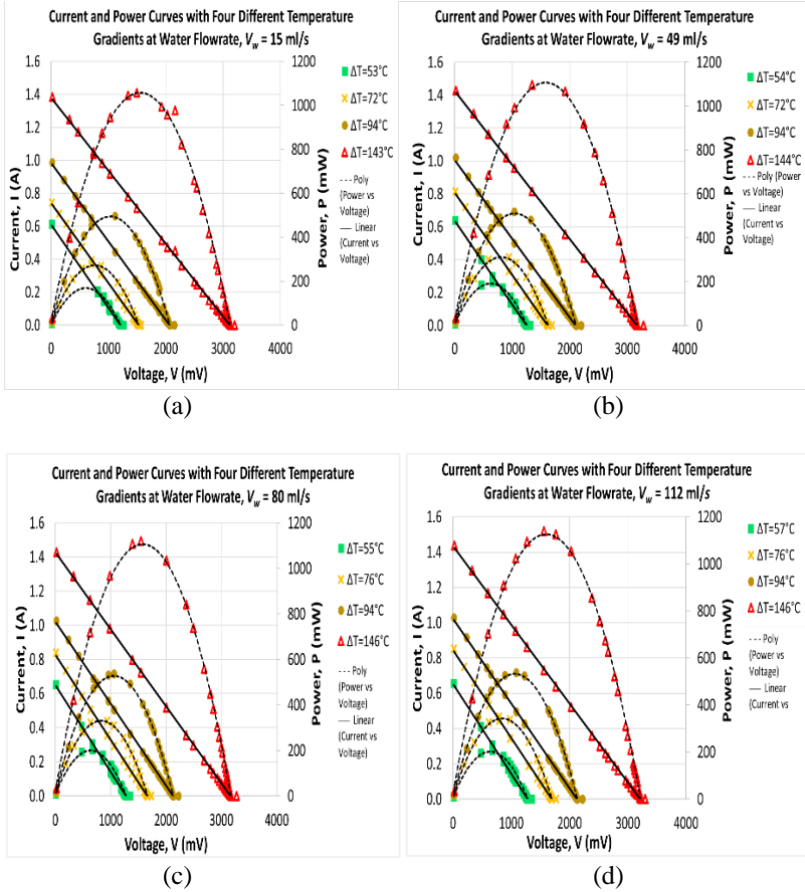


Figure 9: Current and power curves with four different temperature gradients across TEG at different water flowrates (a)  $V_w = 15$  ml/s, (b)  $V_w = 49$  ml/s, (c)  $V_w = 80$  ml/s, and (d)  $V_w = 112$  ml/s.

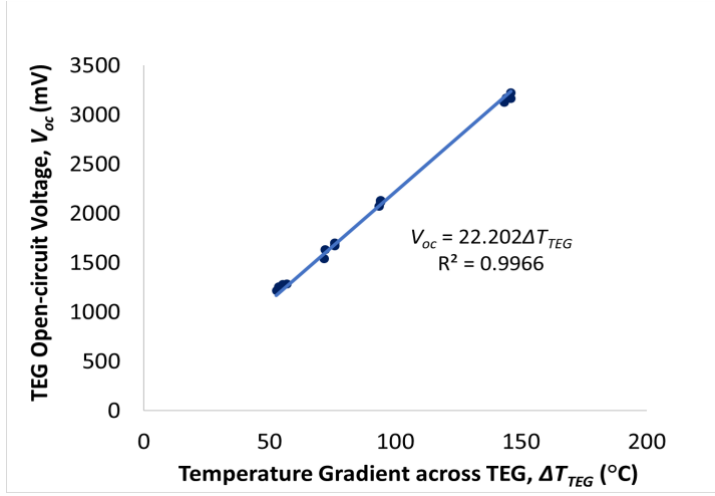


Figure 10: Open-circuit voltage versus temperature difference across TEG.

Figure 10 shows a linear curve of TEG open-circuit voltage ( $V_{oc}$ ) versus temperature difference across TEG ( $\Delta T_{TEG}$ ). As  $\Delta T_{TEG}$  increases,  $V_{oc}$  also increases linearly.

Figure 11 shows the values of experimental value of TEG Seebeck coefficient  $\alpha_{TEG-exp}$  versus  $\Delta T_{TEG}$ . These  $\alpha_{TEG-exp}$  values obtained by dividing  $V_{oc}$  with  $\Delta T_{TEG}$ , which are shown in Figure 10. As illustrated in Figure,  $\alpha_{TEG-exp}$  values range from 0.0215 V/K to 0.0236 V/K. This inconsistency is probably due to the fact that Seebeck coefficient varies with temperature [19]–[21]. Also, the estimated Seebeck coefficient value of 0.0241 V/K which was stated previously in Procedure Section is slightly near to this range. Such difference is probably due to previous assumption was made in neglecting the Seebeck effect of volt measuring probe wires. As shown in Equation (7), the estimated Seebeck coefficient value (0.0241 V/K) would have been a bit lower if the Seebeck effect of volt measuring probe wires was taken into consideration.

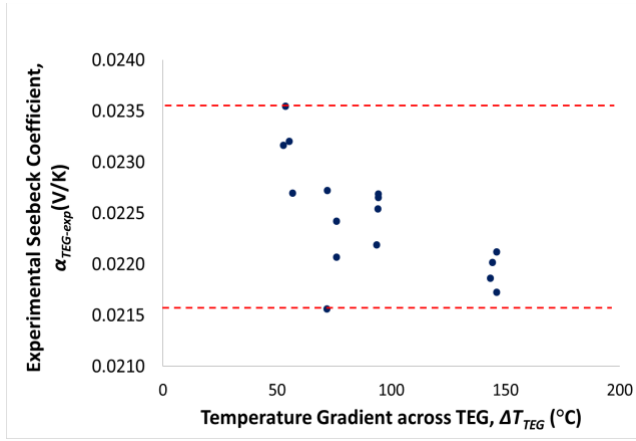


Figure 11: Experimental Seebeck Coefficient versus Temperature Gradient across TEG

Figure 12 illustrates TEG maximum power output,  $P_{max}$  versus  $\Delta T_{TEG}$ . As  $\Delta T_{TEG}$  increases,  $P_{max}$  increases exponentially. A trend line with the following equation was shown in Figure 12 can be used to predict the  $P_{max}$  value with a known  $\Delta T_{TEG}$  value.

$$P_{max} = 0.0001\Delta T_{TEG}^{1.8067} \quad (10)$$

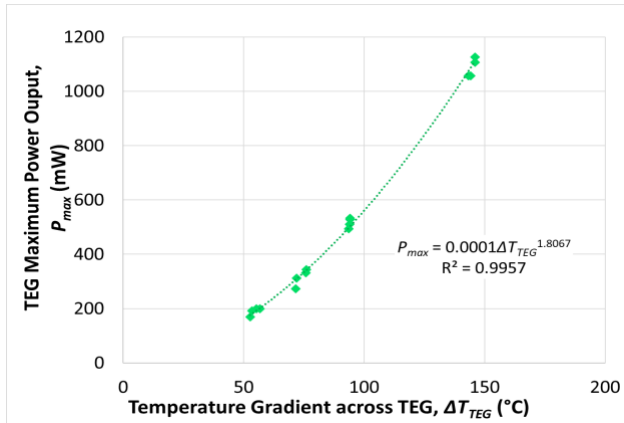


Figure 12: TEG Maximum Power Output,  $P_{max}$  versus Temperature Gradient across TEG,  $\Delta T_{TEG}$



## Conclusion

An experimental setup with one TEG located between a copper water cooling jacket and an aluminium block which acts as a heat spreader was proposed in this study. TEG characterisation in term of electrical characteristics was investigated. The result obtained shows power output by TEG increases as temperature difference across TEG increases. In addition to this, the theoretical power output is also validated with experimental power output, with a maximum difference of 4.05%. Moreover, from this experiment result, we can also conclude that as water flowrate increases, the power output also increases up to a certain flowrate where the power output remains constant. This optimum water flowrate is equal to 80 ml/s. Further increasing water flowrate will not give any advantages on power output. The maximum power achieved with this optimum water flowrate is equal to 530mW when  $T_h = 180^\circ\text{C}$ .

## References

- [1] Agency for Natural Resources and Energy, “Key World Energy Statistics,” (2017).
- [2] L. J. and K. C. L. Kok S. Ong, “Thermoelectric Energy Conversion,” 1, 1–8 (2018).
- [3] W. H. Chen, C. Y. Liao, C. I. Hung, and W. L. Huang, “Experimental study on thermoelectric modules for power generation at various operating conditions,” *Energy* 45 (1), 874–881 (2012).
- [4] B. Singh, T. Lippong, A. Date, and A. Akbarzadeh, “The effects of temperature difference and compressive force to the electrical characterization of peltier cell for artificial concentrated solar power thermoelectric application,” *J. Mech. Eng.* 11 (1), 15–30 (2014).
- [5] D. S. Patil, R. R. Arakerimath, and P. V. Walke, “Thermoelectric materials and heat exchangers for power generation – A review,” *Renew. Sustain. Energy Rev.* 95 (June), 1–22 (2018).
- [6] D. Champier, “Thermoelectric generators: A review of applications,” *Energy Convers. Manag.* 140, 167–181 (2017).
- [7] G. Liang, J. Zhou, and X. Huang, “Analytical model of parallel thermoelectric generator,” *Appl. Energy*, 88 (12), 5193–5199 (2011).
- [8] “Legacy Power Systems | Power and Thermal Systems – NASA Radioisotope Power Systems.” [Online]. Available: <https://rps.nasa.gov/power-and-thermal-systems/legacy-power-systems/>. [Accessed: 17-May-2018].
- [9] D. Crane and J. Lagrandeur, “Thermoelectric Generator Performance for Passenger Vehicles,” 1–28 (2012).
- [10] O. Ivanov, M. Yaprincev, R. Lyubushkin, and O. Soklakova,

- “Enhancement of thermoelectric efficiency in Bi<sub>2</sub>Te<sub>3</sub> via rare earth element doping,” *Scr. Mater.* 146, 91–94 (2018).
- [11] X. Zianni, “Designing width-modulated Si nanowires for enhanced thermoelectric efficiency,” *Microelectron. Eng.* 159, 51–54 (2016).
  - [12] R. Kiflemariam and C. X. Lin, “Experimental investigation on heat driven self-cooling application based on thermoelectric system,” *Int. J. Therm. Sci.* 109, 309–322 (2016).
  - [13] Y. Tu, W. Zhu, T. Lu, and Y. Deng, “A novel thermoelectric harvester based on high-performance phase change material for space application,” *Appl. Energy* 206 (October), 1194–1202 (2017).
  - [14] A. S. El-Adl, M. G. Mousa, and A. A. Hegazi, “Performance analysis of a passively cooled thermoelectric generator,” *Energy Convers. Manag.* 173 (March), 399–411 (2018).
  - [15] D. R. Karana and R. R. Sahoo, “Effect on TEG performance for waste heat recovery of automobiles using MgO and ZnO nanofluid coolants,” *Case Stud. Therm. Eng.* 12, 358–364 (2018).
  - [16] A. Rezaia, L. A. Rosendahl, and S. J. Andreasen, “Experimental investigation of thermoelectric power generation versus coolant pumping power in a microchannel heat sink,” *Int. Commun. Heat Mass Transf.* 39 (8), 1054–1058 (2012).
  - [17] “Heat capacity.” [Online]. Available: [https://en.wikipedia.org/wiki/Heat\\_capacity](https://en.wikipedia.org/wiki/Heat_capacity).
  - [18] H. D. Young, *University Physics*, 7th ed. (1992).
  - [19] Z. Zhou and C. Uher, “Apparatus for Seebeck coefficient and electrical resistivity measurements of bulk thermoelectric materials at high temperature,” *Rev. Sci. Instrum.* 76 (2), (2005).
  - [20] B. Paul, “Simple apparatus for the multipurpose measurements of different thermoelectric parameters,” *Meas. J. Int. Meas. Confed.* 45 (1), 133–139 (2012).
  - [21] J. Tan *et al.*, “Thermoelectric properties of bismuth telluride thin films deposited by radio frequency magnetron sputtering,” 5836, 711–718 (2005).

# Development of a System to Control Flow of Coolant in Turning Operation

Rajesh Kumar Maurya<sup>1\*</sup>, M. S. Niranjana<sup>2</sup>, Nagendra Kumar Maurya<sup>1</sup>,  
Shashi Prakash Dwivedi<sup>1</sup>

<sup>1</sup>GL Bajaj Institute of technology & management, Greater Noida, India.

<sup>2</sup>Delhi Technological University Delhi -110042, India.

\*raj06mry@gmail.com

## ABSTRACT

*Automation of cooling system in machine tools is an effective method for achieving higher productivity and increased tool life. A cooling system is designed to control the operating temperature on the cutting tool tip by circulating coolant through a reservoir built on the top of the machine tool. This arrangement maintains the coolant flow rate as per variation of cutting tool tip temperature sensed by LM-35 temperature sensor which is located 1 cm away (calibrated distance) from the cutting tool tip and whose output voltage is linearly proportional to the temperature. Coolant flow rate is varied in such a manner that the temperature of the cutting tool tip remains within fixed value of temperature. The aim of present work is to develop a cooling control panel system to provide coolant on cutting tool tip in turning operation of mild steel. The coolant flow rate can be increased or decreased as per the variation of sensor temperature during turning of mild steel with high speed steel (HSS) cutting tool at different depth of cut, and spindle speed, keeping feed rate constant which results in effective cooling of the cutting tool tip. The experiments were carried out with and without use of coolant. It supplies the coolant as per instructions of cooling control panel system which results in saving of coolant as well as power. The mechatronics application of designed cooling control panel system enabled the reduction in cutting tool tip temperature in more robust way as compare to conventional cooling system.*

**Keywords:** Centre Lathe; Cutting Tool, Cooling Control Panel System; Coolant; Temperature Sensor

## Introduction

The challenges in machining are to achieve high dimensional accuracy of work part, surface finish, high production rate, less environmental effect as well as cost saving. These responses are strongly influenced by various machining factors such as tool geometry and work-piece material, turning process parameters, cutting tool material, coolant etc [1]. Hasib et al. [2] have observed that the main functions of coolant in machining are to reduce the friction at the interface of tool –chip and tool workpiece, cool both chip and tool as well as to remove the chip.

In turning operation, high temperature is generated which causes various problems like high tool wear in high heat affected zone, change in hardness, as well as work-piece microstructure, burning and micro-cracks. The problems of temperature raised could be reduced through the application of cutting fluid by conventional methods. But in conventional method, it can reduce in some extent through cooling in cutting zone because cooling rate is very low. Thus, for increasing the cooling rate the researchers have focus on alternative method instead of traditional flood cooling. The alternative technique referred as mist application of cutting fluid also known near dry machining.

This method can reduce the use of coolant which leads to environment friendly as well as economic benefits. The turning operation has been carried out in dry, flood and mist condition of cutting fluids. It has been seen that the mist application reduced 40% more tool-chip interface temperature than the conventional cooling methods. Benedicto et al. [3] have observed the application of coolants in machining process which is a matter of serious concern in terms of cost, environment and health issue. The alternative use of cutting fluid such as solid lubricants, cryogenic cooling, gaseous cooling, use of vegetables oil for cooling and Minimum Quantity Lubrication (MQL) in which oil is mixed with compressed air and uses in the form of drops or spray in the cutting zone which can reduce the environment and health issue.

In Oda et al. [4], the aim of this paper is to reduce power consumption by improving the machining process. Here it has been described that in machining process about 54% of total energy is consumed due to coolant related equipment. To reduce the energy consumption efforts are totally concentrated on coolant related equipments which caused the saving of energy approximately by 26%. Nandgaonkar et al. [5] explained the concept of water oil mist spray (WOMS) for cooling in machining as compare to MQL in which air is mixed with oil. It has been found that the use of (WOMS) causes better cooling as well as better tool life. Attanasio et al. [6] found that the use of MQL causes reduction in cutting fluid. When it is applied on rake face of tool, it does not produce the reduction of wear and same as in case of dry machining. When it is applied on flank surface it shows the appropriate reduction in tool wear as compare to dry condition.

Dhar et al. [7] paper deals with the use of MQL as coolant for turning of AISI-4340 steel at different speed-feed combination. Use of this technique causes a significant reduction in cutting temperature, tool wear and surface roughness as compare to the conventional cooling and dry conditions. Dhar et al. [8] have observed that in high production machining the application of conventional cooling is not suitable in terms of cooling, tool wear, and surface finish. The use of MQL shows significant results over the mentioned responses. Dhar et al. [9] work deals with the use of cryogenic cooling by liquid nitrogen jet in turning of AISI-4037 steel.

There are several benefits of using cryogenic as a coolant in turning zone as compare to the conventional flooded cooling and dry conditions. It has been seen that the use of liquid nitrogen jet on turning zone cause good reduction in cutting temperature, tool wear. It also provides good surface finish and better dimensional accuracy. The use of cryogenic cooling is harmless as it is also called as environment friendly and clean technology. N.R. Dhar et al. [10] have found the application of minimum quantity of lubrication (MQL) as a coolant while turning the AISI-1040 steel at different speed-feed combination shows a favourable condition as compared to the dry and conventional cooling conditions. Cutting temperature, dimensional inaccuracy and surface roughness get reduced to a great extent by using the MQL. Not only these, the use of MQL are environment friendly as well as enhance the machinability characteristic.

Shane et al. [11] investigates the use of cryogenic as a coolant in a new economical approach so that it can reduce the tool-work piece interface temperature and tool wear. Since machining of Titanium alloy Ti-6Al-4V is very difficult because of its high hardness, thus the tool life is extremely short in this condition of machining. Therefore, the use of cryogenic as a coolant in machining increases the tool life. In M.M.A. Khan et al. [12], the applications of MQL based on the vegetable oil as coolant in the turning of low alloys steel AISI 9310 have been observed more favourable as compared with dry and wet conditions. In this system the vegetable oil is sprayed with the help of air in heat affected zone which reduce the cutting temperature, tool wear, surface roughness, as well as environment pollution a great extent as compared with dry and wet condition.

Maurya et al. [13] have focuses on methodology presented by various researchers to investigate the mechanical properties of EN-36C alloy steel. The objective of this work is to control the flow rate of the coolant as per variation in the tool tip temperature so that appropriate cooling could be done without loss of coolant as well as power consumption. The cooling control panel system has been developed to response the supply of coolant as per the variation of tool tip temperature to obtain better surface finish and tool life. It is responsible for the saving of coolant and power consumption at any appropriate cutting process parameters.

## Methodology

In the present work, the turning operation has been performed on mild steel bars of same diameters with High Speed Steel (HSS) cutting tool at various process parameters keeping feed rate constant throughout the experiments in the Flat Bed Lathe machine (CA6161). The experiments were conducted with and without use of water-soluble oil coolant. The cutting conditions used in the experiments are given in Table 1. The complete flow chart of methodology is shown in Figure 1.

Table 1: Cutting Conditions for experiments

Spindle speed(RPM)	112	180	280	450	710
Depth of cut (mm)	0.4	0.6	0.8	1.2	1.4
Length of cut (m)			0.6		
Feed rate (mm/rev.)			0.1		

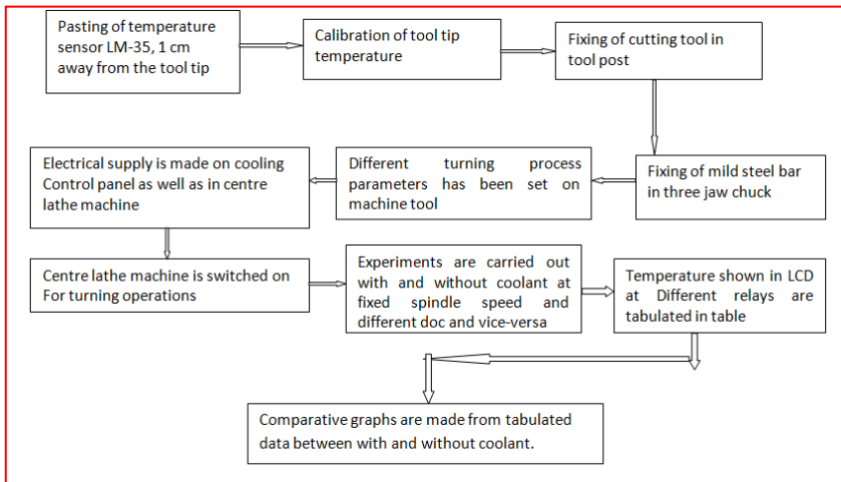


Figure 1: Methodology flow chart

## Development of Cooling Control Panel System

An important mechatronics cooling control panel system is based on the use of temperature sensor i.e. LM-35 and microcontroller ATmega-16 which has high-performance, low-power AVR® 8-bit microcontroller having operating voltages 2.7 - 5.5 V and speed grades 0 - 8 MHz. Sensor gives the

temperature of the tool tip in centigrade which is displayed on the LCD. There is number of relays which give the signals at different set of temperatures as per the program of the microcontroller. The flow rate of coolant is controlled by switching off the relays step by step. Higher position of the relay gives the higher flow rate.

The proposed cooling control panel system has been developed to reduce the cutting tool tip temperature in more robust way as compare to conventional cooling system and measure the flow rate of coolant as per the variation of cutting tool tip temperature which is sensed by the sensor i.e. -35 Precision Centigrade Temperature Sensors and automatic on and off of the coolant flow as per the temperature variation of the tool tip. Cooling control panel system consists of number of components which is shown in Figure 2.

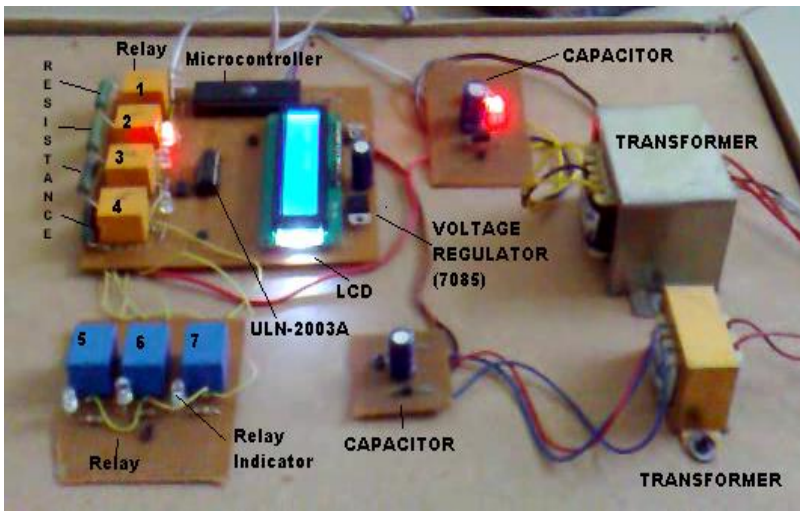


Figure 2: Cooling control panel system

### **Calibration of Experimental Data**

The following procedure has been adopted to perform the experiment on the cooling control panel system for the calibration of tool tip temperature vs. sensor temperature (LM-35) which is located 1 cm away from the cutting tool tip.

First, the cutting tool and thermometer has fixed in the burette stand in such a way that the tool tip as well as thermometer is dipped in the oil contained in glass beaker and placed it on stand. The oil glass is heated with sprit lamp continuously till the experiment is completed. The electrical supply is made to the cooling control panel system for running the circuit in response the LCD gets on and showing the normal temperature. Oil and tool

tip temperature is displayed by the thermometer dipped in oil bath. LCD temperature is the temperature of sensor location which is fixed 1 cm away from the tool tip. The reading of tool tip temperature and sensor are recorded time to time.

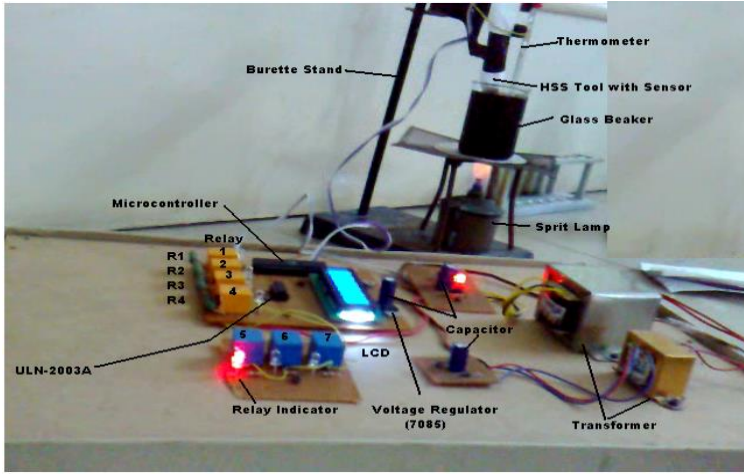


Figure 3: Experimental setup for calibration of tool tip temperature

Table 2: Calibration of tool tip temperature

S.N.	Sensor temperature in °C	Tool tip temperature in °C
1	37	80
2	40	90
3	46	97
4	50	102
5	56	108
6	61	113
7	66	118
8	71	124
9	73	126
10	78	130
11	81	131
12	83	132
13	85	134
14	90	139
15	91	140
16	95	142
17	101	144
18	104	150
19	107	153
20	111	157
21	113	159



As the LCD temperature reached 51 °C, the first relay switched on as per the program of microcontroller. At this instant, the pump starts, and flow of coolant takes place, Noted down the reading of LCD and thermometer temperatures. As the temperature of LCD is reached 61 °C, the second relay switched on and pump speed is increased in response to increase the flow rate of coolant. Again, noted down the readings of LCD and thermometer temperatures. The process is continued till the last relay is switched on at 121 °C. Again, noted down the readings of LCD and thermometer temperatures. This is all about the calibration of tool tip temperature vs. sensor location temperature as shown in Figure 3. The sensor temperatures corresponding to tool tip temperature are observed through the LCD readings which are given in Table 2.

## **Experimental work**

After performing the calibration of tool tip temperature, the cooling control panel system is used to perform the turning operations on centre lathe machine at different depth of cut and spindle speed with and without coolant.

First, the cutting tool has been fixed in tool post, which contains the temperature sensor i.e. LM-35, 1 cm away from the tool tip and the tool tip made the contact with work piece i.e. mild steel bar which is fixed in three jaw chuck. The electrical supply is made on cooling control panel system for running the circuit in response; the LCD gets on and showing the normal temperature.

The different parameters has been set in centre lathe machine such as spindle speed, depth of cut, feed rate and the centre lathe machine is switched on, as the turning operation starts, the tool tip temperature starts increasing and the sensor temperature is displayed on the LCD which is fixed 1 cm away from the tool tip. As the LCD temperature reached 51 °C the first relay switch on as per the programmed of microcontroller. At this instant the pump start and in response flow of coolant takes place. In similar way when the temperature of LCD is reached on 61 °C the second relay switched on and the pump speed is increased in response the flow rate increased. This process is continued till the last relay is switched on at 121 °C. This experiment is carried out at fixed spindle speed such as 180, 280 and 450 rpm at different depth of cut such as 2 mm, 0.4 mm, 0.6 mm, 0.8 mm, 1 mm, 1.2 mm, and 1.4 mm with and without coolant flow. This experiment is also carried out at different value of fixed depth of cut such as 0.2 mm, 0.4 mm, 0.6 mm, 0.8 mm, 1 mm, 1.2 mm, and 1.4 mm at various spindle speed such as 112 rpm, 180 rpm, 280 rpm, 450 rpm, and 710 rpm with and without coolant flow. The experimental observation has been shown in Table 3 and Table 4.



Figure 4: Cooling control panel setup on center lathe machine

Flow rate of the coolant is measured with the help of measuring beaker and stop watch at the onset of different relay having different temperature such as 51 °C, 61 °C, 71 °C, 81 °C, 91 °C, 101 °C, 111 °C, and 121 °C which is shown in Table 5.

Table 3: Observation table at different speed

Exp. No	DOC	N1 (180 rpm)		N2 (280 rpm)		N3 (450 rpm)	
		Without coolant	With coolant	Without Coolant	With Coolant	Without Coolant	With Coolant
1	0.2	40	40	38	24	40	24
2	0.4	45	45	62	26	75	27
3	0.6	55	55	85	28	100	32
4	0.8	75	75	100	30	125	34
5	1.0	85	85	110	43	135	36
6	1.2	100	100	120	36	165	38
7	1.4	110	110	145	40	185	44
8	1.6	122	122	160	45	220	48

Table 4: Observation table at different DOC

Exp. No	Speed	D1=0.4		D2=0.6		D3=1.2		D4=1.4	
		Without coolant	With coolant	Without Coolant	With Coolant	Without Coolant	With Coolant	Without Coolant	With Coolant
1	112	35	22	36	22	45	20	55	22
2	180	45	24	50	24	100	24	110	26
3	280	65	28	80	36	125	36	150	38
4	450	78	30	110	40	160	44	200	46
5	710	95	32	124	44	230	50	240	51

**Table 5: Observation table for coolant flow rate**

S.N.	Tool tip temperature (°C)	Coolant flowrate (L/min)
1	102	1.132
2	113	1.249
3	118	1.428
4	130	1.578
5	139	1.764
6	147	1.999
7	157	2.307
8	165	3.000

## Results and Discussions

Calibration data of tool tip which are obtained from experimentation have been listed in Table 2. It has been seen that there was a steep increase in the curve which has been obtained from the calibration data. Thus the graph shows that the data obtained from the experiments is quiet successful and correct which is shown in Figure 5.

The curve obtained from observations data at fixed spindle speed and different depth of cut is listed in Table 3 have been shown in Figure 6 (a), (b) and (c). The curve is drawn with tool tip temperature vs depth of cut in Figure 6 (a) without and with coolant at speed of 180 rpm. It is clearly seen that the curve obtained without coolant has gradual increase in slope because of less development of tool tip temperature at slow speed (180 rpm). Whereas the curve at the same speed with coolant has steep down slope as compared to without coolant which is favorable condition in turning operations. Similarly it could be seen in Figure 6 (b) and (c), but curve at the speed of 450 rpm has steep increase in slope without coolant as compare to curve obtained at speed of 180 rpm and 280 rpm. It is due to the higher development of tool tip temperature at high speed. Thus from graph, it is clear that the mechatronics application of designed cooling control panel system enabled the reduction in cutting tool tip temperature in more robust way as compare to conventional cooling system.

The curve obtained from observations data at fixed depth of cut and different spindle speed is listed in Table 4 have been shown in Figure 7(a), (b), (c) and (d). In Figure 7 (a), the curve is drawn with tool tip temperature vs spindle speed without and with coolant at fixed depth of cut of 0.4 mm, 0.6 mm, 1.2 mm and 1.6 mm. It is clearly seen that the curve obtained without coolant has gradual increase in slope because of less development of tool tip temperature at low depth of cut. Whereas the curve at the same depth of cut with coolant has steep down slope as compared to without coolant which shows favorable condition in turning operations. Similarly it could be seen in figure 7 (b), (c) and (d) but curve at the depth of cut of 1.2

mm and 1.4 mm has steep increase in slope without coolant as compare to curve obtained at depth of cut 0.4 mm and 0.6 mm. It is due to the higher development of tool tip temperature at high depth. Thus, from graph it is clear that the mechatronics application of designed cooling control panel system enabled the reduction in cutting tool tip temperature in more robust way as compare to conventional cooling system.

The curve of flow rate vs. tool tip temperature which is obtained from the experimental data listed in Table 5 is shown in Figure 7. The flow rate of coolant has been measured at variable tool tip temperature in liter/minute. It has been observed that the coolant flow rate increased with increase in temperature. The coolant flow rate has been found 1.13 liter/minute at tool tip temperature of 102 °C and 3 liter/minute at the tool tip temperature of 165 °C.

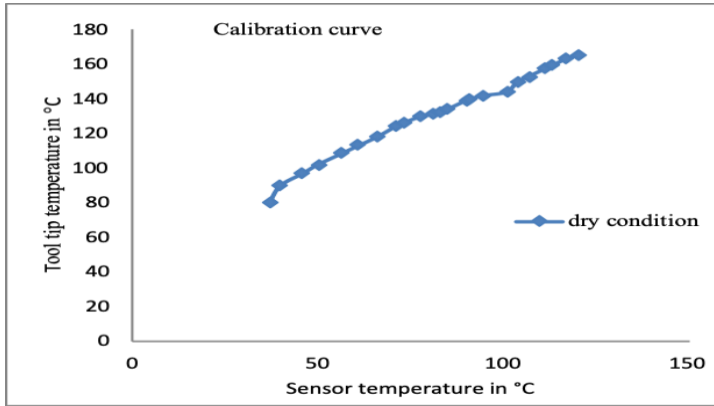


Figure 5: Calibration of tool tip temperature vs. sensor temperature

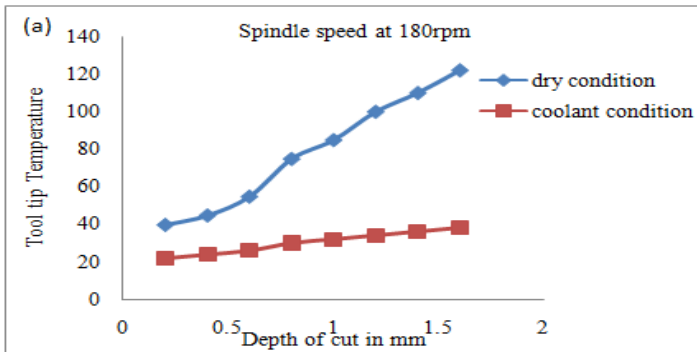


Figure 6 (a): Curve for tool tip temperature vs. depth of cut

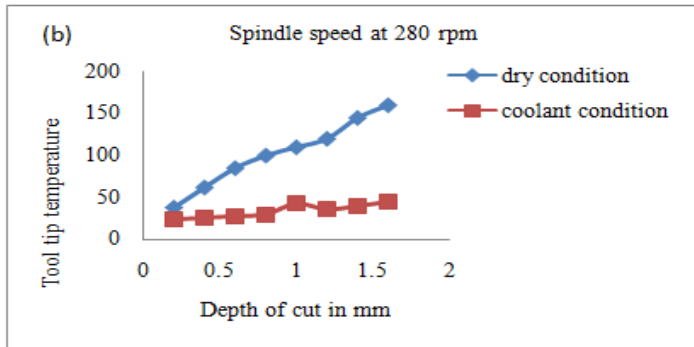


Figure 6 (b): Curve for tool tip temperature vs. depth of cut

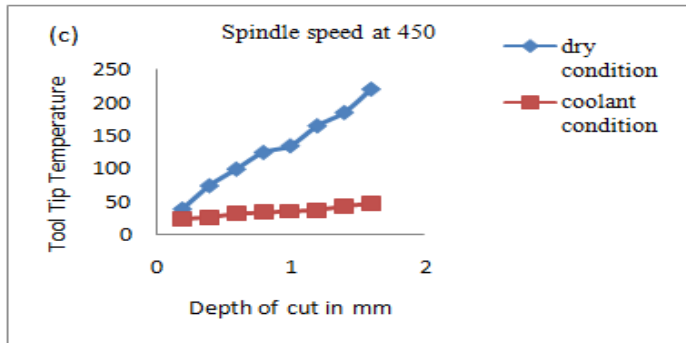


Figure 6 (c): Curve for tool tip temperature vs. depth of cut

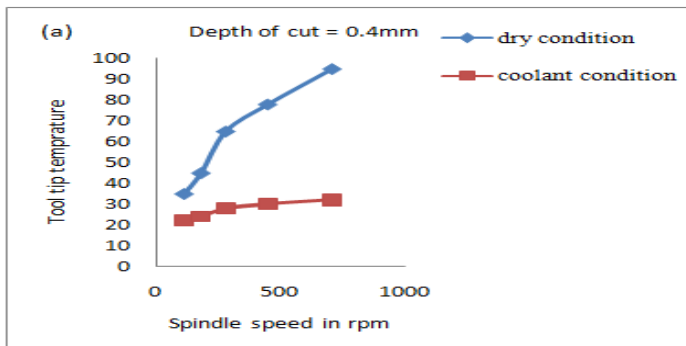


Figure 7 (a): Curve for tool tip temperature vs. spindle speed

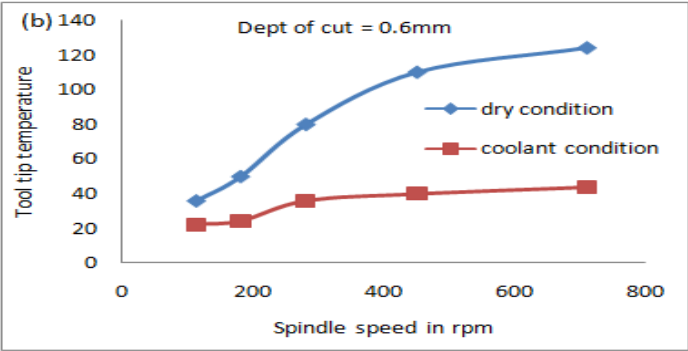


Figure 7 (b): Curve for tool tip temperature vs. spindle speed

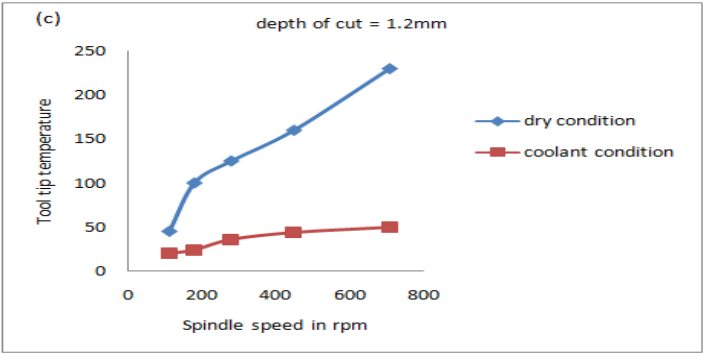


Figure 7 (c): Curve for tool tip temperature vs. spindle speed

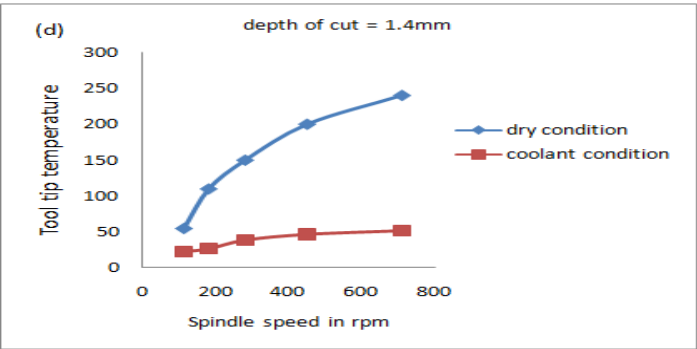


Figure 7 (d): Curve for tool tip temperature vs. spindle speed

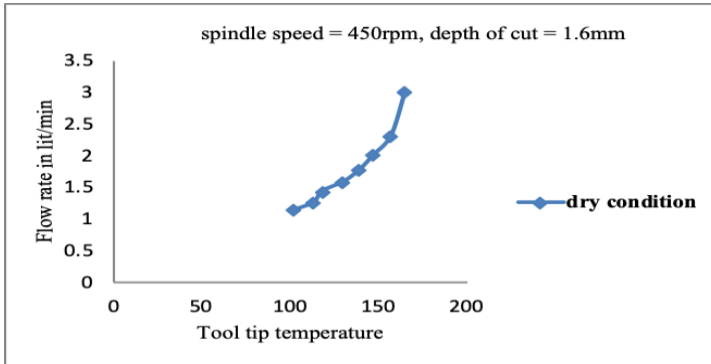


Figure 8: Curve for flow rate vs. tool tip temperature

## Conclusions

Based on the present experimental study, the following conclusions are drawn:

- Cooling control panel for the measurement of cutting tool tip temperature has been successfully designed and used to measure the tip temperature during turning operation.
- The coolant is supplied only when the sensor temperature has been reached at fixed value of 51 °C during turning operation which shows the tool tip temperature is about 94 °C. Below this sensor temperature of 51 °C, the coolant pump will always in off position which save the energy and coolant wastage. In case of conventional method, the coolant flow is continued which consume more power and wastage of coolant.
- Cooling control panel system can be used in any machining operation with changing the sensor location as per the position of the cutting tool in the machine tool.
- The cutting tool tip temperature has been found reduced drastically at various cutting speeds and depth of cut with the use of cooling control panel system.
- The coolant flow rate has been found increased in the given tool tip temperature range under dry machining at spindle speed of 450 rpm and depth of cut of 1.6 mm.

## References

- [1] M.S. Islam, "Tool wear investigation on mild steel for turning operation," B.Sc. Engineering project Report, Dept. of Mechanical Engineering KUET Khulna, 2003.
- [2] M. A. Hasib, A. A. Faruk, N. Ahmed, "Mist application of cutting fluid," *International Journal of Mechanical & Mechatronics Engineering IJMME-IJENS* 10 (4), 13-18 (2010).
- [3] E. Benedicto, D. Carou, E.M. Rubio, "Technical, economic and environmental review of the lubrication/cooling systems used in machining processes," *Procedia Engineering* 184, 99-116 (2017).
- [4] Y Oda, Y. Kawamura, M. Fujishima, "Energy consumption reduction by machining process improvement," *Procedia CIRP* 4, 120-124, (2012).
- [5] S. Nandgaonkar, T V K Gupta, S. Joshi, "Effect of water oil mist spray (WOMS) cooling on drilling of Ti6Al4V alloy using Ester oil based cutting fluid," *Procedia Manufacturing* 6, 71-79 (2016).
- [6] A. Attanasio, M. Gelfi, C. Giardini, C. Remino, "Minimal quantity lubrication in turning: Effect on tool wear," *Wear* 260, 333-338 (2006).
- [7] N.R. Dhar, M. Kamruzzaman, M. Ahmed, "Effect of minimum quantity lubrication (MQL) on tool wear and surface roughness in turning AISI-4340 steel," *Journal of Materials Processing Technology* 172, 299-304 (2006).
- [8] N.R. Dhar, M.W. Islam, S. Islam, M.A.H. Mithu, "The influence of minimum quantity of lubrication (MQL) on cutting temperature, chip and dimensional accuracy in turning AISI-1040 steel," *Journal of Materials Processing Technology* 171, 93-99 (2006).
- [9] N.R. Dhar, M. Kamruzzaman, "Cutting temperature, tool wear, surface roughness and dimensional deviation in turning AISI-4037 steel under cryogenic condition," *International Journal of Machine Tools & Manufacture* 47, 754-759 (2007).
- [10] N. R. Dhar, M.T. Ahmed, S. Islam, "An experimental investigation on effect of minimum quantity lubrication in machining AISI 1040 steel," *International Journal of Machine Tools & Manufacture* 47, 748-753 (2007).
- [11] S. Y. Hong, I. Markus, W. Jeong, "New cooling approach and tool life improvement in cryogenic machining of titanium alloy Ti-6Al-4V," *International Journal of Machine Tools & Manufacture* 41, 2245-2260 (2001).
- [12] M.M.A. Khan, M.A.H. Mithu, N.R. Dhar, "Effects of minimum quantity lubrication on turning AISI 9310 alloy steel using vegetable oil-based cutting fluid," *Journal of Materials Processing Technology* 209, 5573-5583 (2009).



- [13] R. K. Maurya and M. S. Niranjana, “An experimental analysis of process parameters for EN-36C alloy steel using CNC lathe – A review”, *Materials Today: Proceedings*, (2019).

# Effect of Process Parameters on Surface Roughness in HPC Drilling of AISI 1055 Steel

*H.V. Shete\**

*Ashokrao Mane Group of Institutions,  
Department of Mechanical Engineering,  
Kolhapur-416 112, Maharashtra, India  
\*sheteaditya@yahoo.co.in*

*M.S. Sohani*

*Shaikh College of Engineering and Technology,  
Belagavi, Karnataka, India*

## ABSTRACT

*Data regarding the influence of high-pressure coolant on the performance of drilling process using design of experiment has been limitedly available. This paper presents the effect of higher coolant pressures along with spindle speed, feed rate and peck depth on the surface roughness of hole using Taguchi technique. Experimental set up was developed consisting of specially manufactured high-pressure coolant system and high-pressure adapter assembly attached to vertical machining center. Developed experimental set up has optimized utilization of non-through coolant vertical machining center in a small-scale industry. Experiments were conducted on AISI 1055 steel with TiAlN coated drill on the vertical machining center. Taguchi technique was used for design of experiment and analysis of results. Results revealed that the surface roughness improve till coolant pressure reaches to an optimum value of 13.5 bar and there after it decreases. Coolant pressure and spindle speed was the significant process parameters for the hole surface roughness. Surface roughness at the top of hole was considerably lower than the bottom of hole, under the action of all process parameters. Supply of coolant at high pressure has resulted in lower surface roughness even with large peck depth; which indicate that, manufacturing cost can be reduced with the use of high-pressure coolant in drilling.*

**Keywords:** *High Pressure Coolant (HPC); High Pressure Coolant System; Adapter Assembly; Taguchi Method*

## **Introduction**

High pressure cooling, cryogenic cooling [1,2] and atomized coolant spray [3,4] are the most focused trends in the manufacturing research [5]. Various researchers have studied the high-pressure coolant machining. Lopez de Lacalle et al. [6] studied the influence of HPC in drilling of Inconel 718 and Ti6Al4V. HPC drilling with internal coolant showed better tool life than the conventional coolant drilling, even at high cutting speeds. Dhar et al. [7] concluded that HPC drilling results in lesser roundness deviation. Bermingham et al. [8] conducted drilling experiments on Ti-6Al-4V with WC-Co drill at 70 bar coolant pressure and concluded that the productivity and tool life was substantially improved with HPC.

Jessy et al. [9] investigated the influence of coolant supplied in the range of 0.01 to 0.03 bar pressure and revealed that, internal coolant drilling results in considerable reduction of drill temperature than the external coolant drilling. Bagci and Ozelik [10] studied the impact of an internal air coolant supplied at 1 bar and 3 bar pressure and revealed that, the coolant pressure has greater influence on the drill temperature. Li et al. [11] analyzed drilling of Ti alloy with spiral point drill at 2 bar coolant pressure. The study emphasized the scope for research work in HPC drilling. Shete and Sohani [12] showed that the drilling at the bottom of hole was more critical than the top of hole. D'Addona and Raykar [13] concluded that, coolant pressure has a considerable influence on the tool temperature and higher coolant pressure results in efficient cooling and effective lubrication action at the cutting zone. Tanabe and Hoshino [14] developed a new forced cooling technology for machining difficult-to-machine material and concluded that the technology effectively cools the tool tip and removes the chips. Arunkumar et al. [15] investigated effects of deep hole drilling parameters on the hole quality and concluded that the coolant pressure, spindle speed are the significant parameters affecting on the surface roughness, circularity and cylindricity of hole. Oezkaya and Biermann [16] investigated the velocity, kinetic energy and distribution of coolant oil at the cutting edges and in the clearance between tool flute and work piece in deep drilling process of AISI 316L. The study concluded that heat generated between tool, work piece and chip cannot be removed satisfactorily, due to reduced flow velocity of coolant during drilling.

The literature survey revealed that, study pertaining to the HPC drilling has been limited to the use of a constant high-pressure coolant and pinpointed on the necessity of investigation on the effect of HPC in drilling process using design of experiment [17]. Hence, present study aims to determine the effect of variation of high pressure of coolant, spindle speed, feed rate and peck depth on the surface roughness of hole in drilling using Taguchi Technique. The present work involves the development of an experimental set up, so as to boost the productivity in small scale industries.

The investigation has been performed to obtain the optimal process parameters of drilling process, which results in reduced surface roughness and manufacturing cost.

## **Experimental Set Up**

Drilling operation constitutes, drilling throughout holes of diameter 10 mm and depth 55 mm in AISI 1055 steel workpieces of  $\text{Ø} 20 \times 55$  mm dimension. The specifications of solid coated carbide drill [18] are shown in Table 1. Semi synthetic coolant was selected, as it is widely used in manufacturing industries. Specifications of the coolant are shown in Table 2.

The selected VMC was of low coolant pressure-non through coolant type category. Hence a specially manufactured high-pressure coolant system and high-pressure adapter assembly was attached to this machine, as shown in Figure 1. The HPC system develops and supply high pressure coolant to adapter assembly and thereafter adapter assembly supply this coolant to the through coolant drill.

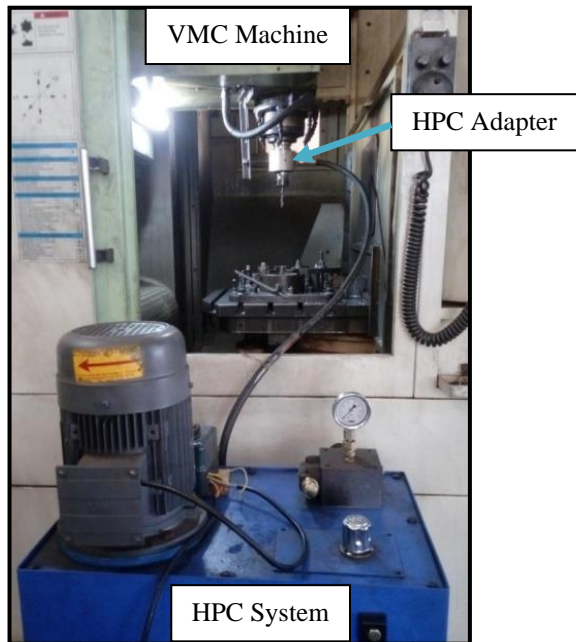


Figure 1: Experimental set up

The experimental set up was developed specially for the VMC machines, which are not having inbuilt through coolant drilling or milling facility. Thus, it optimizes the utilization of existing non-through coolant VMC's in small and medium scale manufacturing industries.

Table 1: Specifications of through coolant drill

Tool material	Coating	Drill diameter (mm)	Flute length (mm)	Point angle (°)
Micro grain carbide	TiAlN	10	61	140

Table 2: Specifications of the coolant

Type	Grade	PH (3% solution)	Coolant concentration
Semi synthetic coolant	Tectyl cool 260B	-9.7	3%

## Design of Experiment

Taguchi method is commonly used for the design of experiment [9, 10]. In the present investigation, four process parameters were selected and their range was selected, so as to maximize the production rate. Range and levels of input process parameters are shown in Table 3. The L9 orthogonal array was selected, which consists of nine rows and four columns as shown in Table 4.

## Conduction of Experiment

As per orthogonal array, experiments were conducted on the HPC experimental set up. The experiments were randomized to avoid any error in the results. The HPC jets developed through the drill tool is shown in Figure 2 and the HPC drilling operation in workpiece is shown in Figure 3.

Table 3: Range and levels of input process parameters

Process parameter	Minimum level 1	Middle level 2	Maximum level 3
Coolant pressure	7	13.5	20
Spindle speed	1500	3000	4500
Feed rate	0.05	0.165	0.28
Peck depth	10	15	20

Table 4: Orthogonal array

Expt. No.	Coolant pressure (bar)	Spindle speed (rpm)	Feed rate (mm/rev)	Peck depth (mm)
1	7	1500	0.05	10
2	7	3000	0.165	15
3	7	4500	0.28	20
4	13.5	1500	0.165	20
5	13.5	3000	0.28	10
6	13.5	4500	0.05	15
7	20	1500	0.28	15
8	20	3000	0.05	20
9	20	4500	0.165	10



Figure 2: HPC jets through the drill tool



Figure 3: HPC drilling

## Experimental Results

Surface roughness of drilled hole was measured with Mitutoyo surface roughness tester as shown in Figure 4. From top and bottom surface of workpiece, roughness was measured at a position of 6 mm and the measured value was represented as surface roughness at top and surface roughness at bottom, respectively. The average values of hole surface roughness are given in Table 5. Figure 5(a, c, e) and Figure 5(b, d, f) show the micrographs of the

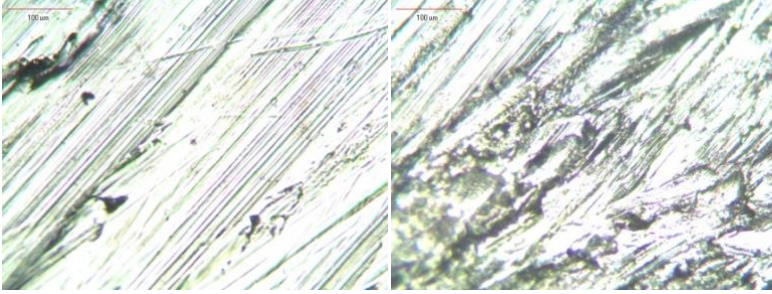
hole surface at the top and bottom position, respectively at the magnification of x10 (100  $\mu\text{m}$ ).



Figure 4: Set up for surface roughness measurement

Table 5: Experimental results

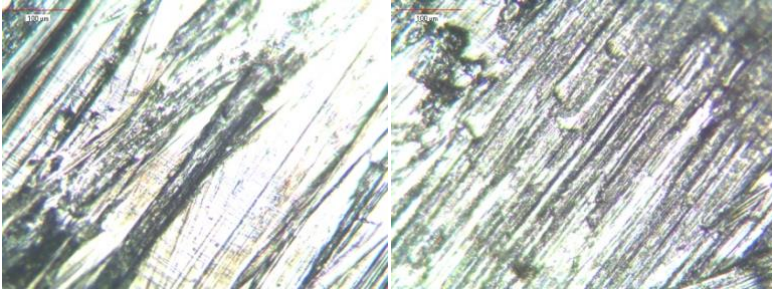
Expt. No.	Hole surface roughness at top ( $\mu\text{m}$ )	Hole surface roughness at bottom ( $\mu\text{m}$ )
1	1.35	2.63
2	1.30	2.44
3	0.83	1.02
4	0.72	0.95
5	0.39	0.61
6	0.17	0.25
7	0.83	0.86
8	0.29	0.52
9	0.25	0.51



(a)

(b)

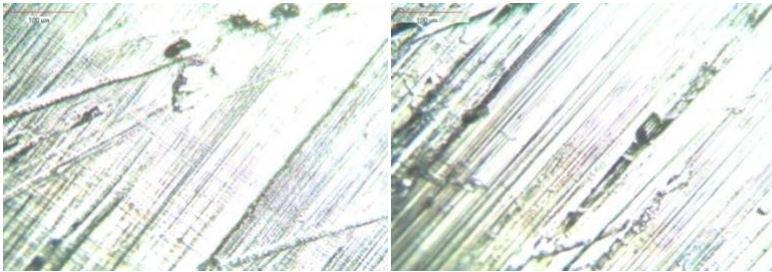
Experiment No. 3: coolant pressure: 7 bar; spindle speed: 4500 rpm; feed rate: 0.28 mm/rev; peck depth: 20 mm



(c)

(d)

Experiment No. 5: coolant pressure: 13.5 bar; spindle speed: 3000 rpm; feed rate: 0.28 mm/rev; peck depth: 10 mm



(e)

(f)

Experiment No. 9: coolant pressure: 20 bar; spindle speed: 4500 rpm; feed rate: 0.165 mm/rev; peck depth: 10 mm

Figure 5: Micrograph of hole surface at top and bottom.



## Analysis of Results

The experimental design, plots and analysis have been carried out using Minitab 17 software. “Smaller is better” criterion was used for the determination of S/N ratios, as smaller values of surface roughness are necessary for better drilling performance. The S/N ratio of output characteristics for each input parameter was calculated from the experimental results and main effects of process parameters for S/N data and mean data were plotted.

### Analysis of hole surface roughness at top

Response table and main effects plot for signal to noise ratios is shown in Table 6 and Figure 6, respectively. Response table and main effects plot for means is shown in Table 7 and Figure 7, respectively.

Table 6: Response table for signal to noise ratios

Parameter level	Coolant pressure (bar)	Spindle speed (rpm)	Feed rate (mm/rev)	Peck depth (mm)
1	-1.0890	0.6217	7.8455	5.8711
2	8.8077	5.5506	4.2052	4.9102
3	8.1372	9.6836	3.8052	5.0746
Delta	9.8967	9.0618	4.0403	0.9609
Rank	1	2	3	4

Table 7: Response table for means

Parameter level	Coolant pressure (bar)	Spindle speed (rpm)	Feed rate (mm/rev)	Peck depth (mm)
1	1.1600	0.9667	0.6033	0.6633
2	0.4267	0.6600	0.7567	0.7667
3	0.4567	0.4167	0.6833	0.6133
Delta	0.7333	0.5500	0.1533	0.1533
Rank	1	2	3.5	3.5

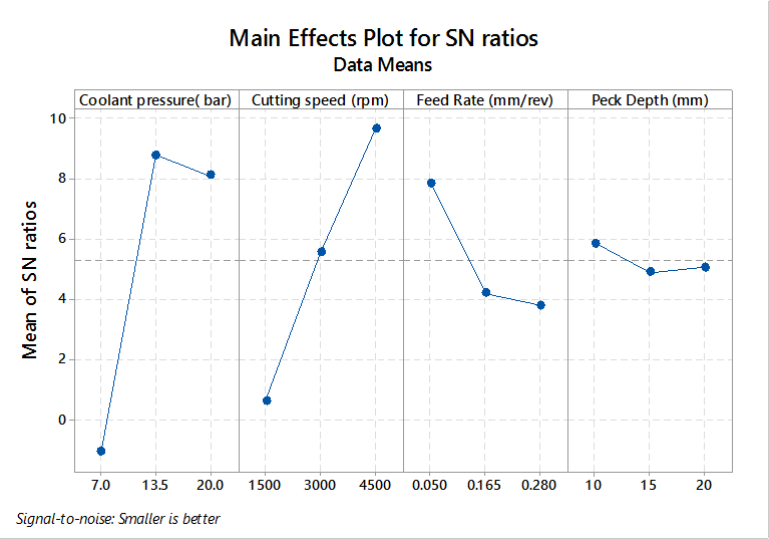


Figure 6: Main effects plot for S/N ratios

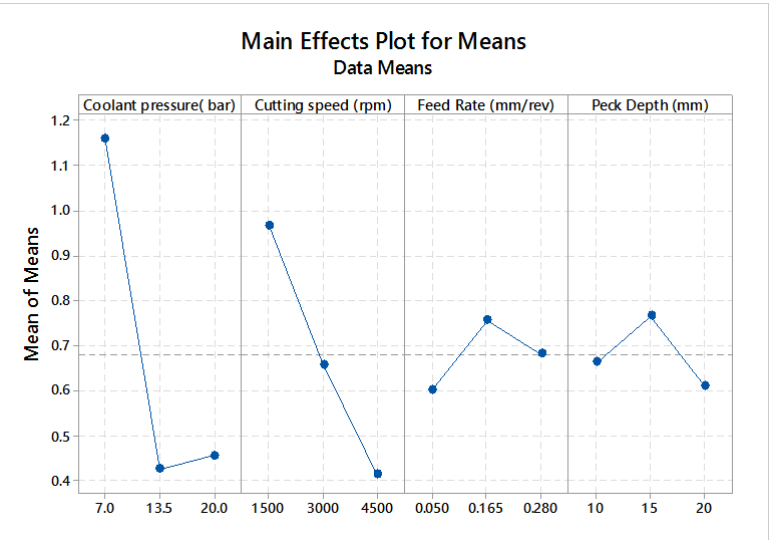


Figure 7: Main effects plot for means

### Analysis of hole surface roughness at bottom

Response table and main effects plot for signal to noise ratios is shown in Table 8 and Figure 8, respectively. Response table and main effects plot for means is shown in Table 9 and Figure 9, respectively.

Table 8: Response table for signal to noise ratios

Parameter level	Coolant pressure (bar)	Spindle speed (rpm)	Feed rate (mm/rev)	Peck depth (mm)
1	-5.4396	-2.2145	3.1185	0.5810
2	5.5934	0.7530	-0.4846	1.8678
3	4.2907	5.9059	1.8105	1.9956
Delta	11.0330	8.1204	3.6031	1.4147
Rank	1	2	3	4

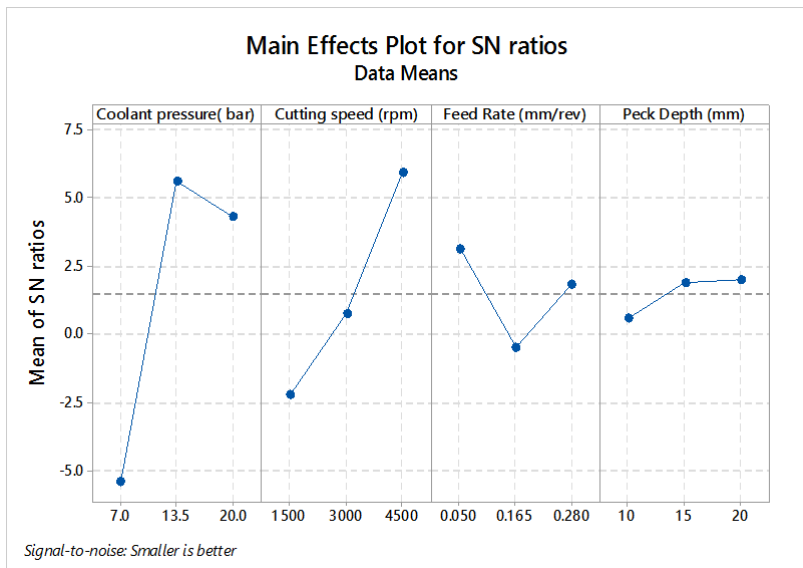


Figure 8: Main effects plot for S/N ratios

Table 9: Response table for means

Parameter level	Coolant pressure (bar)	Spindle speed (rpm)	Feed rate (mm/rev)	Peck depth (mm)
1	2.0300	1.4800	1.1327	1.2500
2	0.6033	1.1893	1.3000	1.1833
3	0.6293	0.5933	0.8300	0.8293
Delta	1.4267	0.8867	0.4700	0.4207
Rank	1	2	3	4

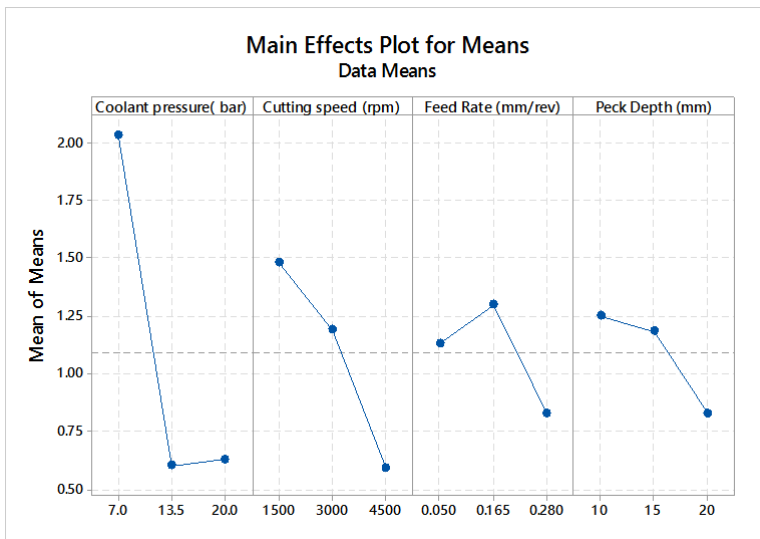


Figure 9: Main effects plot for means

## Discussions

### Effects of process parameters

The effects of input parameters on the surface roughness of hole were analyzed with the help of main effects plot for means as shown in Figure 7 and Figure 9.

#### Effect of coolant pressure

Surface roughness at top and bottom of hole decrease, as coolant pressure increase from 7 bar to 13.5 bar. This indicates that, higher coolant pressure

results in improved cooling and chip removal abilities of the coolant. But surface roughness at top and bottom increase with very small rate, as coolant pressure increase from 13.5 bar to 20 bar. Thus, coolant of 13.5 bars optimal pressure [5, 19] was sufficient to achieve the better surface roughness.

From mean values of surface roughness given in the column of coolant pressure of Table 7 and Table 9, surface roughness at top is lower than that the bottom, at all levels of coolant pressure. At level 1 of coolant pressure, surface roughness at top was 87% lower as compared to the surface roughness at bottom. At level 3 of coolant pressure, surface roughness at top was 17% lower as compared to the surface roughness at bottom. Thus, as coolant pressure increases, difference between surface roughness at top and bottom decreases. Therefore, higher coolant pressure considerably reduces the surface roughness at bottom of hole.

#### Effect of spindle speed

Surface roughness at top and bottom of hole decrease with increase in spindle speed. As spindle speed increase, cutting time is reduced, which results in reduced thrust force, reduced workpiece distortion and hence, surface finish is improved [20]. From mean values of surface roughness given in the column of cutting speed of Table 7 and Table 9, surface roughness at top of hole was decreasing at comparatively faster rate than the surface roughness at bottom, when spindle speed was increased. At level 1 of cutting speed, surface roughness at top was 51% lower as compared to the surface roughness at bottom. At level 3, surface roughness at top was 17% lower as compared to the bottom of hole. Therefore, higher cutting speed considerably reduces the surface roughness at bottom of hole.

#### Effect of feed rate

It is seen that, surface roughness at top and bottom of hole increases with increase in feed rate from 0.05 mm/rev to 0.165 mm/rev. This was due to the fact that, as feed rate increase, thrust force also increase. However, it is seen that surface roughness at top and bottom decreases, when feed rate increases from 0.165 mm/rev to 0.28 mm/rev. This may be due to the fact that, high coolant pressure and spindle speed control the increase in the surface roughness due to high feed rate.

From mean values of surface roughness given in the column of feed rate of Table 7 and Table 9, at level 1 of feed rate, surface roughness at top was 53% lower as compared to the surface roughness at bottom. At level 3 of feed rate, surface roughness at top was 15% lower as compared to the surface roughness at bottom.

#### Effect of peck depth

It was observed that, surface roughness at top and bottom decreases with increase in peck depth. When peck depth increases, number of engagements

and retractions of drill tool decreases, which results in reduced impact stresses and hence, surface roughness decreases. It indicates that, use of higher coolant pressure in drilling allow higher peck depth for lower surface roughness, which can reduce the cycle time and production cost.

From mean values of surface roughness shown in the peck depth column of Table 7 and Table 9 at level 1, surface roughness at top was 59% lower as compared to the surface roughness at bottom. At level 3, surface roughness at top was 21% lower as compared to the surface roughness at bottom.

### **Comparative effects**

Based on the discussion of effects of process parameters on the surface roughness and Table 5, it is concluded that the surface roughness at the bottom was considerably higher than the top, which is also supported by the micrographs of the hole surface shown in Figure 5. The micrographs show that, hole surface at the bottom has more feed mark, chip marks, smearing and distorted area than the surface at top. This was due the fact that, higher temperature, vibrations and chip accumulation at the bottom of hole results in more distortion of the drilled hole surface. Also from Table 5, in few cases surface roughness values obtained with HPC drilling were considerably low and competitive with finishing operations.

### **Significant parameters**

From the delta values of surface roughness and ranks shown in Table 7 and Table 9 of response table for means, significant factors affecting on the surface roughness were determined. It was observed that, coolant pressure followed by spindle speed was significant input parameters for the surface roughness at the top and bottom of hole.

### **Optimal level of process parameters**

Main effects plot for S/N ratios were used to obtain the most favorable values of process parameters [21]. The level of a parameter with highest signal to noise ratio provide the optimal level [22]. Thus from Figure 7 and Figure 9, optimal levels of parameters for HPC drilling at the top and bottom of hole are shown in Table 10. It is seen that, optimal value of peck depth was different at the top and bottom of hole, which is not possible from the production point of view. Therefore, practically feasible optimal level of process parameters for the undertaken HPC drilling process is also shown in Table 10.

Table 10: Optimal level of process parameters

Process parameter	Optimal value		
	At top	At bottom	Feasible
Coolant pressure (bar)	13.5	13.5	13.5
Spindle speed (rpm)	4500	4500	4500
Feed rate (mm/rev)	0.05	0.05	0.05
Peck depth(mm)	10	20	20

### Verification of Results

The confirmation experiments were carried at optimal level of process parameters at the top and bottom of hole and average experimental value of hole surface roughness at the top and bottom was measured to be  $0.17\text{ }\mu\text{m}$  and  $0.22\text{ }\mu\text{m}$  respectively. The percentage error in the surface roughness at the top and bottom of hole has been found to be 5% and 6.5%, which was acceptable [23] and hence experimental results were verified.

### Conclusions

Based on analysis and discussion of HPC drilling process, following conclusions were drawn.

- Optimal coolant pressure of 13.5 bar pressure was sufficient to achieve the better surface roughness.
- Surface roughness at the top of hole was considerably lower than the bottom of hole under the action of process parameters.
- Surface roughness values obtained with HPC drilling process were low and even in few cases; surface roughness was competitive with the finishing operation such as grinding operation.
- Supply of coolant at high pressure in drilling has permitted large peck depth for smaller surface roughness value; which indicates that the manufacturing cost can be reduced with HPC drilling process.
- Optimal value of process parameters in HPC drilling were investigated as; coolant pressure: 13.5 bar, spindle speed: 4500 rpm, feed rate: 0.05 mm/rev and peck depth: 20 mm.
- Coolant pressure and spindle speed were observed to be the significant process parameters affecting on the hole surface roughness in HPC drilling process.
- As a continuation of research process, the study should be undertaken to determine interactive effects of coolant pressure, spindle speed, feed rate and peck depth on the responses in HPC drilling process. Effect of tool geometry, difficult to machine materials and higher length to diameter aspect ratio may also be investigated in HPC drilling. The thermal aspects

of coolant, tool and chip during deep hole drilling must be investigated to explore the insights of HPC drilling process.

## **References**

- [1] B.D. Jerold and M.P. Kumar, "The influence of cryogenic coolants in machining of Ti-6V-4V", *Journal of Manufacturing Science and Engineering* 135 (3), 1-8 (2005).
- [2] N. Govindraj, L.S. Ahmed, and M.P. Kumar, "Experimental investigations on cryogenic cooling in the drilling of AISI 1045 Steel", *Materials and Manufacturing Processes* 29 (11-12), 1417-1421 (2014).
- [3] Lopez de Lacalle, C. Angulo, and A. Lamikiz, "Experimental and numerical investigations of the effect of spray cutting fluids in high speed milling", *Journal of Materials Processing Technology* 172 (1), 11-15 (2006).
- [4] C. Nath, S.G. Kapoor, A.K. Srivastava, and J. Iverson, "Study of droplet spray behavior of an atomization-based cutting fluid spray system for machining titanium alloys", *Journal of Manufacturing Science and Engineering* 136 (2), 1-12 (2014).
- [5] P. Blau, K. Busch, M. Dix, C. Hochmuth, A. Stall, and R. Wertheim, "Flushing strategies for high performance, efficient and environmentally friendly cutting", *Procedia CIRP* 26, 361-366 (2015).
- [6] L.N. Lopez de Lacalle, B.J. Perez, J.A. Sanchez, J.I. Llorente, A. Gutierrez, and J. Alboniga, "Using high pressure coolant in the drilling and turning of low machinability alloys", *The International Journal of Advanced Manufacturing Technology* 16 (2), 85-91 (2000).
- [7] N.R. Dhar, M.H. Rashid, and A.T. Siddiqui, "Effect of high pressure coolant on chip, roundness deviation and tool wear in drilling AISI-4340", *ARPN Journal of Engineering and Applied Science* 1(3), 52-59 (2006).
- [8] M.J. Bermingham, S. Palaniswamy, D. Morr, R. Andrews, and M.S. Dargusch, "Advantages of milling and drilling Ti-6Al-4V components with high pressure coolant", *International Journal of Advanced Manufacturing Technology* 72 (1-4), 77-88 (2014).
- [9] K. Jessy, S.S. Kumar, D. Dinakaran, and V.S. Rao, "Influence of different cooling methods on drill temperature in drilling GFRP", *International Journal of Advanced Manufacturing Technology* 76(1-4), 609-621 (2014).
- [10] E. Bagci and B. Ozel, "Effects of different cooling conditions on twist drill temperature", *International Journal of Advanced Manufacturing Technology* 34 (9-10), 867-877 (2006).
- [11] R. Li, P. Hegde, and A.J. Shih, "High throughput drilling of titanium alloys", *International Journal of Machine Tools and Manufacture* 47(1), 63-74, 2007.



- [12] H.V. Shete and M.S. Sohani, "Effect of process parameters on holediameter accuracy in high pressure through coolant peck drilling using Taguchi Technique", *International Journal of Material Forming and Machining Processes- IGI Global* 5(1), 12-31 (2018).
- [13] D.M. D'Addona and S.J. Raikar, "Thermal modeling of tool temperature distribution during high pressure coolant assisted turning of Inconel 718", *Materials* 12(3), 408 (2019).
- [14] I. Tanabe and H. Hoshino, "Development of a new forced cooling technology using a high-pressure coolant for machining difficult-to-machine materials", *Journal of Manufacturing and Materials Processing* 2 (2), 39, 2018.
- [15] N. Arun kumar, A. Thanikasalam,V. Sankaranarayana, and E. Senthil Kumar, "Parametric optimization of deep-hole drilling on AISI 1045 steel and online tool condition monitoring using an accelerometer," *Journal of Materials and Manufacturing processes* 33 (16), 1751-1764 (2018).
- [16] E. Oezkaya and D. Biermann, "Experimental and simulative investigation of the oil distribution during a deep-hole drilling process and comparing of the RANS k-w-SST and RANS hybrid SAS-SST turbulence model", *Thermal Science and Engineering* 1(4), 874 (2018).
- [17] H.V. Shete and M.S. Sohani, "Machining in high pressure coolant environment–A strategy to improve machining performance: a review", *International Journal of Manufacturing Technology and Management*, Inderscience Publication.
- [18] F. Klocke, L. Settinen, D. Lung, P.C. Priarno, and M. Arft, "High performance cutting of gamma titanium aluminizes: Influence of lubricoolant strategy on tool wear and surface integrity", *Wear* 302 (1-2), 11361144 (2013).
- [19] E.O. Ezugwu and J. Bonney, "Effect of high pressure coolant supply when machining nickel-base Inconel 718 alloy with coated carbide tool", *Journal of Materials Processing Technology* 153-154, 1045-1050 (2004).
- [20] A. Kamboj, S. Kumar, and H. Singh, "Burr height and hole diameter error minimization in drilling of AL6063/15%/SiC composites using HSS step drills", *Journal of Mechanical Science and Technology* 29 (7), 2837-2846 (2015).
- [21] P.J. Ross, *Taguchi techniques for quality engineering*, 2nd ed. (Mc-Graw Hill Education (India) Private Limited, New Delhi, 2005).
- [22] R.K. Roy, *A primer on Taguchi method*, 2nd ed. (Society of Manufacturing Engineers, Michigan, 2010).
- [23] K.H. Hashmi, G. Zakria, M.B. Raza, and S. Khalil, "Optimization of process parameters for high speed machining of Ti-6Al-4V using response surface methodology", *International Journal of Advanced Manufacturing Technology* 85(5-8), 1847-1856 (2016).

# Design and Development of the Front Wheel Hub for All-Terrain Vehicle (ATV)

Himanshu Verma, Sandeep Kumar, Rabinder Singh Bharja<sup>a</sup>, Rajan Kumar<sup>b,\*</sup>

Department of Mechanical Engineering,

Dr. B. R. Ambedkar National Institute of Technology,

Jalandhar, 144011, India

<sup>a</sup>[bharjrs@nitj.ac.in](mailto:bharjrs@nitj.ac.in), <sup>b,\*</sup>[rajank@nitj.ac.in](mailto:rajank@nitj.ac.in)

## ABSTRACT

*An all-terrain vehicle (ATV) is a single seat, open cockpit, and open wheel off-road vehicle in which the engine is located behind the driver. The present paper discusses the important aspects of designing and development of the front wheel hub of ATV. This study discusses the design of the front wheel hub while considering that it should be of light weight and high strength. This paper discusses the material selection for the hub from the two different types of material. This study includes the improvement in the design of the hub with the help of various analyses of the hub. The hub is analyzed in the various loading conditions to obtain the appropriate factor of safety with the help of a static structural module of ANSYS software.*

**Keywords:** All-Terrain Vehicle; Hub; Failure Analysis; Development; Static Structural Analysis

## Introduction

A front wheel hub is a component whose main purpose is to connect the wheel to other suspension components via stub axle and to keep the free spinning of the wheel on the bearing while keeping it attached to the vehicle. It is located between the disc and the stub axle of the ATV as shown in Figure 1. In older vehicles, front wheel bearings have been built to be serviced with repair kits because individual parts can be disassembled, washed and re-packed with grease. Generally, new vehicles are designed with front wheel assemblies comprising axle, bearing assembly, installation,

and rim flange incorporated into one unit known as a wheel bearing and hub assembly.

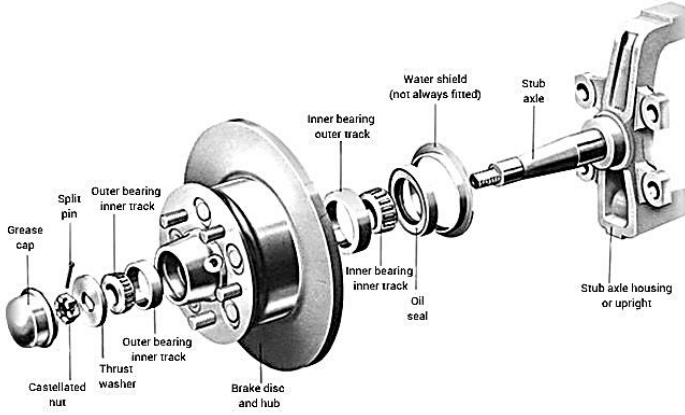


Figure 1: Wheel hub assembly [1]

BÖNAA [1] integrated the brake rotor and wheel hub in a single unit for use on automobiles and other vehicles. Conventional ATV uses different hubs and rotors are normally made as two separate parts bolted together to allow replacement of worn-out brake rotors. The disk's life span is relatively short compared to the hub which usually requires no replacement. This model results in more machining and thereby some possibilities of unbalance and misalignment during construction. Today's approach for the manufacture of hub and rotor as two separate parts requires additional material for bolt flanges, thereby increasing the overall size. Shrivastava [2] used the crash pulse scenario standard which is used for impact time to calculate the radial forces using Newton laws of motion on the hub in the worst-case scenario. Kumar et al. [3] discussed the use of aluminum composites in automobile and aerospace industries for various high performing components that are being used for varieties of applications owing to their lower weight excellent thermal conductivity. Among several series of aluminum alloys, aluminum possesses very high strength, higher toughness and is preferred for in the aerospace and automobile sector.

As the use of ATV is limited to only BAJA SAE 2018 events only thus, the hub design, material selection and structural development of the hub must choose accordingly. Baja SAE is made up of contests that represent projects in real-world engineering design and associated obstacles. Engineering students are responsible for designing and building an off-road vehicle that will survive the severe punishment of rough terrain. The goal of each team is to design and build a sporting single-seat, all-terrain vehicle with the driver's structure. The vehicle is to be a model for a robust,

functional, ergonomic and inexpensive production vehicle that meets a niche for recreational users. The semi-trailing or trailing arm suspensions are usually used in the rear of a vehicle while the MacPherson strut and double wishbone models can be used both in the front and rear [4]. Often recognized as a single control arm suspension is the MacPherson strut, comprising of a strut or shock unit, wheel hub and one control arm [5]. The strut as well as the control arm is connecting directly to the vehicle's chassis. Then the control arm attaches to the bottom of the wheel hub, while the strut connects to the top.

The reduction in the rotational mass of the hub and reduction in the overall weight of ATV lead to an increase in the acceleration. Furthermore, hub experiences the continuous stresses and impact stress due to the motion of ATV such as during braking, cornering and six feel fall. Therefore, the hub should be designed so that it should be of minimum weight and higher strength.

## **Methodology of Designing**

Designing is one of the most important and thoughtful processes. At different design stages, the various problems occurred that need to be sought out using the following five steps which are given in Figure 2 [6]:

1. Define the problem
2. Gather pertinent information
3. Generate multiple solutions
4. Analyze and select a solution
5. Test and implement the solution

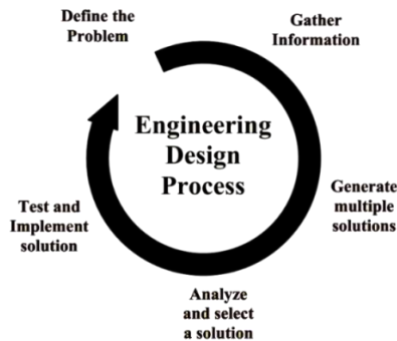


Figure 2: Design stages [6]

## Selection of Material

In the present study, the material is selected on the basis of the following properties:

1. The material should have a low density or cheap or a combination of both.
2. The material should have enough strength values to carry the load with a sufficient factory of safety (FOS).
3. It should be easily machinable.

The two materials considered for the wheel hub are Aluminium 7075-T6 and EN8 Mild Steel. Table 1 illustrates the different properties of these materials [7, 8]. The material is selected on the basis of strength to weight ratio.

Table 1: Material property chart

Property	Aluminum 7075-T6	EN-8 Mild Steel
Density	2.81 g/cm <sup>3</sup>	7.85 g/cm <sup>3</sup>
Brinell Hardness Number	150 BHN	201 BHN
Ultimate Tensile Strength	572 MPa	650 MPa
Tensile Yield Strength	503 MPa	415 MPa
Poisson's Ratio	0.33	0.33
Fatigue Strength	159 MPa	--
<b>Strength to Weight Ratio</b>	<b>203.56 MPa·cm<sup>3</sup>/g</b>	<b>83.22 MPa·cm<sup>3</sup>/g</b>

## Designing of Hub

The main objective of designing the hub is to be reliable, durable and light weight to overcome the failure of last years. In order to satisfy these requirements, AL-7075 T6 material is selected, from the two material options i.e. Al-7075-T6 and EN8, based on material strength to ratio. Prior to designing a thoroughly study is done on the previous year's design, experiences, and failures. Considering the facts and following design considerations, parameters, and last year's failure data, the preliminary design is made on CATIA software as shown in Figures 3 and Figure 4.

## Design considerations

Several design considerations are proposed before the CAD modeling of hub:

1. The pattern of bolt connected to the wheel and brake rotor is determined by the type of rim and disc respectively.
2. The size and pitch circle diameter of the rim should be considered.
3. Pitch circle diameter of the brake disc.
4. Hub length is decided by the caliper dimension constraint.
5. The material should opt accordingly as strong enough to take the weight of the car and variable stresses.

6. Wheel bearing in the hub depends on internal and external diameters of stub axle coming out of the hub.
7. Bolt size should be considered.

#### Design parameters of the hub

Following design parameters of the hub are considered in the present study:

1. Loading condition.
2. Manufacturing process.
3. Material behaviour on the application of load.

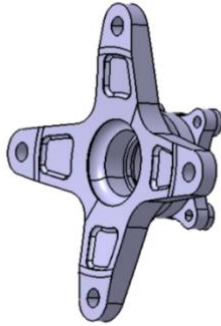


Figure 3: Final CAD model

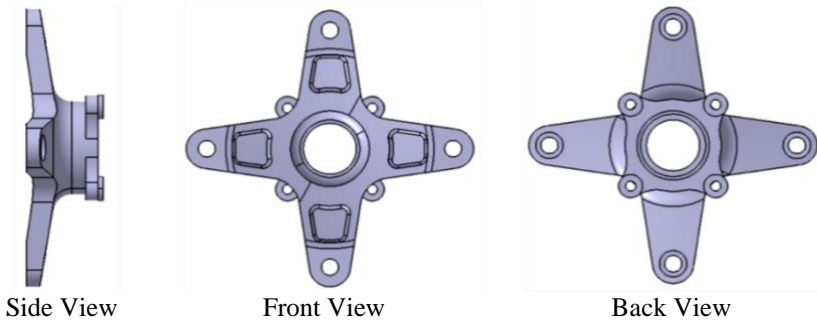


Figure 4: Different views of the hub

After several iterations as shown in Figure 5, the tapered cross-section with the fillet model is finalized for the analysis to evaluate the stressed area, deflections and life cycle of the designed component.

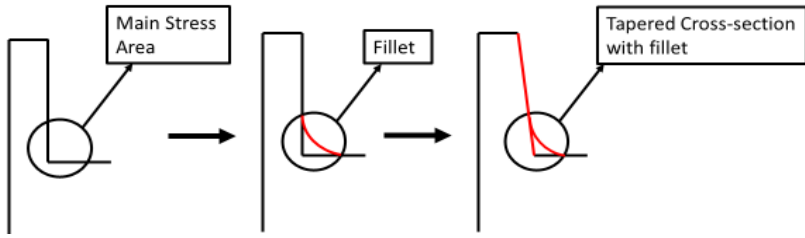


Figure 5: Improvement in the design of the hub

## Results and Discussion

For the analysis of the hub, a 3-D model is generated in CATIA and imported into ANSYS. Material specifications of Al7075-T6 shown in Table 1 are assigned in engineering data in ANSYS. To observe maximum stress produced in the hub model is subjected to extreme conditions and static analysis is carried out in ANSYS. Mesh model of the hub is shown in Figure 6, having 75420 nodes and 44464 total elements.

### Loading Conditions

#### Breaking torque

As the brakes are used frequently in the ATV so the hub comes under the frequent stresses, therefore, it requires to be analyzed properly in braking conditions. The hub experiences shear stress due to braking torque. Constraints are applied on the two end faces of the hub which are fixed on the disc side along with the application of torque 243 N-m (calculated in Appendix A) on the rim side face as shown in Figure 7.

As shown in Figures 8 and 9, the maximum stress comes near the disc mountings. Therefore, the fillet is provided at this place, however, the value of stress is very less hence the chances of failure will insignificant here.

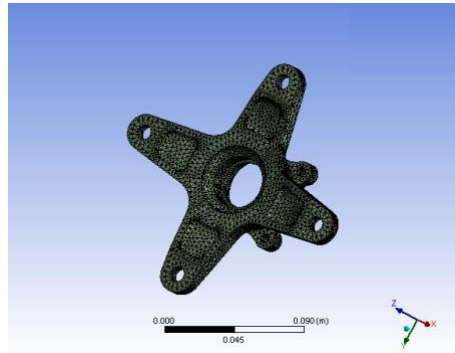


Figure 6: Mesh model of the hub

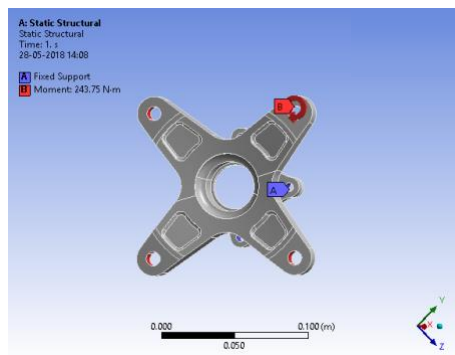


Figure 7: Loading condition in case of breaking torque

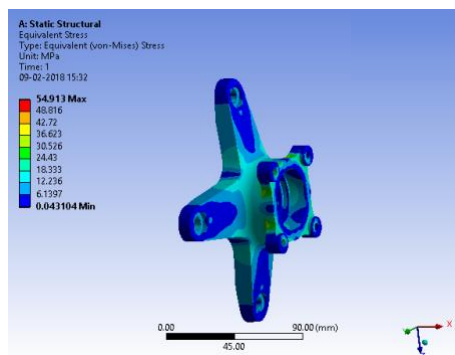


Figure 8: Von-Mises stress distribution



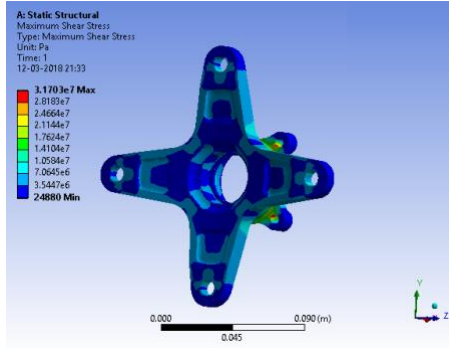


Figure 9: Maximum shear stress distribution

### Six feet fall

This is the harsh condition that can occur in the ATV especially during the suspension and traction event. During six feet fall, the hub comes under the bending condition. The normal and shear stresses both occur during the bending thus either of these stresses cannot particularly decide the FOS of the hub, therefore, the Von-Mises Stress criteria is used to decide the FOS of hub under this loading condition. Constraints are applied on both the bearing surfaces as cylindrical supports and load of 6130N (calculated in Appendix B) as remote force is applied on the rim side end face as shown in Figure 10.

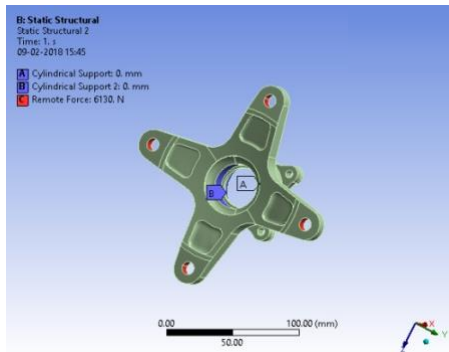


Figure 10: Loading condition in case of six feet fall

Figure 11 shows that the maximum stress occurs near the end of flanges towards the stub-axle side due to the bending of flanges, hence, failure can take place there. To avoid failure, the tapered cross-section with a fillet is kept here.

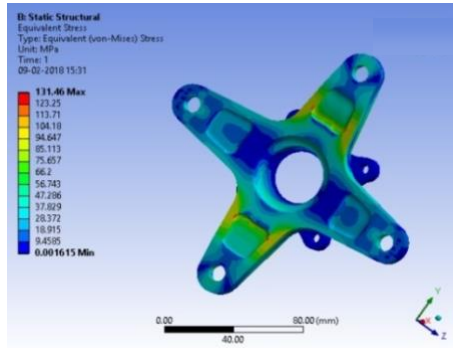


Figure 1: Von-Mises stress distribution

### Cornering

Particularly in the maneuverability event, the ATV should respond to the quick turning, therefore due to sudden turns the hub comes under the cornering forces which cause the bending of the flanges of the hub. Therefore, the Von-misses stress criteria are used for deciding the FOS of the hub in this condition. Boundary conditions are applied on both the bearing surfaces as cylindrical supports and load of 1500 N as remote force is applied on the rim side end face as shown in Figure 12.

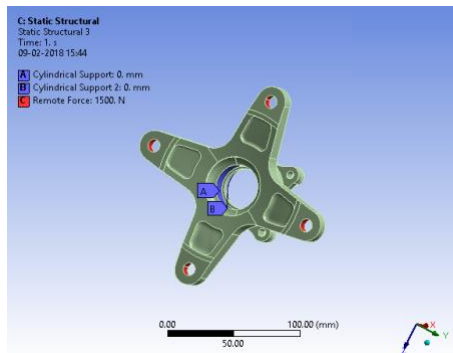


Figure 2: Loading condition in case of cornering

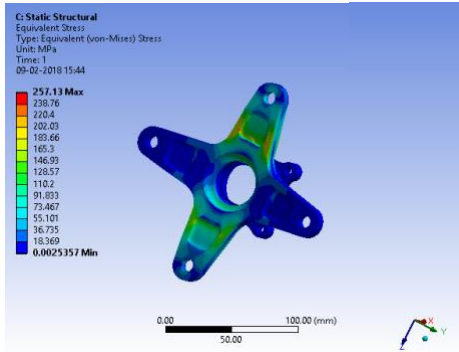


Figure 3: Von-Mises stress distribution

In this case of cornering, the chances of failure are maximum because the maximum stress with the value of 257.13 MPa occurs near the end of flanges towards the stub-axle side due to the bending of cantilever flanges as shown in Figure 13. Tapered cross-section with a fillet is provided to avoid the failure in this case also as described in the case of six feet fall.

After the analysis and improvements in various loading conditions, it is noted that the maximum stress in the most severe condition is 257.13 MPa under cornering condition on the flanges as shown in Figure 13, which is very lower as compared to the yield strength of material i.e. 503 MPa. Table 2 illustrates the maximum induced Von-Mises stress and FOS for different boundary conditions.

Table 2: Von-Mises stress and FOS for braking, six feet fall and cornering condition

Parameters	Unit	Boundary Conditions		
		Braking	Six Feet Fall	Cornering
Von-Mises stress	MPa	54.91	131.46	257.13
FOS	-	9.16	3.82	1.96

Conclusions

The weight of the manufactured hub is found to be approximately equal to the CAD model of the hub i.e. 314 g. The least weight, higher reliability, and durability of the hub are achieved through the various structural development of hub as shown in Figure 4 and with the help of the proper material selection, i.e. components Al 7075-T6 for the hub. In the various loading conditions i.e. six feet fall, cornering and braking the stresses come out to be

131.46 MPa, 257.13 MPa and 54.91 MPa with the appropriate factor of safety 3.82, 1.96, and 9.16 respectively. The front wheel hub is rigorously tested on the track and good performance is achieved.

## **1. Appendix A - Calculation of the braking torque**

Braking force on disc exerted from pedal [9]

Pedal force	= 600 N
Pedal ratio	= 6.5
Master cylinder bore diameter	= 0.75 inch
Caliper bore diameter	= 1.12 inch
Ratio of bore areas	= 2.23 inch
Caliper pad and disc friction coefficient	= 0.35

$$\text{Braking force} = 600 \times 6.5 \times 2.23 \times 0.35 \times 2 = 6088.02 \text{ N}$$

Vehicle mass considered for calculation (m)	= 185 kg
Deceleration (aa)	= 0.8 g
Traction coefficient ( $\mu$ )	= 0.8
C.G. height	= 17 inch
Wheel base	= 54 inch
C.G. height/ wheelbase ( $\gamma$ )	= 0.315
Weight distribution	= front - 45%; rear - 55%

Therefore,

$$\text{Static axle load distribution (v)} = \frac{\text{Static rear axle load}}{\text{Vehicle weight}} = 0.45$$

$$\begin{aligned} \text{Dynamic normal load on the front axle } (F_{zF, dyn}) &= (1 - v + \gamma a_d) m \times g \\ &= (1 - 0.45 + 0.314 \times 0.80) \times 185 \times 9.81 = 1454.05 \text{ N} \end{aligned}$$

$$\text{Dynamic normal load on each tyre} = \frac{F_{zF, dyn}}{2} = 727.02 \text{ N}$$

$$\text{Tractive force} = 727.02 \times 0.80 = 581.62 \text{ N}$$

$$\text{Braking torque} = 581.62 \times 11 \times 0.0254 = 162.50 \text{ Nm}$$

$$\text{Factor of safety} = 1.50$$

$$\text{Braking torque on front wheel} = 162.50 \times 1.50 = 243.75 \text{ Nm}$$

## **2. Appendix B - Calculation of six feet fall force**

According to third equation of motion [10]

$$v^2 = u^2 + 2as$$

Here,  $u = 0 \text{ m/s}$ , because the velocity in vertical direction the initial velocity in the free fall is 0.

$$a = g(9.8 \text{ m/s}^2)$$
$$s = 6 \text{ feet or } 1.81 \text{ meter}$$

$$\text{so, } v^2 = 0 + 2 \times 9.8 \times 1.81$$

$$v = 5.97 \text{ m/s}$$

$$\text{Impact force} = \frac{\text{Change in momentum}}{\text{Impact time}} = \frac{\Delta mv}{\Delta t}$$

$$\text{Initial velocity in vertical direction, } u = 0 \text{ m/s}$$

$$\text{Final velocity in vertical direction, } v = 5.97 \text{ m/s}$$

$$\text{Mass of the vehicle (m)} = 185 \text{ kg}$$

$$\Delta mv = 185 \times 5.97 = 1104.45 \text{ kg} \cdot \text{m/s}$$

$$\text{Impact time}(\Delta t) = 0.18 \text{ s}$$

$$\text{Impact force} = \frac{1104.45}{0.18} = 6130 \text{ N [2]}$$

### Appendix C - Cornering force calculation for front hub [11]

G	=	gross weight of vehicle
$F_{\mu 1}, F_{\mu 2}$	=	Longitudinal and lateral frictional forces respectively
$N_{s1}, N_{s2}$	=	Dynamic normal reactions on the front & rear tires respectively
C.G height ( $r_h$ )	=	0.432 meter
$r_{as}$	=	Track width/2
$\mu$	=	friction coefficient between tire and ground
$k_a$	=	cornering force
g	=	gravitational acceleration

$$\text{Vertical mass considered for calculation (m)} = 185 \text{ kg}$$

$$G = m \times g = 185 \times 9.81 = 1814.85 \text{ N}$$

$$F_{\mu_1} = G \times \mu = 185 \times 9.81 \times 0.80 = 1451.88 \text{ N}$$

$$F_{\mu_2} = F_{\mu_1} \times \mu_1 = 185 \times 9.81 \times 0.80 \times 0.80 = 1161.50 \text{ N}$$

$$\begin{aligned} F_{\mu_1} \times r_h + F_{\mu_2} \times r_h + (G + F_{dec}) \times r_{as} - N_{s_1} \times (r_{as} + r_{as}) &= 0 \\ = (1451.88 + 1161.50) \times 0.432 - N_{s_1} \times 1.244 \\ &+ (1814.8 + 1451.88) \times 0.622 = 0 \end{aligned}$$

$$N_{s_1} = 2540.05 \text{ N}$$

$$K_a = \left( \frac{N_{s_1}}{2} \right) \times 0.80 = 1016.02 \text{ N}$$

$$\text{Factor of safety} = 1.48$$

$$K_a = 1016 \times 1.48 \text{ N} = 1500 \text{ N}$$

## References

- [1] G. Michael, "Types of Bearing Designs Used on Rear Wheel Hubs", Wheel Bearings: Descriptions of Bearings, Races, Seals, and Hubs, 2014, [Online]. Available: <https://www.carid.com/articles/wheel-bearings.html> [Accessed: 20-05-2018]
- [2] Lars Erik BÖNAA, Integrated hub and rotor patents, WO1997040285A1, 1997-10-30.
- [3] D. Shrivastava, "Designing of all-terrain vehicle (ATV)," International Journal of Scientific and Research Publications 4 (12), 1-16 (2014).
- [4] G.V. Kumar, C.S. Rao, N. Selvaraj and M.S. Bhagyashekar, "Studies on AL6061-SiC and AL7075-Al2O3 metal matrix composites," Journal of Mineral and Material Characterization and Engineering 9 (01), 43 (2010).
- [5] M. Wan, Suspension Geometry (Cont'l), AutoZine Technical School, 2000, [Online], Available: [http://www.autozine.org/technical\\_school/suspension/tech\\_suspension2\\_1.htm](http://www.autozine.org/technical_school/suspension/tech_suspension2_1.htm) [Accessed: 02-10-2014]
- [6] Q. Riley Enterprises, LLC. (n.d.). Automobile Ride, Handling, and Suspension Design. Retrieved October 2, 2014, from <http://www.rqriley.com/suspensn.htm> [Accessed: 18-05-2018]
- [7] S. Khandani, August 2005. [Online]. Available: <https://www.saylor.org/site/wp-content/uploads/2012/09/ME101-4.1-Engineering-Design-Process.pdf>. [Accessed: 18-05-2018]

- [8] Metals Handbook, Vol.2 - Properties and Selection: Nonferrous Alloys and Special-Purpose Materials, ASM International 10th ed. (1990).
- [9] EN8 Carbon Steel, 080M40 BS 970 Specification, [Online]. Available: <http://www.astmsteel.com/product/en8-carbon-steel-080m40-bs-970/> [Accessed: 20-05-2018]
- [10] R. Limpert, Brake Design and Safety, Society of Automotive Engineers, (1992).
- [11] R.S. Khurmi, A Textbook of Engineering Mechanics, SI Units (S. Chand), (2007).
- [12] J. Rincón García, “Analysis of Wheel Hubs: Student Car,” Tampere University of Applied Sciences, (2014).

# Comparative Study on CI Engine Performance and Emissions using a Novel Antioxidant Additive

N Kapilan\*

Nagarjuna College of Engineering and Technology, Bangalore, India

\*kapil\_krecmech@yahoo.com

## ABSTRACT

*The depletion of conventional energy sources and environmental pollution related to use of these energy sources make biodiesel as a renewable replacement to diesel. The biodiesel can be used as an immediate replacement to fossil diesel as its properties are comparable to diesel. The main drawback of the biodiesel is its lower oxidation stability and prone to microbial growth which degrades the properties of biodiesel during storage. However, these problems can be overcome by adding suitable additives to the biodiesel. The non-edible neem oil is one of the feedstocks used for biodiesel in India. The neem biodiesel has lower oxidation stability and hence it is necessary to add suitable additive. The eucalyptus oil has better antioxidant and microbial inhibition properties and hence it was used as an additive in this work. The effect of adding this additive on the biodiesel properties, engine emissions and performance were studied. The engine tests were conducted on a compression ignition engine at different loads with various concentration of eucalyptus oil. The engine performance indicates that the thermal efficiency of the engine with biodiesel is lower than the diesel fuel while the engine exhaust emissions like HC, CO and smoke were lower with the biodiesel. The use of eucalyptus oil as an additive to the biodiesel at full load increases the engine thermal efficiency by 3.08%. Also, it lowers the engine exhaust emissions except NO<sub>x</sub> emission.*

**Keywords:** Biofuel; Biodiesel; Eucalyptus Oil; Engine Tests; Emissions

## Introduction

The world's energy demand is increasing due to globalization and urbanization and it is reported that the oil resources will be depleted by 2030



[1]. It is reported that the fossil fuel reserves of crude petroleum oil will be depleted in 35 year [2]. The enhanced manufacturing activities and increase in vehicle population increases the demand for petroleum products in India. The data released by India government indicates that the demand of oil between April 2015 and March 2016 increases by 10.9 percent. In India, the local and global car makers are introducing new car models which indirectly increase the fuel demand. An analysis shows that the 70 percent of diesel is consumed in the automobile sector. It also reports that the diesel consumption (28.48%) is by three wheelers, cars and utility vehicles are highest as compared to the agriculture sector [3].

The growth of the Indian economy is approximately 7 percent since 2000. The CO<sub>2</sub> emission emitted by the automobile vehicles is approximately 13 percent. The government of India wants to reduce CO<sub>2</sub> emission by following a sustainability method. This method prefers use of biofuel as a replacement to the fossil fuels. India is one the largest user of petroleum products and is reported that the primary energy demand will be double in India by 2030. It was estimated that if India's GDP increases by one percent then the demand for crude oil will increase by 2.89% [4].

The increase in crude oil prices and expenses related to oil imports force the government to opt for alternative fuels. India's bio-fuel policy suggest use of biofuels as a renewable replacement to petroleum products as it will reduce oil imports from other countries and indirectly improve the energy security [5]. This policy has created awareness among common people about the use of biofuels as substitute for the fossil fuels, in particular, biodiesel and bioethanol. The government policies have also boosted the production of biofuels which indirectly helps the rural economy.

The vegetable oil is converted into biodiesel by transesterification method. The methanol and ethanol are used for biodiesel production. The transesterification reaction is affected by the reaction time and temperature, type of catalyst and molar ratio of alcohol to oil [6]. The homogeneous catalyst are used for transesterification reaction, however in recent years heterogeneous catalyst are preferred. The proper selection of alcohol and catalyst is important to get higher biodiesel yield and to reduce the cost of biodiesel [7]. A significant research work has been carried to find suitable reusable solid catalysts and studied on effect of the structural properties of various solid catalysts on biodiesel yield [8]. The biodiesel wastewater contains excess catalyst, alcohol, glycerol and soap and hence it has to be purified to remove these unwanted substances [9].

The engine combustion characteristics are affected by the type of biodiesel blend and hence lower biodiesel diesel blend is preferred [10]. The viscosity of the biodiesel is higher and hence it results in coarse atomization and poor spray formation. The fuel injection system has to be modified if biodiesel is used as fuel in diesel engine due to higher cloud point of the biodiesel. The ignition delay period of biodiesel is higher than the diesel. The

biodiesel causes lower engine exhaust emissions like hydrocarbon (HC), carbon monoxide (CO) and smoke [11]. The type of biodiesel feedstock affects the biodiesel quality and directly affects the engine combustion performance and engine exhaust emissions.

Few researchers used biodiesel as fuel in compression ignition engine and suggested that the engine process variables should be optimized to get lower emissions and higher thermal efficiency [12]. The biodiesel's oxidation stability is low due to fatty acids containing double bonds. This causes formation of insoluble substances, sediment and gum. These substances may cause depositions in the fuel injection components, engine combustion chambers, filter plugging and injector fouling [13]. Few researchers reported that the biodiesel properties changes during storage and the value of viscosity and acid value increases with storage period [14]. The thermal and oxidative degradation of the biodiesel results in deterioration in fuel properties [15]. Hence suitable natural and synthetic antioxidant additives are developed and mixed with biodiesel with the concentration various from 250 to 1000 ppm [16].

Ana Carolina Roveda et al. [17] used various synthetic antioxidants like butylated hydroxy toluene (BHT) and propyl gallate (PG) and carried out accelerated storage study by varying storage temperature from 85°C to 110°C. They used rancimat method to determine the oxidative stability of PG and BHT with DHQ. They reported that the combinations of the synthetic antioxidants are effective as compared to individual compounds and the optimum mixing the additive cost. Gabriela Menegon Buosi et al. [18] used the combination of natural extracts of rosemary, oregano and basil with antioxidant (TBHQ, BHA and BHT), to improve the soya bean biodiesel oxidation stability. They reported that the best formulation is 50% rosemary, 12.5% oregano and 37.5% basil. The mixing of antioxidants to the biodiesel influences the engine combustion, thermal efficiency and engine exhaust emissions significantly [19]. The natural antioxidants derived from catechin, curcumin and quercetin are better than the butyl hydroxyanisole for the cotton seed oil biodiesel. However the interactions among the extracts varied with the total concentration [20]. The addition of natural additives such as L-Ascorbic Acid 6-palmitate, caffeic acid and tannic acid to plant-seed derived biofuels improves the thermal and oxidative stability and viscosity of the canola biodiesel [21]. The poor oxidation stability, cloud and pour points of the karanja oil biodiesel was improved with natural additive derived from *T. cordifolia* stem [22].

The clove oil was used as natural antioxidant for the cotton seed oil biodiesel and the results shows that the oxidation stability increases with increase in addition of clove oil. The addition of clove oil to biodiesel increases the brake thermal efficiency by 4.71% at full load. Also it significantly affects the CO, HC, NO<sub>x</sub> and smoke emissions [23]. The higher alcohols such as decanol and hexanol can be used as partial subjects diesel.

The engine tests conducted with ternary blends of diesel-biodiesel- alcohols revealed that thermal efficiency of ternary blends were better than biodiesel. Also this ternary blends produces lower hydrocarbon, smoke, carbon monoxide emissions as compared to both biodiesel and diesel [24].

During the storage of biodiesel blends, microbial growth takes place and it may cause production biological mass at the interface of fuel-water. This affects the properties of the biodiesel blend and there is a chance of corrosion of tanks and pipes due to metabolism of these microorganisms which release acids [25]. Hence it is necessary to add additives to inhibit the microbial growth.

Barra et al. [26] reported that the chemical composition of eucalyptus oil changes depending on the origins and their study shows the major components of eucalyptus oil are spathulenol, 1,8-cineole, beta-phellandrene, cryptone and p-cymene. Their results show that the eucalyptus oil has antifungal activities at low doses and also it has better antioxidant activity. Huey-Chun Huang et al. [27] reported that the eucalyptus oil has better antioxidant characteristics and reduces the intracellular reactive oxygen species levels. It is also reported that the eucalyptus leaf oil can be used as antioxidant due to its ability to inhibit the free radicals [28].

Gitte Sørensen et al. [29] investigated the microbiological stability of biodiesel blends and their results show the bacterial growth in the incubations of fuel blends. Juan-Manuel Restrepo-Flórez [30] used a simulation work to study the influence of biodiesel on a microbial population and reported that the biodiesel has higher microbial growth. From this literature review, it is observed that the biodiesel is prone to oxidation and microbial growth deteriorate the properties of the biodiesel and hence suitable additive to be added to avoid these problems. Hence in this work, we have used eucalyptus oil as the additive and studied its effect on the compression ignition engine. The demand of edible oil is high in India and hence government of India promotes non-edible oils as biodiesel feedstock. Among available non-edible oils, neem oil has significant potential and also easily available in the market. However, the neem biodiesel has lower oxidation stability and hence in this study, engine tests were conducted to study the impact of eucalyptus oil on the neem biodiesel.

## **Materials and Methods**

The neem oil available in the open market was purchased and filtered to remove impurities. The acid value of the neem oil was estimated, and it was 64 mg KOH/gm. Hence the neem oil was subjected two step transesterification involving acid esterification and base transesterification, to produce biodiesel. The low-cost alcohol (methanol) was used as solvent. The sulfuric acid and potassium hydroxide were used as acid and base catalyst

respectively. The properties of the neem biodiesel like flash point, viscosity, density and calorific value were determined as per the ASTM methods and compared with the fossil diesel. The eucalyptus oil was mixed with the neem biodiesel with the concentration of 250, 500 and 750 ppm. A compression ignition engine was modified to work as experimental setup using suitable instrumentation. The engine trials were conducted to study the impact of eucalyptus oil on the engine exhaust emissions and performance.

The engine exhausts emissions such as CO, HC and NO<sub>x</sub> were measured and recorded using an MRU make (delta 1600 L model) exhaust gas analyzer. The infrared measurement technique was used to measure CO and HC emissions. An electro chemical sensor was used to measure NO<sub>x</sub> emission.

### Engine Test Setup

A series of engine tests were conducted on a four stroke, compression ignition engine which cooled by water. The details of the test engine are shown in the Table 1. The engine load was varied using a swinging field electrical dynamometer. For baseline data, engine experiments were conducted with diesel and important engine performance parameters and engine exhaust emissions were recorded after the engine reaches steady state condition and engine load was varied from no load to full load. After the engine tests, the fuel was changed, and similar procedure explained above was carried out and observations were recorded. Figure 1 shows the engine experimental setup.

Table 1: Test engine details

Item	Details
Make	Kirloskar
Model	TAF 1
Rated Power (kW) at 1500 rpm	4.4
Rated Speed (rpm)	1500
Compression Ratio	17.5 : 1
Injection Timing (degree)	23.4 degree bTDC
Injector Nozzle Opening Pressure (bar)	200
Fuel Injection	Direct Injection
Stroke X Bore (mm)	110 X 87.5
Other Details	Naturally aspirated CI Engine

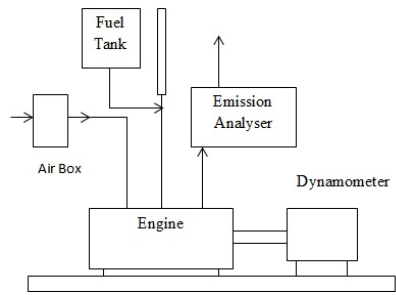


Figure 1: Engine experimental setup.

**Error Analysis**

The error analysis was carried out and the error of various instruments was shown in the Table 2.

Table 1: Error analysis

Instruments	Accuracy	% Uncertainty
Load measuring unit	± 0.1 kg	± 0.10
Fuel measuring unit	±0.1 cc	± 0.20
Digital stop watch	± 0.6 sec	±0.03
Speed measuring unit	± 10 rpm	± 0.10
EGT measuring unit	± 1°C	± 0.11

**Results and Discussion**

The neem oil was converted into biodiesel using two-step transesterification process. The fuel properties like flash point, density, dynamic viscosity and calorific value of the diesel, biodiesel and biodiesel added with eucalyptus oil were determined as per ASTM method. The transesterification reaction is shown in the Figure 2.

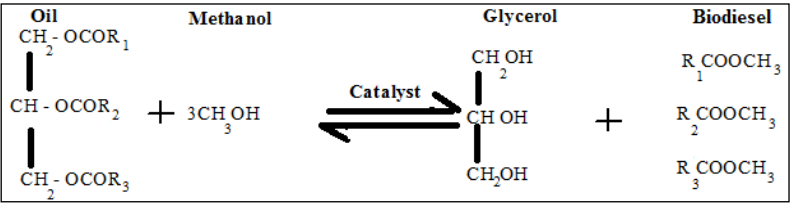


Figure 2: Transesterification Reaction

Table 3 compares important properties of the fuels. A slight difference in the properties is observed with biodiesel (B0) and biodiesel added with eucalyptus oil. Since the eucalyptus oil is added in terms of ppm, the variation of properties is small. However, the properties of diesel are better than the biodiesel.

Table 3: Comparison of fuel properties

Property	B0	B250	B500	B750	Diesel
Dynamic Viscosity (mm <sup>2</sup> /s)	4.8	4.8	4.84	4.89	3.5
Calorific Value (MJ/kg)	38.4	38.4	38.1	38	43.2
Flash Point (°C)	147	148	150	153	71
Density (kg/m <sup>3</sup> )	861	861	863	866	847

The engine tests were conducted with diesel, biodiesel and biodiesel with different concentrations of eucalyptus oil. The addition of eucalyptus oil affects the engine emissions and performance. The engine performance is represented by the term brake thermal efficiency which indicates how the energy possessed by the fuel is converted into mechanical energy. The impact of additive on the brake thermal efficiency of the diesel engine at various loads is indicated in Figure 3. Figure 3 shows that the engine's brake thermal efficiency increases with increase in engine load. Among the various fuels, the brake thermal efficiency is higher with diesel as the engine is designed for diesel. The brake thermal efficiency is lower with the neem biodiesel due to its lower volatility and slightly higher viscosity. The effect of eucalyptus oil on biodiesel is small at low loads. However, at higher loads, eucalyptus oil enhances the brake thermal efficiency. The brake thermal efficiency is lower with eucalyptus oil concentration of 750 ppm. However, the eucalyptus oil with the concentration of 500 ppm provides better thermal efficiency as compared to the 750 ppm.

The engine combustion temperature is directly influencing the engine exhaust gas temperature (EGT). The changes in EGT of the engine at different load with various fuels are depicted in Figure 4. The engine load affects the EGT and eucalyptus oil also impact the EGT. The higher fuel consumption at higher loads causes higher EGT at higher loads. The EGT is higher with biodiesel as compared to diesel fuel due to higher ignition delay period of the biodiesel. However, the addition of eucalyptus oil reduces the EGT of the engine. The variation in EGT of different eucalyptus oil concentration is small.

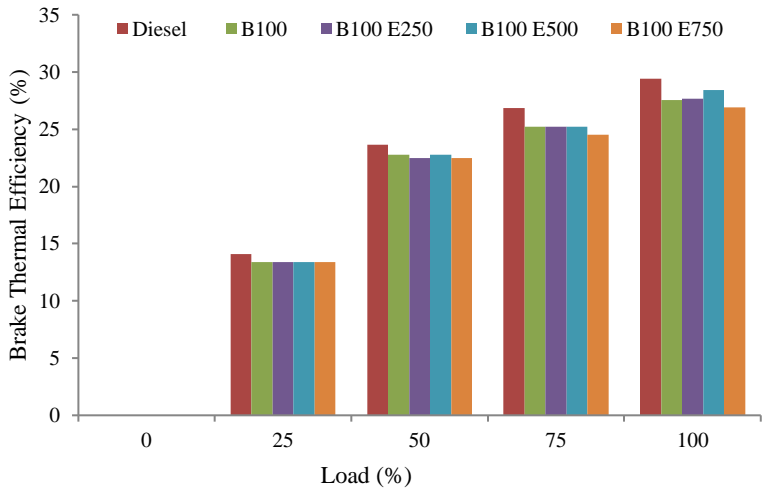


Figure 3: Brake thermal efficiency versus load.

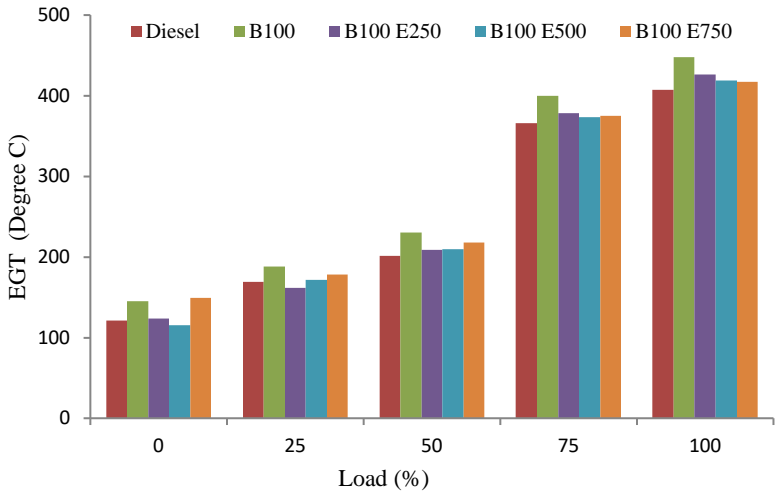


Figure 4: EGT versus load.

The impact of eucalyptus oil on engine un-burnt hydrocarbon (UBHC) emission is indicated in Figure 5. The engine consumes more amount of fuel to produce higher power. The higher fuel supply increases the UBHC emission. Figure 4 depicts that the engine UBHC emission increases with the

increase in the load and UBHC emission is high at higher loads. The biodiesel contains oxygen in its molecular structure and hence engine's UBHC with biodiesel is lower than the diesel fuel. At low loads, the variation in UBHC is low. However, the eucalyptus oil concentration of 500 ppm produces lower UBHC emissions as compared to the diesel and other concentrations. However, the additive concentration of 750 ppm causes higher UBHC with reference to other concentration.

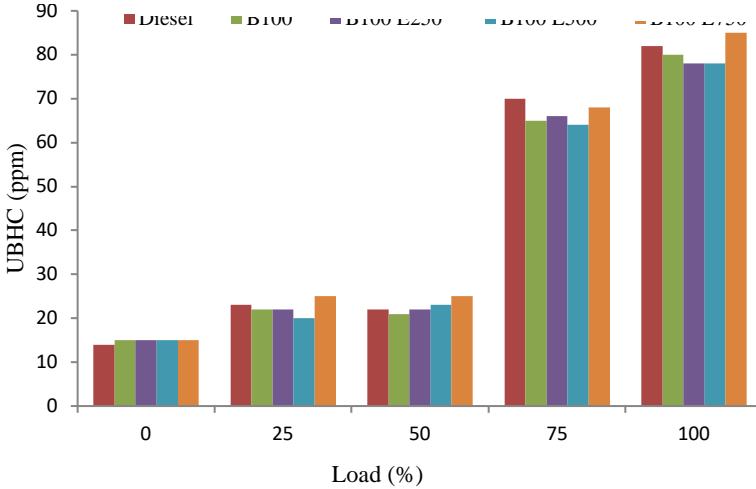


Figure 5: UBHC versus load.

The variation of engine's CO emission at various load is depicted in Figure 6. The CO emission indicates the incomplete combustion of the fuel in the engine. The engine's CO emission increases with the increase in the load. The biodiesel is an oxygenated fuel and hence engine's CO emission with biodiesel is lower than the diesel fuel. It is noticed that at higher loads, the CO emission of the biodiesel is lower than the biodiesel added with the eucalyptus oil. The higher eucalyptus oil concentration of 750 ppm provides higher CO emission.

The variation in engine's NOx emission with different fuels and at various engine loads is indicated in Figure 7. The engine's NOx emission increases with the increase in the engine load due to higher consumption fuel at higher loads. However, the engine's NOx emission is higher with biodiesel, and also at all loads. The additive added biodiesel significantly emits lower NOx emission with reference to neat biodiesel. The NOx emission is lower with the additive concentration of 750 ppm. The reduction



in NOx emission is due to the production of hydrocarbon free radicals which reduced the formation of NOx during combustion process.

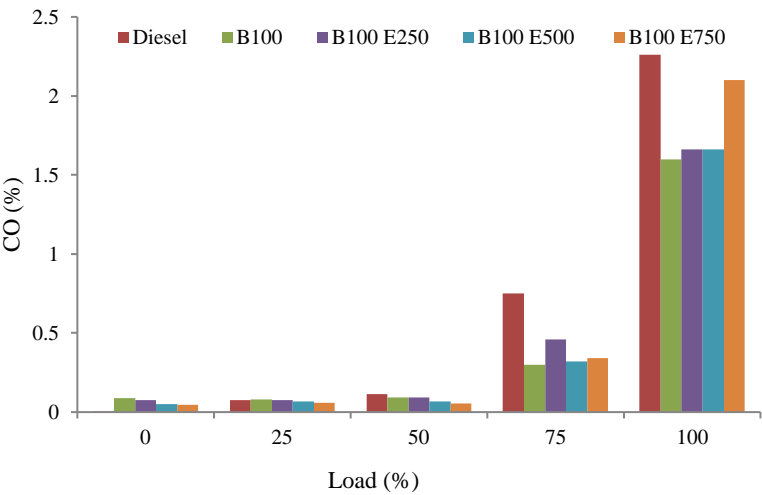


Figure 6: CO versus load.

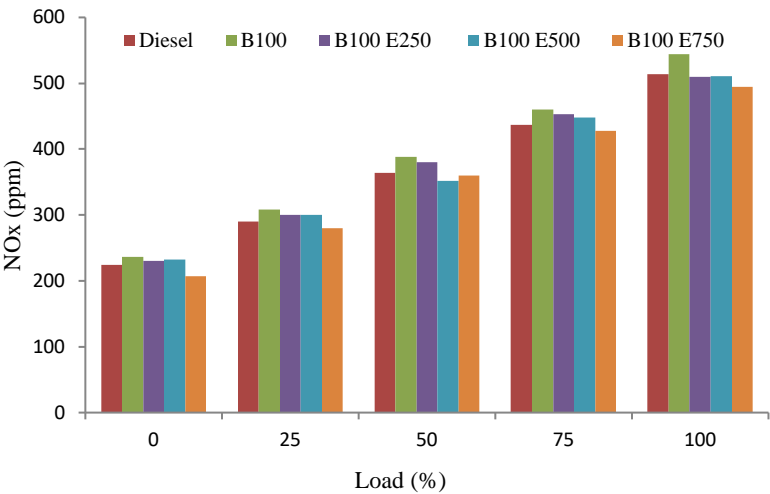


Figure 7: NOx versus load.

Conclusion

From the fuel property analysis, it was observed that the neem biodiesel properties were better than the raw oil and comparable to the diesel fuel. The viscosity of the raw oil was reduced drastically transesterification. The engine tests results show that the eucalyptus oil impact the thermal efficiency and performance of the diesel engine. The higher eucalyptus oil concentration of 750 ppm causes lower thermal efficiency. However other concentrations result in better thermal efficiency and engine performance at higher loads. The addition of eucalyptus oil with the concentration of 500 ppm results in 3.08 % increase in thermal efficiency at full load as compared to the biodiesel. Also, it was observed that eucalyptus oil concentration of 500 ppm reduces the carbon monoxide and unburnt hydrocarbon emissions as compared to other concentrations. A slight difference in NO<sub>x</sub> emission was observed with various concentrations of eucalyptus oil. Hence, we conclude from this work that the eucalyptus oil can be used as natural additive to the neem biodiesel.

## **Acknowledgment**

The work has been accomplished under the research project No. VTU/Aca/2009-10/A-9/11583, financed by the VTU Research Grant.

## **References**

- [1] Chedid, R., Kobrosly, M., Ghajar, R, “A supply model for crude oil and natural gas in the Middle East”, *Energy policy* 35, 2096–2109 (2007).
- [2] Shahriar, S., Topal, E, “When will fossil fuel re-serves be diminished?” *Energy Policy* 37, 181–189 (2009).
- [3] Report on All India Study Report to Petroleum Planning and Analysis Cell on sale of Diesel and Petrol, <http://pib.nic.in/newsite/PrintRelease.aspx?relid=102799> (Accessed on January, 15, 2019).
- [4] Christopher Frey, H, “Trends in on-road transportation energy and emissions”, *Journal of the Air & Waste Management Association* 68 (6), 514-563 (2018).
- [5] A report on International Energy Outlook 2008 Report <http://www.eia.doe.gov/emeu/cabs/India/Oil.htm> (Accessed on January, 15, 2019).
- [6] Idris Atadashi Musa, “The effects of alcohol to oil molar ratios and the type of alcohol on biodiesel production using transesterification process”, *Egyptian Journal of Petroleum* 25 (1), 21-31 (2016).

- [7] Avhad, M.R, Marchetti, J. M, “A review on recent advancement in catalytic materials for biodiesel production”, *Renewable and Sustainable Energy Reviews* 50, 696-718 (2015).
- [8] Faizan Ullah, Lisha Dong, Asghari Bano, Qingqing Peng, Jun Huang, “Current advances in catalysis toward sustainable biodiesel production”, *Journal of the Energy Institute* 89(2), 282-292 (2016).
- [9] Nurull Muna Daud, Siti Rozaimah Sheikh Abdullah, Hassimi Abu Hasan, Zahira Yaakob, “Production of biodiesel and its wastewater treatment technologies: A review”, *Process Safety and Environmental Protection* 94, 487-508 (2015).
- [10] Guven Gonca, Erinc Dobrucali, “Theoretical and experimental study on the performance of a diesel engine fueled with diesel–biodiesel blends”, *Renewable Energy* 93, 658-666 (2016).
- [11] Hyun KyuSuh, Chang Sik Lee, “A review on atomization and exhaust emissions of a biodiesel-fuelled compression ignition engine”, *Renewable and Sustainable Energy Reviews* 58, 1601-1620 (2016).
- [12] Wan Nor Maawa Wan Ghazali, Rizalman Mamat, H.H. Masjuki, Gholamhassan Najafi, Effects of biodiesel from different feedstocks on engine performance and emissions: A review, *Renewable and Sustainable Energy Reviews* 51, 585-602 (2015).
- [13] Abdul M., Gerpen van J.H, “The effect of biodiesel oxidation on engine performance and emissions”, *Biomass and Bioenergy* 20, 317–325 (2001).
- [14] Bouaid A., Martinez M. and Aracil J, “Long storage stability of biodiesel from vegetable and used frying oils”, *Fuel* 86 (16), 2596 – 2602 (2007).
- [15] N. Kapilan, T.P. Ashok Babu, R.P. Reddy, “Technical Aspects of Biodiesel and its Oxidation Stability”, *International Journal of ChemTech Research* 1 (2), 278-282 (2009).
- [16] Improved oxidative stability of biodiesel fuels, Report No: MIOH UTCAF4p2-5 2011, Michigan Ohio University Transportation Center project supported by the U.S, 2011.
- [17] Ana Carolina Roveda, Marina Comin, Anderson Rodrigues Lima Caires, Valdir Souza Ferreira, Magno Aparecido Gonçalves Trindade, “Thermal stability enhancement of biodiesel induced by a synergistic effect between conventional antioxidants and an alternative additive”, *Energy* 109, 260-265 (2016).
- [18] Gabriela Menegon Buosi, Elisangela Tavares da Silva, Kelly Spacino, Livia Ramazzoti Chanan Silva, Bruna Aparecida Denobi Ferreira, Dionisio Borsato, “Oxidative stability of biodiesel from soybean oil: Comparison between synthetic and natural antioxidants”, *Fuel* 181, 759-764 (2016).
- [19] Rashed, M. , M. Masjuki, H.H., Kalam, M.A, Abdullah Alabdulkarem, Rahman, M.M, Imdadul, H.K. Rashedul. H.K, “Study of the oxidation

- stability and exhaust emission analysis of Moringaolifera biodiesel in a multi-cylinder diesel engine with aromatic amine antioxidants”, *Renewable Energy* 94, 294-303 (2016).
- [20] Freitas, João Paulo Almeida, et al. “Cottonseed Biodiesel Oxidative Stability in Mixture with Natural Antioxidants.” *Korean Journal of Chemical Engineering*, 36 (8), 1298–1304 (2019).
- [21] Borugadda, Venu Babu, et al. “Effects of Natural Additives on Performance of Canola Biodiesel and Its Structurally Modified Derivatives.” *Industrial Crops and Products* 125, 303–313 (2018).
- [22] Kumar, Dipesh, and Bhaskar Singh. “Effect of Winterization and Plant Phenolic-Additives on the Cold-Flow Properties and Oxidative Stability of Karanja Biodiesel,” *Fuel* 262, 116631 (2020).
- [23] Jeyakumar, Nagarajan, and Bose Narayanasamy, “Clove as Antioxidant Additive in Diesel-Biodiesel Fuel Blends in Diesel Engines,” *International Journal of Green Energy* 16 (4), 284–292 (2019).
- [24] Ashok, B., et al. “Comparative Assessment of Hexanol and Decanol as Oxygenated Additives with Calophyllum Inophyllum Biodiesel,” *Energy* 173, 494–510 (2019).
- [25] Sabrina A. Beker, Maria Elisabete Machado, Gabriela P. S. Maciel, Rosângela Silva, Renato Cataluña, Elina B. Caramão, Fatima M. Bento, “Antimicrobial Potential of Bio-Oil for Use in Diesel Oil B10”, *Journal of the Brazilian Chemical Society* 27(1), (2016).
- [26] Barra, A., Coroneo, V., Dessi, S., Cabras, P., Angioni, A., “Chemical variability, antifungal and antioxidant activity of *Eucalyptus camaldulensis* essential oil from Sardinia”, *Natural Product Communications* 5(2), 329-35 (2010).
- [27] Huey-Chun Huang, Ya-Chi Ho, Jia-Min Lim, Tzu-Yun Chang, Chen-Lung Ho, Tsong-Min Chang, Investigation of the Anti-Melanogenic and Antioxidant Characteristics of *Eucalyptus camaldulensis* Flower Essential Oil and Determination of Its Chemical Composition, *International Journal of Molecular Sciences* 16, 10470-10490 (2015).
- [28] Arun, K., Mishra Neelum Sahu, Amrita Mishra, Ashoke K.Ghosh, Shivesh Jha, Pronobesh Chattopadhyay, “Phytochemical Screening and Antioxidant Activity of essential oil of *Eucalyptus* leaf”, *Pharmacognosy Journal* 2 (16), 25-28 (2010).
- [29] Gitte Sørensen, Dennis V.Pedersen, Anna K.Nørgaard, Ketil B.Sørensen, Sune D.Nygaard, “Microbial growth studies in biodiesel blends”, *Bioresource Technology* 102 (8), 5259-5264 (2011).
- [30] Juan-Manuel Restrepo-Flórez, Amarjeet Bassi, Lars Rehmann, Michael R.Thompson, “Effect of biodiesel addition on microbial community structure in a simulated fuel storage system”, *Bioresource Technology* 147, 456-463 (2013).



# Experimental Study on Translation Motion Characteristics of Moored Symmetrical Semi-submersible in Regular Waves

*Khairuddin, N.M.<sup>1,2,3</sup> \*, Jaswar Koto <sup>2,3</sup>, Nur Ain, A.R.<sup>1</sup>, Mohd Azhari, J.<sup>1</sup>, Najmie, A.<sup>1</sup>*

*<sup>1</sup> Faculty of Mechanical Engineering, Universiti Teknologi MARA, Malaysia*

*<sup>2</sup> Department of Aeronautic, Automotive and Ocean Engineering,  
Universiti Teknologi Malaysia Skudai, Malaysia*

*<sup>3</sup> Ocean and Aerospace Research Institute, Pekan Baru, Riau, Indonesia*

*\* nmkhairuddin@uitm.edu.my*

## ABSTRACT

*This paper proposes to carry out experiment procedures to investigate the translation motion characteristics of symmetrical semi-submersibles in long crest regular waves. The hydrodynamic response of floating structures in waves is required to be modelled correctly to ensure stability and safety. The symmetrical semi-submersible model was constructed based on a scale ratio of 1:81 in this experiment and was installed with horizontal mooring lines in a wave dynamic basin. This paper also discusses the model preparation procedures, including the mooring lines setup, instrument setup and experiment setup, before conducting the experiment. According to the experiment data, the symmetrical moored semi-submersible experienced wave frequency motion and slow varying motion due to drift force and mooring lines for sway motion; while the heave and surge motion only experienced wave frequency motion.*

**Keywords:** *Hydrodynamic Response; Semi-submersible; Wave Crest; Short Crest Wave; Long Crest Wave*

## Introduction

Semi-submersible offshore production platforms are an alternative for deep sea crude oil drilling. Compared to jacket or fixed-type platforms, semi-submersibles can operate with a self-floating structure. In 2016, the operation

of semi-submersibles covered 40% of total offshore structures worldwide, serving as drilling and production systems [14].

Sharma et al. [14] reviewed and reported that the process of design has evolutionary reliance on challenges of operating depth. However, an evolution of process design must be followed by a detailed analysis and has various options. Besides, semi-submersibles only require low initial investment and operating costs, since the platform contains small waterline areas. Research by Rudman and Cleary [12] states that an analysis of influences of the mooring system is necessary during the design stage. Since the platform is positioned and anchored through the mooring system, the structure may experience large low frequency (LF) motions, defined as slow-drift motions under nonlinear low frequency wave forces excitation. Meanwhile, the wave frequency forces excitation may cause significant dynamic responses by the platform. These excitations are sensitive to different types of mooring systems.

Previous research by Islam et al. [5] exposed a method to find the dynamic behaviour of offshore structures. Some researchers investigated the pitch instability of deep draft semi-submersible drafts in irregular waves, in realistic sea conditions [10]. In the past few years, researchers such as Hong et al. [4], Montasir et al. [11] and Chen et al. [2], have revealed the coupling effects between floating offshore structures and the mooring system. These coupling effects could be predicted in their motion and analyses, in terms of time and frequency [17]. The need for coupled analysis has long been recognized [8]. Research by Low and Langley [9] introduced couple analysis tools. The numerical analysis of nonlinear couple dynamic responses of Spar platforms under regular sea waves has been covered by Agarwal and Jain [1].

Coupled dynamic analysis technique for fully couple dynamics has been developed using the quasi static approach. Chen et al. [3] calculated the motions of a spar and its mooring system in three different water depths by using a quasi-static approach and a coupled dynamic approach. The present genetic algorithm to optimize the mooring design of floating platforms has been investigated by Shafieefar and Rezvani [13]. Siow et al. [15] predicted the semi-submersible's motion response by using diffraction potential theory and heave viscous damping correction. They contribute some improvement to predict the heave responses of semi-submersibles with diffraction potential by linearized the Morison drag [16].

The horizontal mooring system attached above water level does not represent a practical method of mooring but is rather used to study the loading on and response of the semi-submersible, in the absence of the catenary mooring lines. This leads to a better understanding of the effects of the catenary mooring lines on the damping and motion responses. The idea of the horizontal mooring system has been used by Khairuddin et al. [6] to present the mooring lines force behaviour of semi-submersibles in regular waves to reveal the behaviour of mooring lines in terms of time and

frequency. They also conducted physical model testing for semi-submersibles using a horizontal mooring lines system to investigate the added mass and heave damping behaviour in regular waves [7].

The horizontal mooring system in physical model testing is where the structure is moored using horizontal springs that are attached to the structure above the water surface level. Such a system does not have practical usage. However, the investigation of the responses of the structure moored with horizontal springs can be investigated as being influenced by the damping of only the hull. Hence, differences between the responses of the semi-submersible model when moored via horizontal springs to those when moored using catenary mooring systems, were considered due to the mooring lines.

## **Experimental Approach**

There are five part of experimental approach will be described in this section. The first part describes the law of similarity. Second part describes the model preparation while the third part explain the instrument that were used in the experiment. The fourth and last part describes the mooring lines setup and the experimental setup.

### **Law Similarity Outline**

In this study, the semi-submersible model and mooring line are scaling based on the Froude Number and Strouhal Number similarity. This means that the model and prototype have similarity in terms of Froude Number and Strouhal Number (gravitational force and inertia force is satisfied). Froude's law of similarity is the most appropriate scaling law applicable for the moored and unmoored floating structure experiments.

Typically, the effect of viscous is ignored for the motions of ship or ocean engineering structures among waves. In the present tests, the Froude Number and Strouhal Number of the model and prototype are kept the same, which means the similarity of the gravitational force and inertia force is satisfied, as Equation (1) and Equation (2) follows:

$$\frac{V_m}{\sqrt{gL_m}} = \frac{V_p}{\sqrt{gL_p}} \quad (1)$$

$$\frac{V_m T_m}{L_m} = \frac{V_p T_p}{L_p} \quad (2)$$

where  $V$ ,  $L$  and  $T$  represent velocity, linear dimension and the motion period of the body respectively. The subscripts  $m$  and  $p$  denote the variables for the model and prototype respectively.



Based on Equation (1) law of similarity, the relationships of physical variables between the prototype and model are listed in Table 1, where  $\lambda$  means linear scale ratio and  $\gamma$  means specific gravity of seawater ( $\gamma = 1.025$ ).

Table 1: Scaling Law between the prototype and model

Item	Symbol	Scale Ratio
Linear Dimension	$L_p/L_m$	$\lambda$
Linear Velocity	$V_p/V_m$	$\lambda^{1/2}$
Angle	$\phi_p/\phi_m$	1
Period	$T_p/T_m$	$\lambda^{1/2}$
Area	$A_p/A_m$	$\lambda^2$
Volume	$\nabla_p/\nabla_m$	$\lambda^3$
Moment Inertia	$I_p/I_m$	$\gamma\lambda^5$
Force	$F_p/F_m$	$\gamma\lambda^3$

### Model Preparation

In this study, the symmetrical semi-submersible (Figure 1) was designed and constructed so that it can be tested in a water basin to simulate the characteristic of translation motion. This symmetrical semi-submersible model was constructed based on a full-scale model. In this experiment, the symmetrical semi-submersible model was scaled down with the ratio of 1:81.

After completing the model construction, several tests were conducted to ensure the model is coherent to the prototype design. Firstly, the inclining test, swing test (Figure 2) and decay test were carried out to identify the hydrostatic particular for the symmetrical semi-submersible model. This was performed to determine the natural period, vertical center of gravity of the model (KG), metacentric (GM) and the radius of gyration for pitch and roll.

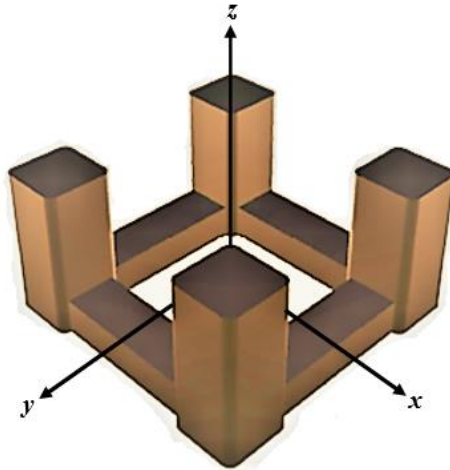


Figure 1: Symmetrical Semi-submersible

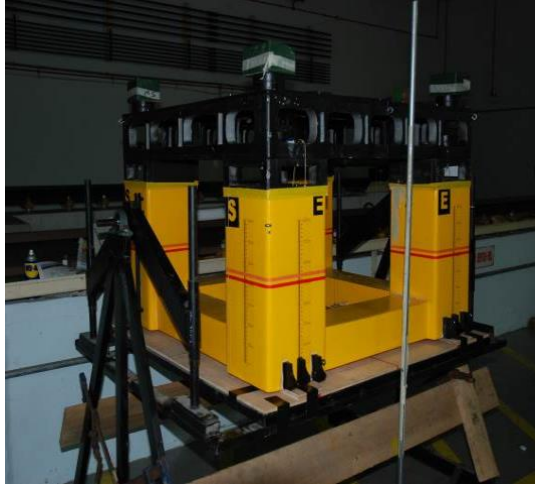


Figure 2: Swing test to calibrate its center of gravity

Throughout the model preparation from the experiment, the analysis of the results was done by measuring the parameter and values which are obtained from the test. Table 2 shows the summary of results of model preparation test conducted.

Table 2: Summary from the model preparation

Description	Model	Prototype	Unit
Mass displacement, $\Delta$	0.112	58748	M.tonne
Overall draft, $d$	0.271	22	m
Center of gravity above base, $KG$	0.387	31.347	m
Center of buoyancy above base, $KB$	0.1	8.1	m
Metacentric height above base, $KM$	0.489	39.609	m
Metacentric, $GM$	0.0896	7.268	m
Metacentric above center of	0.389	31.509	m
Pitch radius of gyration, $K_{yy}$	0.448	36.32	m
Roll radius of gyration, $K_{xx}$	0.434	35.22	m
Heave Period, $T_h$	2.03	18.27	s
Pitch Period, $T_p$	3.39	30.51	s
Roll Period, $T_r$	3.34	30.06	s
Moment of Inertia, $I_r$	0.389	31.509	m4

Mass moment of inertia for pitch, $I_{yy}$	0.021	72.87	M.tonne.m <sup>2</sup>
Mass moment of inertia for roll, $I_{xx}$	0.023	77.50	M.tonne.m <sup>2</sup>
Mooring stiffness, $k$	0.008	69.0	kN/m

### Instrument of Model Test

The symmetrical semi-submersible was assumed to have six degrees of freedom during the experiment. Wave probe (Figure 3) of resistance was employed and attached to the model to measure the generated wave elevation during the test.

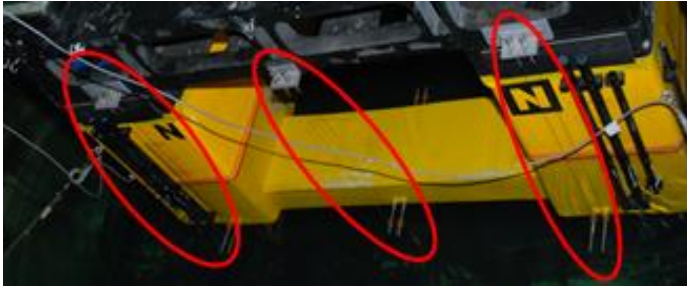


Figure 3: Wave probe to measure the wave elevation

The optic tracker (Figure 4) used was Qualysis, which is a high-speed camera used to capture the motion from the ball maker (Figure 5) that has been fixed onto the model. Once the ball maker that is attached to the model makes a movement, the optic tracker or high-speed camera captures the motion and records the amplitude motion of the symmetrical semi-submersible.



Figure 4: Optic tracker to capture the motion of ball maker



Figure 5: Ball maker

The translation motion in the X, Y and Z axis of the symmetrical semi-submersible has been recorded on a computer device using Qualysis Track Manager (Figure 6) in a time domain series.

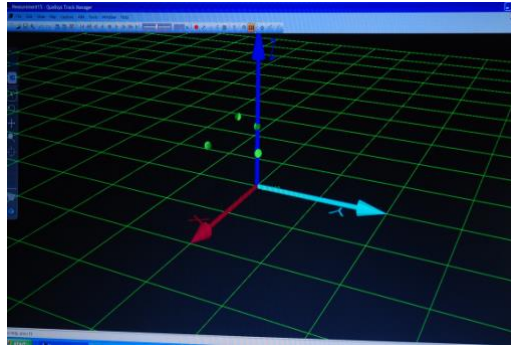


Figure 6: Qualysis Track Manager to record the motion of marker

### Mooring Line Setup

Steel springs which connected with a force transducer were used to simulate the mooring line of the moored semi-submersible. The semi-submersible has a mooring system arranged in four lines, with springs attached in such a way that the horizontal spring stiffness is 0.08 N/m, corresponding to the prototype value of 69 kN/m. The soft springs used must be calibrated to suit the required spring stiffness of 0.08 N/m. The achieved spring stiffness is shown in Table 3. The schematic arrangement of the springs to the model is shown in Figure 7.

Table 3: Summary of spring stiffness

Spring	Column	Stiffness (N/m)
S1	North West(NW)	0.0794
S2	North East (NE)	0.0794
S3	South East (SE)	0.0791
S4	South West (SW)	0.0798

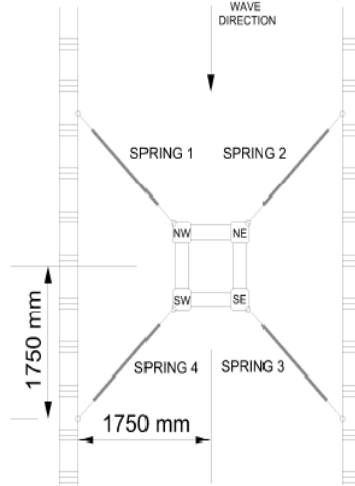


Figure 7: Schematic arrangement

### Experimental Setup

The symmetrical semi-submersible model was attached to the towing carriage, which carries recording equipment that is fixed at 60 m from the wave generator. One wave probe (wave gauge) was fixed to the model to measure the generated wave elevation during tests. Symmetrical semi-submersibles are set so that the North West Column and North East Column face the wave direction.

Before the test, the mooring spring is attached to the axial riser and column. Mooring lines were calibrated so that the stiffness becomes 0.08 N/m by attaching the ring gauge at the end of the spring, at the column side. The ring gauge (Figure 8) measures the load acting on the mooring line.

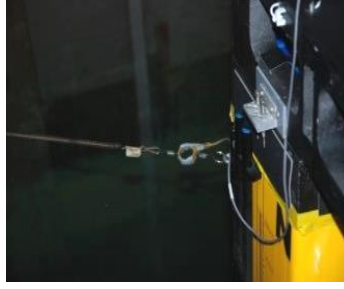


Figure 8: Ring gauge attached to the model

The experiments were conducted under regular waves for head sea conditions in the frequency range of 0.429 Hz to 1.7189 Hz, in steps of 0.1433 Hz, according to the capability of the wave generator. Table 4 shows the frequency of oscillation that has been chosen with the constant wave height of 0.0988 m.

Table 4: Model wave condition

$f$ (Hz)	$T_w$ (s)	$L_w$ (m)
0.4297	2.3271	8.4552
0.573	1.7453	4.756
0.7162	1.3963	3.0439
0.8594	1.1636	2.1138
1.0027	0.9973	1.553
1.1459	0.8727	1.189
1.2892	0.7757	0.9395
1.4324	0.6981	0.761
1.5756	0.6347	0.6289
1.7189	0.5818	0.5284

The wave generator was initiated when the wave passes through the model, and the optic tracker starts the recording process. The measurement recorded up to about 120 seconds. All the data were obtained using the Qualysis Tracker Manager.

## Result and Discussion

In this study, the translation motion in the X, Y and Z axes is consider as a Sway, Surge and Heave motion respectively. The collected time domain samples are presented in Figures 9 to 11, which present the surge, sway and

heave motions of the symmetrical semi-submersible, respectively, in time series collected from the model experiment.

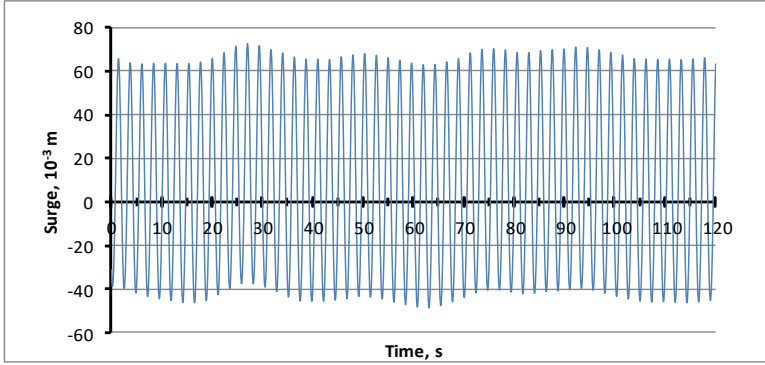


Figure 9: Surge motion in time series from model experimental at wave frequency 0.4297 Hz and wave height 0.0988 m

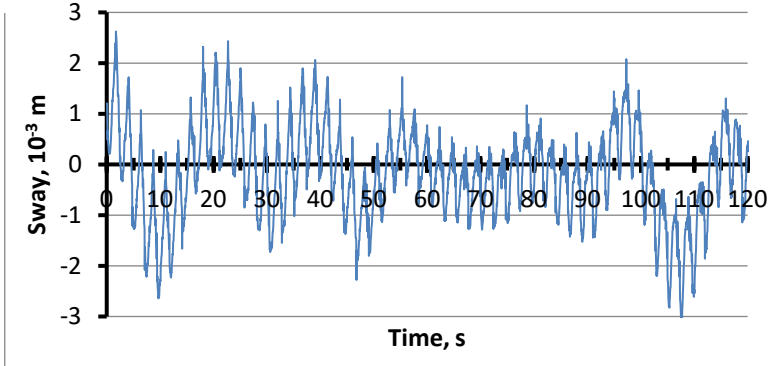


Figure 10: Sway motion in time series from model experimental at wave frequency 0.4297 Hz and wave height 0.0988 m

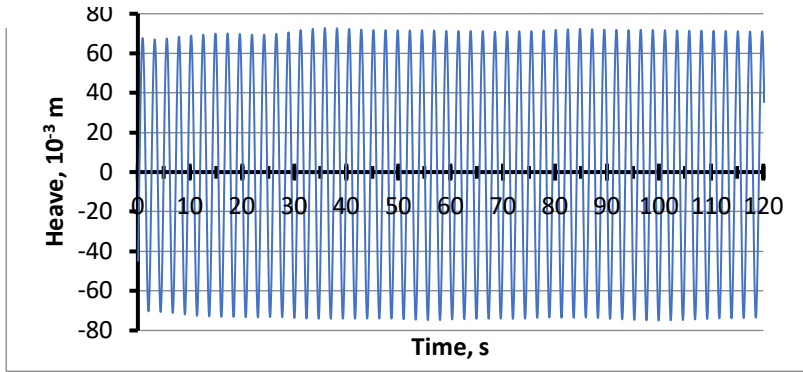


Figure 11: Heave motion in time series from model experimental at wave frequency 0.4297 Hz and wave height 0.0988 m

According to Figure 10, the sway motion experienced the wave frequency motion at this wave condition. The effect of drift force and mooring lines is significant to the pattern of sway motion in this head wave condition; it caused the semi-submersible to experience a continuous slow varying motion from the port to the starboard.

The slow varying motion can be observed from every peak point of sway motion in Figure 10. In terms of magnitude, sway motion demonstrated good characteristics, since the value is insignificant compared to the surge and heave motion. The maximum amplitude of sway motion in Figure 10 is around 0.003 m. With this magnitude, it has showed the effects of sway motion are very insignificant to the mooring lines tensions. To keep their positioning during the operation due to sway effect, this type of floating structure showed the good performance.

According to Figure 9, the effect of the mooring lines tensions caused a difference in the amplitude of the surge motion between forward and aft of semi-submersible, which looks significant for this wave heading condition. The amplitude for forward and aft are around 0.07 m and 0.05 m respectively. This behaviour has showed that, the mooring lines tension reach the peak point frequently in wave heading conditions. This surge motion only experienced the wave frequency motion.

Compared to the sway motion, the motion of surge and heave only experienced the wave frequency motion. According to Figure 11, the amplitude of heave motion is around 0.07 m. At this wave frequency, the heave motion experienced the resonance, where the computed heave RAO is around 1.42. These translation motions show that the symmetrical semi-submersible has good dynamic behaviour in a wave frequency of 0.4297 Hz.



## Conclusions

This paper presented an experimental technique to investigate the hydrodynamic behaviour of moored semi-submersibles in regular waves. In the experiment, the symmetrical semi-submersible was setup in wave heading conditions scaled down from the full-scale size. The examples of time series motion data collected from the model experiment in a wave frequency of 0.4297 Hz and wave height 0.0988 m, were detailed in the paper. The sway motion of symmetrical semi-submersibles experienced two types of motions, namely, slow varying motion and wave frequency motion. In addition to collecting the samples of time series data, it also showed that the experiment was successful to capture the motion response of the symmetrical semi-submersible model due to the incoming or heading waves condition.

## Acknowledgement

The authors are very grateful to Marine Technology Center of Universiti Teknologi Malaysia, for supporting this study.

## References

- [1] R. Sharma, Tae Wan Kim, O. P. Sha, and S. C. Misra, "Issues in Offshore Platform Research - Part 1: Semi-Submersibles." *International Journal of Naval Architecture and Ocean Engineering* 2 (3), 155–70 (2010).
- [2] Rudman, Murray and Paul W. Cleary, "The Influence of Mooring System in Rogue Wave Impact on an Offshore Platform," *Ocean Engineering* 115, 168–81 (2016).
- [3] Islam, A. B. M. Saifu., Mahmudur Rahman Soeb, and Mohd Zamin Bin Jumaat, "Floating Spar Platform as an Ultra-Deepwater Structure in Oil and Gas Exploration," *Ships and Offshore Structures* 12 (7), 923–36 (2017).
- [4] Mao, Huan and Hezhen Yang, "Parametric Pitch Instability Investigation of Deep Draft Semi-Submersible Platform in Irregular Waves," *International Journal of Naval Architecture and Ocean Engineering* 8 (1), 13–21 (2016).
- [5] Hong, Sinpyo et al., "An Experimental Study of the Effect of Mooring Systems on the Dynamics of a SPAR Buoy-Type Floating Offshore Wind Turbine," *International Journal of Naval Architecture and Ocean Engineering* 7 (3), 559–79 (2015).

- [6] O. A. Montasir, A. Yenduri, and V. J. Kurian, "Effect of Mooring Line Configurations on the Dynamic Responses of Truss Spar Platforms," *Ocean Engineering* 96, (2015).
- [7] P. Chen, S. Chai, and J. Ma. "Performance Evaluations of Taut-Wire Mooring Systems for Deepwater Semi-Submersible Platform," *Proceedings of the International Conference on Offshore Mechanics and Arctic Engineering - OMAE 6*, 207–15 (2011).
- [8] M. Yang, B. Teng, D. Ning, and Z. Shi, "Coupled Dynamic Analysis for Wave Interaction with a Truss Spar and Its Mooring Line/riser System in Time Domain," *Ocean Engineering* 39, 72–87 (2012).
- [9] J. Y. Lee, and S. J. Lim, "Hull Form Optimization of a Tension-Leg Platform Based on Coupled Analysis," *Proceedings of the Eighteenth International Offshore and Polar Engineering Conference*, 1 (8), 100–107 (2008).
- [10] Y. M. Low, and R. S. Langley, "Time and Frequency Domain Coupled Analysis of Deepwater Floating Production Systems," *Applied Ocean Research* 28 (6), 371–85 (2006).
- [11] Agarwal, A. K. and A. K. Jain, "Nonlinear Coupled Dynamic Response of Offshore Spar Platforms under Regular Sea Waves," *Ocean Engineering* 30 (4), 517–51 (2003).
- [12] Chen, Xiaohong, Jun Zhang, and Wei Ma, "On Dynamic Coupling Effects between a Spar and Its Mooring Lines," *Ocean Engineering* 28 (7), 863–87 (2001).
- [13] Shafieefar, Mehdi and Aidin Rezvani, "Mooring Optimization of Floating Platforms Using a Genetic Algorithm," *Ocean Engineering* 34 (10), 1413–21 (2007).
- [14] C. L. Siow, Jaswar Koto, Hassan Abby, and N. M. Khairuddin. "Prediction of Semi-Submersible's Motion Response by Using Diffraction Potential Theory and Heave Viscous Damping Correction." *JurnalTeknologi (Sciences and Engineering)* 69 (7), 127–133 (2014).
- [15] Siow, C. L., Jaswar Koto, Hassan Abyn, and N. M. Khairuddin, "Linearized Morison Drag for Improvement Semi-Submersible Heave Response Prediction by Diffraction Potential," *Journal of Ocean, Mechanical and Aerospace -Science and Engineering* 6 (2014).
- [16] N. M. Khairuddin, M. Pauzi, and J. Koto, "Experimental Analysis on the Mooring Lines Force Behaviour of Semi-Submersible in Regular Waves," *Jurnal Teknologi (Sciences and Engineering)* 69 (7), (2014).
- [17] Khairuddin, N. M. and Mohamad Pauzi, "Experimental Investigation of Motion and Wave Induced Forced on Semi-Submersible in Regular Wave," *Journal of Ocean, Mechanical and Aerospace-Science and Engineering* 9, (2014).

# Spiral Toolpath Definition and G-code Generation for Single Point Incremental Forming

Zeradam Yeshiwas\*, A. Krishniah

Department of Mechanical Engineering, College of Engineering,  
Osmania University, Hyderabad, India

\*zeruhulu@gmail.com

## ABSTRACT

*The research to date has not been able to confirm earlier findings showing the commercial availability of the tool path definition package for Single Point Incremental Forming (SPIF). There has been substantial research undertaken on the tool-path definition for SPIF by using CAM package or Matlab script. However, the coordinate points from Matlab must get changed to G-code to introduce in the CNC mill. Previous studies on SPIF have not dealt with the conversion of Matlab script into G-code. In the current study, a methodology has been proposed to convert the tool path trajectories generated using Matlab script into G-code. Three different shapes i.e. the truncated cone, pyramid, and hyperbola were chosen for the definition of tool-path trajectory. The method was tested using Simco edit software and successfully working. This study fills a gap in the literature by introducing a method to convert Matlab script into G-code.*

**Keywords:** SPIF; Toolpath Definition; Numerical Simulation; Spiral Toolpath; G-code Generation

## Introduction

Single point incremental forming (SPIF), is a relatively new process for manufacturing sheet metal parts. It is well suited for small batch production or prototyping. It can be executed by using a CNC mill. It has a high potential economic payoff [1]-[3]. Based on recent reviews, SPIF is on the progress of industrialization. A CAM package with the feature for the tool-path definition of SPIF has not been introduced [4].

Two of the most common methods for the definition of tool path are the contour and the spiral. The contour tool path uses CAM packages whereas; the spiral tool path uses CAM or programming script. The profile tool path created by using a CAM package can produce complex geometry but it produces scarring on the surface of the part. The helical tool path is more suitable for Incremental Sheet Forming (ISF). It completely eliminates scarring on the surface of the formed part and produces homogeneous thinning [5].

Studies have shown that tool-path created in Matlab script has widely used for the numerical simulation of SPIF [5,6]. In contrast, the CAM developed toolpath has been using for an experimental investigation [7]-[9]. CNC mill does not accept the coordinate points created from Matlab. That is because G-code is the programming language for CNC that instructs machines where and how to move. Because of this, the coordinate points from Matlab must get changed to G-code to introduce in the CNC Mill.

Prior studies have not been able to establish a method to convert coordinate points into G-code. In this study, a method to convert the coordinate points into G-code has introduced. The results of this experiment were found to be satisfactory.

## Methodology

Figure 1 shows the procedures followed to get a 3D line plot of the required sample part and conversion of the coordinate points into G-code.

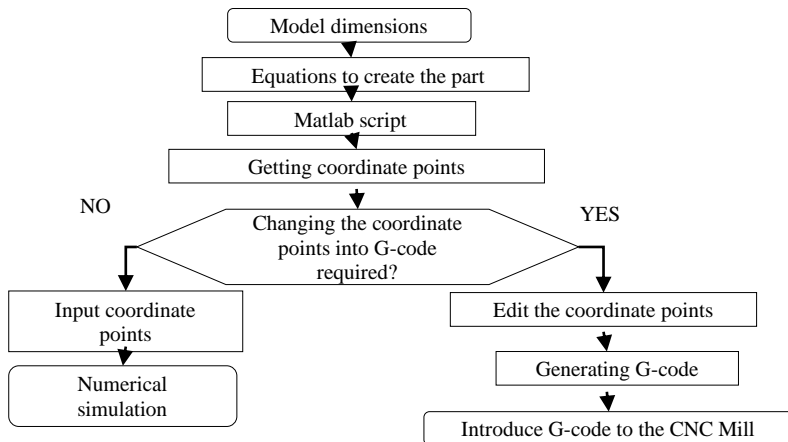


Figure 1: Method used for the tool-path definition and G-code generation

### Sample Parts

The first sample part used in this study is the truncated cone. The basic parameters required to formulate the truncated cone are depicted in Figure 2.

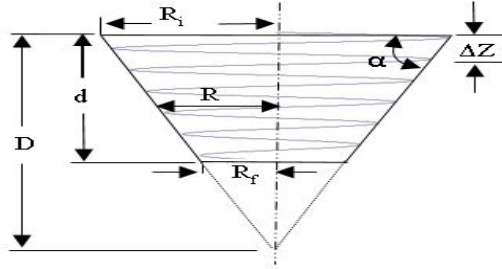


Figure 2: Parameters to formulate the truncated cone

Equations (1)–(5) are used for the formulation of the truncated cone.

$$\Delta r = \frac{\Delta Z}{\tan(\alpha)} \quad (1)$$

$$N = \frac{d}{\Delta Z} \quad (2)$$

$$X = R \cos(\theta) \quad (3)$$

$$Y = R \sin(\theta) \quad (4)$$

$$Z = -\left(\left(\frac{\Delta Z}{360}\right)\theta\right) \quad (5)$$

This section has attempted to provide the Matlab script that used to define the spiral tool-path for the truncated cone. The “plot 3” function was used to create a three-dimensional plot. Figure 3 depicts the isometric view of the Truncated cone.

```
clear
clc
dh=0.5;    %step depth
a=45;      %angle of inclination of the cone
h=30;      %Depth of the cone
Rl=50;     %largest radius of the cone (top part)
D=Rl*tand(a);
N=h/dh;    %Number of loops or contour
m=1;
for n=0:1:360*N %dividing a loop into 360 angles
```

```

Z(m)=0-((dh/360)*n);
R=R1-(((dh/360)*n)/tand(a)); %radius at anydepth
X(m)=R*cosd(n);
Y(m)=R*sind(n);
m=m+1;
end
plot3(Y, X, Z,'b') % 3D visualization of helix

```

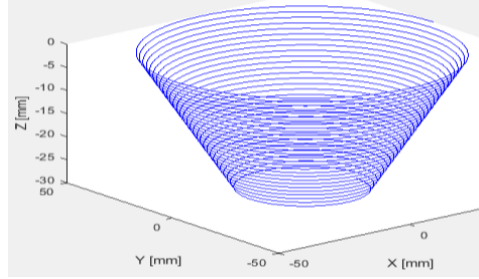


Figure 3: Isometric view of the truncated cone

The second sample part is Hyperbola. The parameters used to formulate this part are presented in Figure 4.

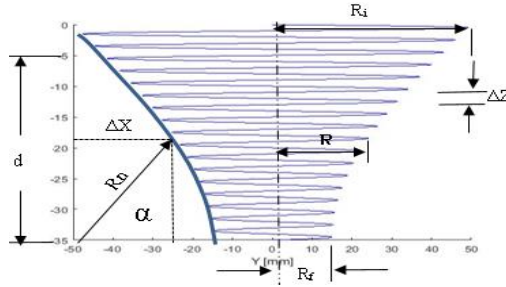


Figure 4: Parameters to formulate the Hyperbola

The number of loops and the coordinate points of X, Y and Z are defined by using equations (2) – (5). Equations (6) – (9) are used to formulate the rest of the parameters.

$$\Delta x = R_n \cos \alpha \quad (6)$$

$$R = R_i - \Delta X \quad (7)$$

$$\Delta R = \frac{\pi}{2(360 \cdot N)} \quad (8)$$

$$\beta = \frac{\pi}{2} - (\Delta R \cdot \theta) \quad (9)$$

This section has attempted to provide the Matlab script used to define the spiral tool-path for the hyperbolic part. Figure 5 depicts the isometric view of the hyperbola.

```

clc
clear
% NOTE: input parameters: dh, h, R1, r1
dh=1;      %Step Depth
h=30;      %depth of the hyperbola
R1=50;     %Initial radius of the circle
r1=h;
N=h/dh;    %Number of loops
m=1;
Ra=pi/(2*360*N); %change in radius on the arc
within one loop

for n=0:1:360*N
    theta=(pi/2)-(Ra*n); %change in angle on the arc
    z(m)=0-((dh/360)*n);
    R=R1-r1*cos(theta); % Radius at any intermediate
    step
    y(m)=R*sind(n);
    x(m)=R*cosd(n);
    m=m+1;
end
plot3(x,y,z,'b-') % 3D visualization of helix

```

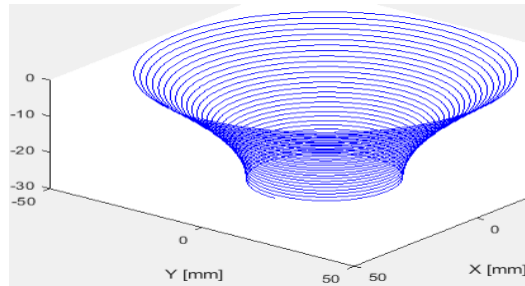


Figure 5: Isometric view of the hyperbola

The third sample part is the truncated pyramid. The parameters used to formulate this part are presented in Figure 6.

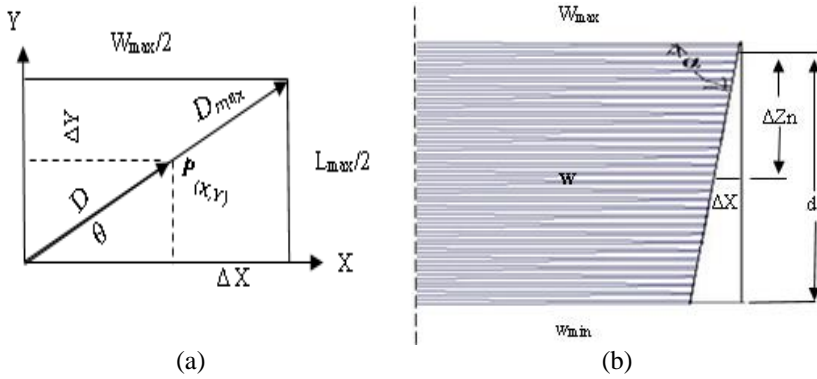


Figure 6: Parameters for the truncated pyramid; a) top view b) front view

The number of loops and values for the coordinate point Z are defined by using equations (2) and (5). Equations (10) – (14) are used to formulate the rest of the parameters for the truncated pyramid.

$$\Delta X = \frac{\Delta Z_n}{\tan(\alpha)} \quad (10)$$

$$D_{max} = \sqrt{\left(\frac{L_{max}}{2}\right)^2 + \left(\frac{W_{max}}{2}\right)^2} \quad (11)$$

$$D = D_{max} - \Delta X \quad (12)$$

$$X = D \cdot \cos(\theta) \quad (13)$$

$$Y = D \cdot \sin(\theta) \quad (14)$$

This section has attempted to provide the Matlab script that employed to define the spiral tool-path for the truncated pyramid. Figure 7 depicts the isometric view of the truncated pyramid.

```
clear
clc
dh=0.8;    %step depth used
a=45;      %angle of inclination of the pyramid
h=30;      %Depth of the pyramid
L=100; W=100;
```



```

X=L/2; Y=W/2;
R1=sqrt(X^2+Y^2); %diagonal length
N=h/dh; %Number of loops or contour
m=1;

for n=0:90:360*N %dividing one contour into 360
    angles
    z(m)=-(dh/360)*n;
    R=R1-((dh/360)*n)/tand(a); %diagonal at any
    intermediate depth
    y(m)=R*sind(n+45);
    x(m)=R*cosd(n+45);
    m=m+1;
end
plot3(x,y,z,'b') % 3D visualization of helix

```

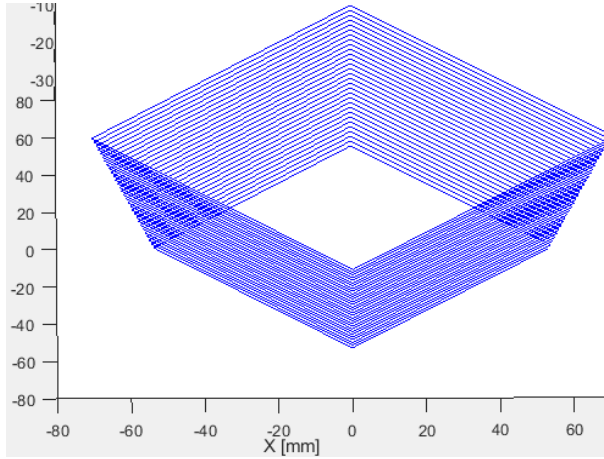


Figure 7: Isometric view of the truncated pyramid

### **Numerical Simulation**

The simulation of SPIF was conducted in ABAQUS to test the coordinate points created in Matlab. In the simulation, the displacement was defined by introducing the X, Y and Z coordinate points in the amplitude vs time data.

In the model, the sheet was fixed along its four peripheries. It defined as a deformable body and meshed with shell elements. The tool was defined as a rigid body. Figure 8 shows the deformed truncated cone, truncated pyramid, and hyperbola.

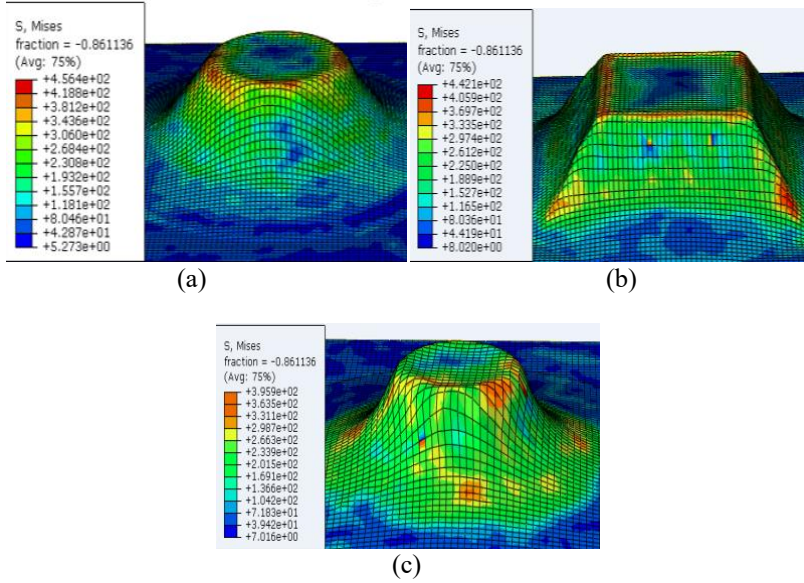


Figure 8: Numerical simulation of the; a) truncated cone, b) truncated pyramid and c) hyperbola

## Results and discussions

### Mixed String Generation

Table 1 provides a sample piece of coordinate points exported from Matlab by using the write table function and the mixed string created for a truncated cone. The mixed string is created by joining cell one to cell six by the “and” function. The mixed string data in Table 1 were input to create the G-code. By using the same procedure, mixed strings were created for the hyperbola and pyramid parts.

Table 1: Sample coordinate points exported from Matlab and mixed string

Part	Coordinate and Coordinate Points						Mixed String
Cone	X	35	Y	0	Z	0	X35Y0Z0
	X	34.99	Y	0.61	Z	-0.002	X34.992Y0.611Z-0.002
	X	34.97	Y	1.22	Z	-0.004	X34.974Y1.221Z-0.004
	X	34.94	Y	1.83	Z	-0.007	X34.945Y1.831Z-0.007

### G-code Generation

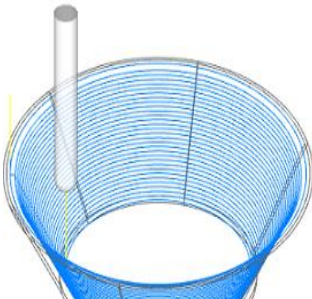
To change the mixed string into G-code, we must introduce it to the elements of the NC program. Preparatory and miscellaneous functions, coordinate values, feed rate, and spindle speed are the major elements of the NC program [10]. To accomplish this, a sample G-code was created from a truncated cone in Mastercam software (Table 2). The contour tool-path was used to define the tool-path. The preparatory and miscellaneous functions from the cone then introduced to the mixed string.

To generate the G-code, preparatory and miscellaneous functions from the sample G-code created from the truncated cone in Mastercam software were introduced at the start and end of the mixed string. Inserting block numbers, setting start and endpoints of the tool, define feed rate has done in SIMCO edit software. After that, the coordinate points have converted into G-code. The tool-path simulation of the G-code created from the Matlab script has shown in Table 3. Introducing the G-code to the CNC mill is required to form the sample parts.

## Conclusions

The aim of the current study was to create three-dimensional spiral tool path and convert it into G-code for the study of SPIF. This study set out to find a method for converting coordinate points created from Matlab script into G-code. This study makes a major contribution to show that coordinate points from the Matlab script can be converted into G-code. Prior to this study, it was difficult to convert coordinate points into G-code for the experimental investigation of SPIF. It is unfortunate that the study did not include the actual results of the experimental investigation gained after introducing the CNC mill. It would be interesting to compare this method and other methods used to create spiral tool path definition methods for the experimental investigation of SPIF.

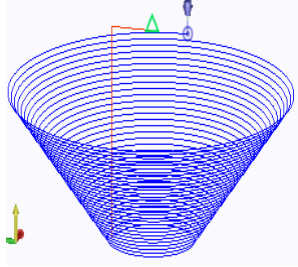
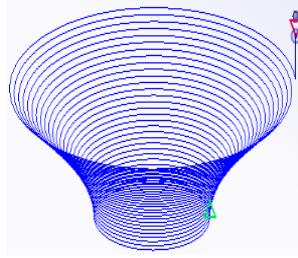
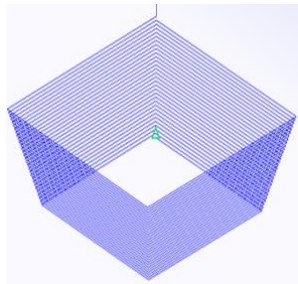
Table 2: Sample G-code for the truncated cone created in Mastercam

Position	G-code	Tool path simulation
Start	% N100 G21 N106 G0 G90 G54 X- N108 G43 H1 Z24.8 N112 G1 Z-.2 F1000.	
Intermediate	N114 X-33.113 Y-35.79 ----- -----	
End	N1258 M5 N1260 G91 G28 Z0.	

N1262 G28 X0. Y0.  
N1264 M30  
%

In the sample G-code, the preparatory and miscellaneous functions have found at the start and the end of the NC file. Whereas, the alphanumeric mixed string has found between the start and ends part of the NC file.

Table 3: Sample G-code and tool path simulation based on the proposed method

Part	G-Code	G-code Simulation
Truncated Cone	% N110 G21 N112 G0 G17 G40 G49 G80 G90 N114 T493 M6 N116 G0 G90 G54 X35 Y0 A0. S0 N120 G1 X35 Y0 Z0.1 F1000. N122 X35Y0Z0 N124 X34.992Y0.611Z-0.002 N126 X34.974Y1.221Z-0.004 N128 X34.945Y1.831Z-0.007	
Hyperbola	% N102 G21 N104 G0 G17 G40 G49 G80 G90 N106 T493 M6 N108 G0 G90 G54 X50.000 Y0 A0. S0 N110 G1 X50.000 Y0 Z0 F1000. N112 X49.988Y0.873Z-0.003 N114 X49.961Y1.745Z-0.006 N116 X49.918Y2.616Z-0.008 N118 X49.861Y3.487Z-0.011	
Truncated Pyramid	% N110 G21 N112 G0 G17 G40 G49 G80 G90 N114 T493 M6 N116 G0 G90 G54 X70.711 Y0 A0. S0 N118 G1 X70.711 Y0 Z0.000 F1000. N120 X70.711Y0.000Z0.000 N122 X0.000Y70.566Z-0.250 N124 X-70.422Y0.000Z-0.500 N126 X0.000Y-70.278Z-0.750	

**Nomenclature**

R <sub>i</sub> :	Maximum Radius	$\Delta R$	Radius change in a loop
R <sub>r</sub> :	Minimum Radius	$\beta$	Change in angle on the arc
R:	Radius at any depth	$\Delta X$ :	Change in the X
$\Delta Z$ :	Step depth	R <sub>n</sub>	Arc radius at any depth
d:	Depth of the part	D <sub>max</sub>	Initial diagonal length
N	Number of loops	D	Diagonal length at any depth
$\alpha$ :	Forming angle	W <sub>max</sub>	Top width
X,Y,Z	Coordinate Points	W <sub>min</sub>	Bottom width
$\theta$	Sweep angle	L <sub>max</sub>	Initial length
$\Delta r$	Change in radius		

**References**

- [1] M. B. Silva, M. Skjoedt, P. Vilaça, N. Bay, and P. A. F. Martins, "Single point incremental forming of tailored blanks produced by friction stir welding," *J. Mater. Process. Technol.* 209 (2), 811–820 (2009).
- [2] J. Jeswiet, "Metal forming progress since 2000," *CIRP J. Manuf. Sci. Technol.* 1 (1), 2–17 (2008).
- [3] J. Jeswiet, F. Micari, G. Hirt, A. Bramley, J. Duflou, and J. Allwood, "Asymmetric Single Point Incremental Forming of Sheet Metal," *CIRP Ann. - Manuf. Technol.* 54 (2), 88–114 (2005).
- [4] Z. Yeshiwas, A. Krishnaiah, "Extraction of Coordinate Points for the Numerical Simulation of Single Point Incremental Forming Using Microsoft Excel," *International Conference on Emerging Trends in Engineering (ICETE). Learning and Analytics in Intelligent Systems 2*, 577–586 (2020).
- [5] K. Suresh, A. Khan, and S. P. Regalla, "Tool path definition for numerical simulation of single point incremental forming," *Procedia Eng.* 64, 536–545 (2013).
- [6] M. Azaouzi and N. Lebaal, "Simulation Modelling Practice and Theory Tool path optimization for single point incremental sheet forming using response surface method," *Simul. Model. Pract. Theory* 24, 49–58 (2012).
- [7] R. Duflou, A. M. Habraken, J. Cao, R. Malhotra, M. Bambach, D. Adams, H. Vanhove, A. Mohammadi, J. Jeswiet, "Single point incremental forming: state-of-the-art and prospects," *International Journal of Material Forming* 11, 743-772 (2017).

- [8] M. Ur, R. Siddiqi, J. R. Corney, and G. Sivaswamy, “Design and validation of a fixture for positive incremental sheet forming,” Part B: Journal of Engineering Manufacture 232 (4), 629–643 (2018).
- [9] R. Malhotra, N. V. Reddy, and J. Cao, “Automatic 3D Spiral Toolpath Generation for Single Point Incremental Forming,” J. Manuf. Sci. Eng. 132 (6), 061003 (2010).
- [10] R. D. G. Corp and R. D. G. Corp, NC code reference manual (Roland DG Corporation, 2009), pp 6-7.

# Reduction of Copper to Steel Weld Ductility for Parts in Metallurgical Equipment

*Mohammad E. Matarneh\*, Nabeel S. Gharaibeh,  
Al-Balqa Applied University,  
Al-Huson University College Department of Mechanical Engineering,  
Al-Huson-Irbid, Jordan. P.O. Box 50, Irbid, Jordan  
\*bayan20042002@yahoo.com, nabeelgharaibeh@yahoo.com*

*Valeriy V. Chigarev  
Department of Metallurgy and Welding Technology,  
Pryazovskyi State Technical University, vul. Universytets'ka 7,  
Mariupol 87500, Ukraine.  
chigarew07@gmail.com*

*Havrysh Pavlo Anatoliiovych,  
Department of Carrying and Lifting Machines,  
Donbass State Engineering Academy, Donetsk region.,  
Kramators, str. Akademichna, 72, 84313, Ukraine.  
nauka.breda@gmail.com*

## ABSTRACT

*Despite being challenging, the welding of the dissimilar metals copper and steel is an essential process that is required for improving quality of equipment manufacturing in the fields of metallurgy, machine construction, and chemical industry. Restricted solubility of iron in copper leads to the formation of a supersaturated solid solution of iron and other chemical elements in the weld pool. Investigations have found the possibility of enhancing the process of welding copper with steel. In the case of using a flux-cored welding wire and an improved welding technique, the number of dendritic inclusions is reduced, and the weld ductility is improved. Studying the microstructure of a copper to steel weld confirmed the ability to enhance the outcome of the welding process of the dissimilar metals. The implementation of recommended preparation techniques of parts before welding, and optimization of the welding technique will increase the strength*

*of the welds and, increases the operational reliability of metallurgical equipment.*

**Keywords:** *Copper to Steel Welding; Flux-cored Wire; Microstructure; Fusion Line; Alloy Formation*

## Introduction

In order to yield high-quality weld assemblies, the method of which dissimilar metal joints are produced, and the resulting properties, plays a very important role. Maintaining such welding process under control makes it possible to produce dissimilar metal welded joints with the required indices of physic, chemical and technical properties. Such weld assemblies including dissimilar metal joints are used in metallurgy, machine construction, and chemical industry equipment manufacturing.

Process regulation is associated with a need to predict the resulting changes brought by the welding technique [1], [2]. The quality of a copper to steel weld has a great effect on the durability of a produced assembly when used under operational conditions that can cause cyclic load and thermal fatigue. This situation can be found in metallurgical equipment, for example, furnace Tuyeres and Crystallizers [1]-[3].

Both copper and iron have a face-centered cubic lattice construction, with a relatively similar crystal lattice; for copper:  $a = 0.3615 \text{ nm}$ ,  $N = 4$ , and for iron:  $a = 0.3656 \text{ nm}$ ;  $N = 4$  (in temperatures between  $910$  to  $1392^\circ\text{C}$ ), parameters [4]. Still some difference between them are found: a difference in melting temperatures; for copper:  $1083^\circ\text{C}$  ( $1356.2 \text{ K}$ ), while for iron:  $1535^\circ\text{C}$  ( $1808 \text{ K}$ ), a difference in their heat conductivity coefficient: for M1 copper ( $20^\circ\text{C}$ ) it is  $390 \text{ Wt/(m}\cdot\text{K)}$ , while for St.3 steel it is  $67 \text{ Wt/(m}\cdot\text{K)}$ , and in the value of their elastic modulus: for copper  $90 \times 10^3 \text{ MPa}$ , while for iron  $201 \times 10^3 \text{ MPa}$ . When welding copper and steel (where the main interaction is between copper and iron), differences in their melting temperature, density, thermo-physical properties (melting temperatures, heat conductivity coefficient, and the elastic modulus) affect the joining process [2], [4].

Improvements in the welding techniques of copper and steel that will yield a joint with better properties are important. The technical parameters of a welding process can be optimized by the analysis the welded metal joint properties [4]. A copper to steel weld usually fails due to cracks and damage, both along the fusion area and within the heat-affected zone from the copper side [5]-[7].

Many welding techniques have been investigated to overcome the challenge of copper to steel welding. Kuryntsev et al. [6] explored the usage of laser welding due to the high energy density provided by this technique. Guo et al. [7] investigated the usage of electron beam welding (EBW) with



great results. Brazing is also considered for copper to steel joints [8]. However, the aforementioned techniques are faced with some complications such as the ability of copper to reflect laser when laser welding, the need for a special setup for the process (welding in vacuum) in EBW, and the resulting weak mechanical properties of the work piece in brazing. All are limiting factor for real-life, in site application. Arc welding is considered as the most practical technique for on-site applications because of its low cost, convenience, and flexibility [9]

One of the factors resulting in reduction of copper to steel weld ductility is an increased amount of iron dendritic inclusions within the area of alloy formation in copper side [11]-[14]. The heterogeneity of the copper to steel weld and a decrease in the ductility index, i.e. an increase in the ultimate strength and an increase in the hardness of the heat-affected zone, result in the decrease in fatigue failure along the fusion zone during cyclic loading, mainly under a symmetrical loading cycle for the structure [13]. Controlling dendritic inclusions of iron into copper lead to improved durability of the weld, and reduced fatigue failure during cyclic loading.

Analysis of the weld ductility reduction factor and analysis of the weld structure and adjustment of welding technology are essential for improving copper to steel weld quality. Therefore, the impact of increased iron content in welding materials and the volume of molten steel on the penetration depth of iron dendritic inclusions into copper is studied.

## **Materials and Methods**

In the work presented here, both M1 copper GOST 1173-2006 (Table 1) was welded to St.3 sp.5 steel GOST 380-94 (Table 2). These comprise parts used in a metallurgical crystallizer.

For the welding process, the electrode used in shielded metal arc welding was Komsomolets-100 type (14-644-75 standard, GOST 9466-75). The welding was performed in the lower position at a reversed polarity direct current. Electrode diameter used was 4 mm, and the welding current ranged between 130-150 A, while the used filler wire was MNZhKT 5-1-0.2-0.2 in argon-arc welding of M1 copper to 09G2S steel.

Thickness of samples was 6 mm, welding current ranged between 380 and 400 A, tension was between 12 and 16 V, and argon consumption was between 80 to 90 l/h. The composition of 09G2S steel is shown in the Table 3. Additional details can be found in [15] and [16]. Finally, the flux-cored wire that was used in welding had diameters of 3.0 and 5.0 mm.

Table 1: Content of the used M1 copper, %

Additives	0.1003
Cu	99.9
Bi	0.001
Sb	0.002
As	0.002
Fe	0.005
Ni	0.002
Pb	0.005
Sn	0.002
S	0.005
O	0.05
Zn	0.005
P	0.04
Ag	0.003

Table 2: Content of the used St.3 sp.5 steel, %

Element	Content
C	0.14 to 0.22
Mn	0.80 to 0.11
Si	0.12 to 0.30
P	< 0.04
S	< 0.05
Cr	< 0.30
Ni	< 0.30
Cu	< 0.30

Table 3: Chemical composition of 09G2S steel, %

Element	Content
C	$\leq 0.12$
Si	0.5 to 0.8
Mn	1.3 to 1.7
Ni	$\leq 0.3$
S	$\leq 0.04$
P	$\leq 0.035$
Cr	$\leq 0.3$
N	$\leq 0.008$
Cu	$\leq 0.3$
As	$\leq 0.08$
Fe	96 to 97

Table 4 lists the components of the flux-cored wire PP-A-Z-F-M. An improved PDG-516M feeder with a power supply was used during welding. Rated welding current was 500A at a duty ratio of 60%. Arc voltage adjustment was between 18 to 50 V, and the welding current adjustment was 60 to 500 A.

Table 4: Components of flux-cored wire PP-A-Z-F-M, % [15]

Element	Content
Aluminium	54.1 to 60.1
Zirconium	0.8 to 0.9
Ferrotitanium	1.2 to 1.8
Copper powder	6.1 to 9.2
Hematite	3.1 to 5.0
Graphite	2.0 to 4.0
Chromium	7.0 to 9.0
Yttrium oxide	4.0 to 5.4
Fluorite	2.0 to 6.2
Sodium fluorosilicate	2.9 to 4.1
Ferromanganese	1.4 to 2.8
Ferrosilicon	1.9 to 3.4

The microstructure of a M1 copper and 09G2S steel weld joint will be studied under different welding techniques to identify the depth of dendritic inclusions penetration. In addition, a variety of electrode sizes will be tested.

## Results and Discussions

The impact of iron content in welding materials on depth of dendritic inclusions within the heat-affected zone from copper side was studied. Figure 1 shows a picture of a weld between copper and steel in used in parts of a metallurgical crystallizer. As mentioned before, the welded metal was 6 mm thick.

Studying the microstructure found in the weld, it was found that an  $\alpha$ -phase with a cubic lattice appeared within the fusion line. This phase is a supersaturated solid solution of iron in copper, where the composition of the  $\alpha$ -phase is not constant. There indications of elements included in the composition of electrode metal, such as nickel, manganese and others [13].

To investigate the depth of dendritic inclusions resulting from crystals growing as the molten metal solidifies, the microstructure of the fusion line in a welded joint was studied. Figure 2 shows the microstructure of a welded joint between M1 copper and 09G2S steel.

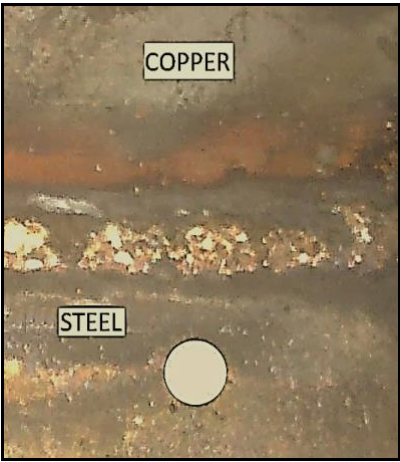


Figure 1: A weld between copper and steel used in parts of a metallurgical crystallizer

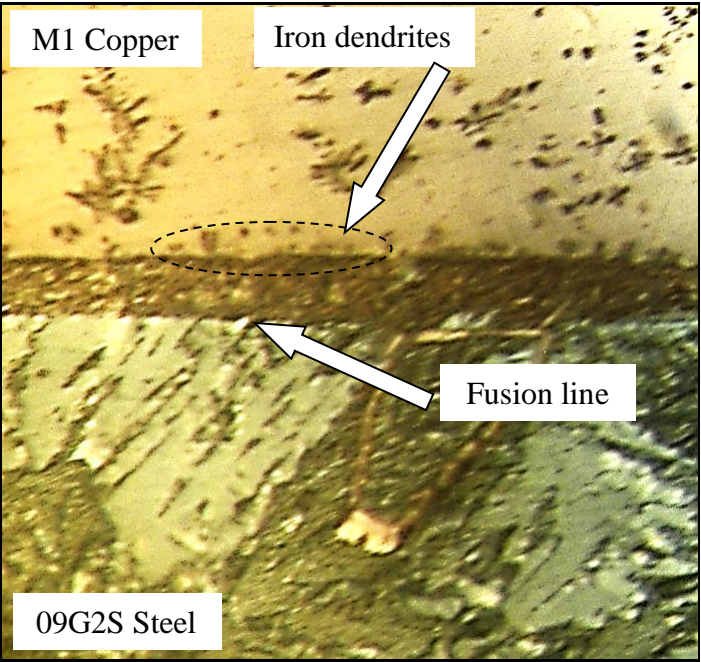


Figure 2: Welded joint microstructure,  $\times 800$  times

As it can be seen in Figure 2, iron dendrites were found next to the fusion line within the copper side (the upper side in the figure). The depth of

iron dendritic inclusions penetration during shielded metal arc welding was found to be between ranging between 0.5 and 1.8 mm. The formed structures will more likely affect the properties of the equipment they are used in. Such alterations are brought by the presence of dendritic growth.

In order to examine if the application of a different approach in welding of the depth of dendritic infusion, the microstructure of a weld produced by argon-arc welding and flux-cored wire was examined. Figure 3 shows the microstructure resulting in the weld after applying the aforementioned argon-arc welding and flux-cored wire to join the two metals.

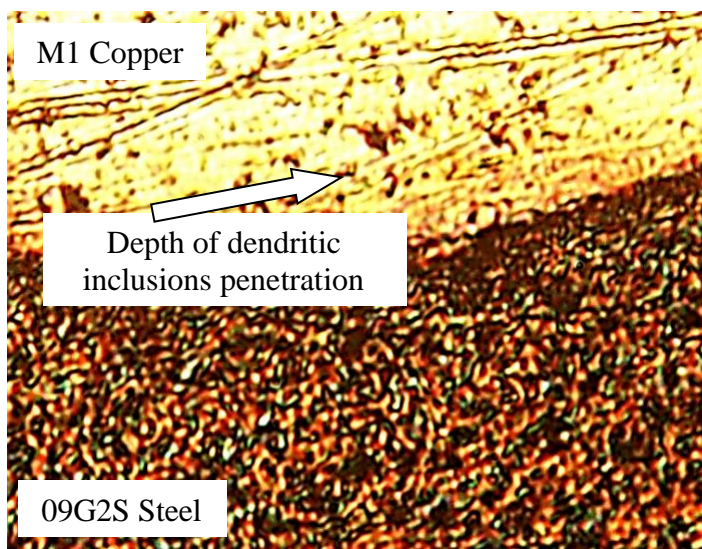


Figure 3: Microstructure of the weld after argon-arc welding,  $\times 900$  times.

As shown, it was found that during argon-arc welding and flux-cored wire welding the depth of iron dendritic inclusions penetration was found to be between 0.6 and 1.2 mm. The resulting depth compared with the depth of penetration found during the shielded metal arc welding was found to be slightly less. This indicates a slight enhancement in controlling the formation of undesired crystal structures in the final body of the weld.

Another alternative that can be employed in the welding process in order to reduce the effect of dendritic inclusions in the weld joint, is increasing the amount of welding materials used, which can be achieved by the usage of welding electrodes with larger diameters. Figure 4 shows the change in resulting depth of dendritic inclusions resulting in weld of the two metals using different electrode diameters.

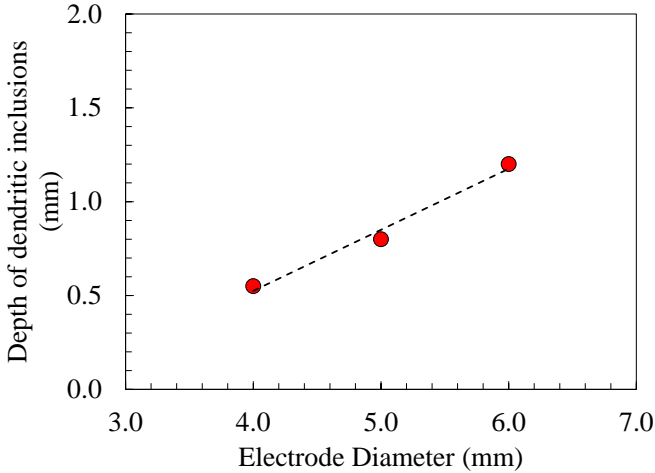


Figure 4: Dependence of the depth of dendritic inclusions on the iron content in welding materials and the diameter of the electrode

As seen in Figure 4, using an electrode with a larger diameter (i.e. increasing the welding material in the electrode) resulted in an insignificant increase in the depth of penetration. It should be noted that the resulting insignificant changes in depth of penetration, will not reduce the fatigue strength under testing for cyclic loading.

The amount of molten metal (steel) most seriously affects the amount of dendritic inclusions. The greater the extent of steel melting during the weld process, the larger the resulting weld pool. This will generate a greater specific heat input during welding, which will lead to iron crystallization not only within the weld, but also on individual grains of metal due to the limited solubility of iron in copper [17]. This occurrence can be the result of procedural violations for welding preparation. Figure 5 shows the microstructure of the weld, the fusion line, and the heat-affected zone with rejection of iron as solid solution dendrites, with increased iron melting.

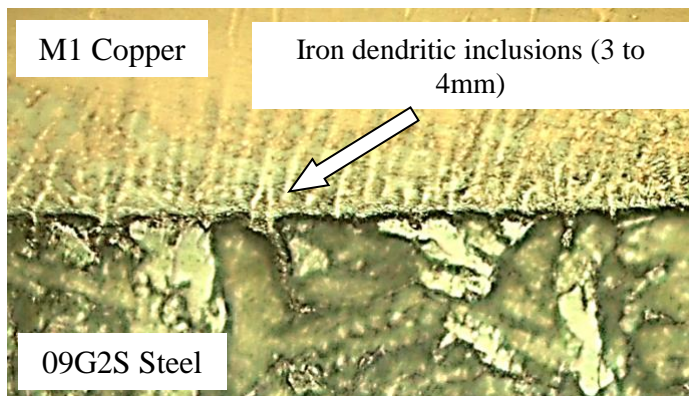


Figure 5: Microstructure of a welded joint with increased degree of iron melting

As it can be observed in Figure 5, the presence of excessive iron is kept in the  $\alpha$ -phase as supersaturated solid solution. Such amount of iron increases the hardness of the heat-affected zone, which in its turn will reduce the ductility of the resulting weld. Resulting in a weld joint that is vulnerable to fatigue under stress. Excess iron melting could have additional consequences in the presence of other chemical elements. Figure 6 shows the welded joint microstructure in case of excess iron melting.



Figure 6: Welded joint microstructure in case of excess iron melting,  $\times 800$  times.

As clearly shown in Figure 6, the dendritic inclusions on the edges of the grains are in a ball-shaped form. This is where chemical elements (manganese, nickel, titanium, copper, etc.) are transferred after the diffusion. The presence of chemical elements can be attributed to failure to comply with the requirements of edge preparation before welding.

It can be deduced that excess iron melting, which occurs due some procedural violations during welding and failure to comply with the requirements of edge preparation, are the key factor of reduced weld ductility and fatigue strength of copper to iron welds.

Overall, by using an improved copper to steel welding technique and the developed flux-cored wire (controlling the weld phase composition), the number of dendritic inclusions can be reduced at the weld line. This will result in increasing the weld ductility and the durability of the weld assemblies [13], [15]-[19].

## Conclusions

1. Iron content in the weld material for welding copper and steel is not the key factor that reduces the life of welded joints due to fatigue.
2. Restricted solubility of iron in copper leads to the formation of an  $\alpha$ -phase as supersaturated solid solution of iron and other chemical elements in the weld pool.
3. If the recommendations for parts preparation before welding were followed, the fatigue strength of welded joints will not be reduced, and the operational reliability of metallurgical equipment assemblies can be improved.
4. By optimizing the composition of welding materials and the welding technique, the amount of molten iron and the degree of melting of iron in the weld pool can be reduced.

## References

- [1] V.V. Chigarev, I.V. Serov, P.A. Gavrish, M.A. Turchanin, and V.D. Kassov, "Investigation of Interaction between Weld Pool Components When Welding Parts of Metallurgical Equipment," Protection of metallurgical machine from breaks: Collection of Scientific Works 8 (Mariupol), 214-223 (2005).
- [2] P.A. Gavrish, "Prevention of Formation of Crystallization Cracks When Welding Copper with Steel", The 10th International Scientific Conference New constructional steel and alloys and methods of their processing for increasing reliability and durability of products, Zaporizhia National Technical University, Zaporizhia, 77-79 (2005).



- [3] P.A. Gavrish, "Improvement of Technology of Welding Copper with Steel Considering Structures or Formation of a Heat-Affected Zone," Bulletin of Khmelnytskyi National University 3 (2), 11-13 (2007).
- [4] V.R. Riabov, D.M. Rabkin, R.S. Kurochko, and L.G. Strizhevskaya, "Welding Dissimilar Metals and Alloys," (Moscow: Mashinostroenie), 239 (1984).
- [5] V.V. Chigarev, P.A. Gavrish, and L.V. Vasilieva, "Optimisation of the Technological Parameters of Steel to Copper Welding Process", Eastern-European Journal of Advanced Technologies 1 (49), 20-24 (2011).
- [6] S. V. Kuryntsev, A. E. Morushkin, and A. Kh Gilmudinov, "Fiber laser welding of austenitic steel and commercially pure copper butt joint," Optics and Lasers in Engineering, (90), 101-109, 2017.
- [7] Guo, Shun, Qi Zhou, Jian Kong, Yong Peng, Yan Xiang, TianYuan Luo, KeHong Wang, and Jun Zhu, "Effect of beam offset on the characteristics of copper/304stainless steel electron beam welding," Vacuum 128, 205-212 (2016).
- [8] R. K. Choudhary, Laik, A., & Mishra, P, "Microstructure evolution during stainless steel-copper vacuum brazing with a Ag/Cu/Pd filler alloy: effect of nickel plating," Journal of Materials Engineering and Performance 26 (3), 1085-1100 (2017).
- [9] Cheng, Zhi, Jihua Huang, Zheng Ye, Yu Chen, Jian Yang, and Shuhai Chen, "Microstructures and mechanical properties of copper-stainless steel butt-welded joints by MIG-TIG double-sided arc welding," Journal of Materials Processing Technology (265), 87-98 (2019).
- [10] P.A. Gavrish, "Investigation of Steel to Copper Fusion Line during Welding," Naukovi Visti Dalivskogo Universitetu, Luhansk 1 (49), (2011).
- [11] M.A. Turchanin, P.G. Agraval, and I.V. Nikolaenko, "Thermodynamics of alloys and phase equilibria in the copper-iron system," Journal of Phase Equilibria. Basic and Applied Research 4 (24), 307-319.
- [12] P.A. Gavrish and M.A. Turchanin, "Thermodynamics of Copper-Iron Interaction in a Weld Pool", Bulletin of Donbas State Machine-Building Academy 2 (4), 75-78 (2006).
- [13] P.A. Gavrish, "Improvement of Technology of Copper to Steel Welding: monograph", Kramatorsk, (Donbas State Machine-Building Academy), 188 (2014).
- [14] Naukova Dumka, "Durability of Welded Joints Under Changing Load," in Academy of Sciences of Ukraine. Paton Institute of Electric Welding, V.I. Trufiakov Ed., (Kiev), 256 (1990).
- [15] V.M. Karpenko, A.V. Granovskiy, N.A. Makarenko, and P.A. Gavrish. Author's certificate 1538395, MKI V23K 35/368. Flux-cored wire, (USSR). NO 4418894/31-27, Claimed on 03.05.88, Declassifying order DSP NO 06-154 of 04.11, 2010.

- [16] V.M. Karpenko, A.V. Granovskiy, N.A. Makarenko, P.A. Gavrish, Author's certificate 1540173, MKI V23K 35/368. Flux-cored wire, (USSR), NO 4442783/31-27, Claimed on 20.06.88; Declassifying order DSP NO 06-154 of 04.11, 2010.
- [17] P. Gavrish, "The Preliminary Heating at Welding Copper and Steel," American Journal of Materials Engineering and Technology 3 (1), 46-48 (2013).
- [18] V.V. Chigarev, P.A. Gavrish, and E.P. Gribkov, "Improving the technological conditions of drawing flux-cored welding wires," Welding international 1 (27), 59-61 (2014).
- [19] V.V. Chigarev, P.A. Gavrish, and E.P. Gribkov, "Investigation of the process of drawing flux-cored wire for welding cooper to steel," Welding international 9 (26), (2012).

# ANFIS Model for Prediction of Performance-Emission Paradigm of a DICl Engine Fueled with the Blends of Fish Oil Methyl Ester, n-Pentanol and Diesel

Kiran Kumar Billal\*, G.R.K. Sastry<sup>2</sup>, Madhujit Debi

<sup>1</sup>National Institute of Technology, Agartala

<sup>2</sup>National Institute of Technology, Andhra Pradesh

\*[billa2962@gmail.com](mailto:billa2962@gmail.com)

## ABSTRACT

*A precise, robust model for complex systems like IC Engines would be much beneficial because of environmental issues, fossil fuel depletion and accumulation of on-road vehicles. The present study depicts the compatibility of higher alcohols like n-pentanol that are produced in renewable ways as a promising blending additive with biodiesel fuels. Biodiesel prepared from the waste parts of the fishes is used to blend with petrodiesel. The methyl esters of fishoil biodiesel (MEFO) and n-pentanol are blended with petrodiesel at different proportions are tested on a four-stroke single cylinder DICl engine and results from witnesses the noble benefits of adding higher alcohols that are observed in both performance and as well as in emissions. The experimental paradigm is further fed to an artificial intelligent model to test the inherent predicting capability an Artificial Intelligent Adaptive Neuro-fuzzy Interface System (ANFIS). A sugeno network with brake power and percentage of biodiesel as input parameters and engine response paradigm such as BSFC, BTE, HC, CO and NOx as outputs are modelled and tested on a statistical platform. It was found that the proposed model is robust and efficient system identification tool to map the input-output response paradigm with high accuracy as the regression (R) values are ranging from 0.9967 to 0.9999, RMSE is ranging 0.000026 to 0.0000336 and MAPE is very low ranging from 0.0021 to 0.0028.*

**Keywords:** Performance; Emission; ANFIS; Fishoil Biodiesel

## **Introduction**

Most significant single wellspring of vitality devoured by the total populace is petroleum, surpassing coal etc. [1]. Oil is an essential part of the creation of composts, plastics and synthetic concoctions. Most specialists expect overall oil excavation will top at some point somewhere in the range of 2007 and 2025, and demand will keep on rising another 40% amid a similar period [2]. The typical 52% ascent in world CO<sub>2</sub> discharges by 2030 and outflows of non-renewable energy sources (counting oil) officially identified with global environmental change [3]. The reliance on limited vitality sources constrained by perilously few, often politically insecure nations, has shockingly prompted a cycle of crisis [4].

Biodiesel, formally known as either methyl-ester or ethyl-ester, is usually happening animal fat or veggie oil which has been scientifically altered to keep running in a compression ignition engine. Biodiesel's leverage contrasted with petrodiesel like its sustainable nature, better discharge, support for household horticulture and compatibility with current running engines without any modifications in engines. Overall biodiesel limit has developed to over 2.2 billion liters because commercial generation started in the early '90s [5]. The US instituted American Society for Testing and Materials (ASTM) D 6751 in the year 2001 which standardizes 14 fuel properties like heating value, cetane index etc. Later, the European Union (EU) in the course of time instituted the biodiesel standard EN 14214 in the year 2003, which antiquated discrete country standards [6].

Extensive research was going in the alternative fuels section from times in these fields and originated some alternatives for petrodiesel that can be used in existing engines without any engine modifications. Biodiesel can be disengaged from vegetable oils as well as animal fats and transesterified with methyl/ethyl alcohols to frame alkyl esters [7]. According to a recent survey, the fish processing industries are discarding the unwanted parts of fishes on a colossal scale consistently around the world. The Central Institute of Fisheries Technology (CIFT) expressed that over one lakh Mg of shrimps are created as fish waste parts annually. As per the International Fishmeal and Fish Oil Organization (IFFO), the world fish oil generation is 1.01 million tons and it will be expanded ten times in next five years [8].

Consequently, fish oil has developed global attention and concern for being a decent reserve of biodiesel for petrodiesel fuel by decreasing the natural poisons and guaranteeing energy security. A few analysts investigated the execution and emission qualities of fish oil biodiesel. The test outcomes demonstrated that the engines worked efficiently with overall efficiency and decrease in emission discharges [9]. CO and CO<sub>2</sub> emissions are considerably lowered with the blends of fish oil biodiesel [10]. Preto et al. [11] considered the engine performance, ignition and emission attributes of fish oil fuel in a

heavy-duty CI engine by differing the blends from 0% to 100% in the interim of 25% and half.

The test outcomes demonstrated that the engine worked typically guaranteeing its appropriateness as a beneficial fuel. Hence, the potential advantages of fish oil biodiesel are utilised in the study. Higher alcohols are less destructive on petrodiesel injection and conveyance courses of action because of their significantly less hygroscopic behaviour than ethanol getting consideration comprehensively. With its incredible miscibility with the petrodiesel, these higher alcohols are promising petrodiesel added chemical substances [12].

### **Higher Alcohols as a Biodiesel-Diesel Additive**

Alcohols can be regarded as a clean blending element to diesel-biodiesel blends because they are renewable in nature. Redefining the biodiesel with the assistance of higher alcohols like n-pentanol is a practical choice to upgrade biodiesel properties all together to enhance the execution in petrodiesel engine applications. Extensive research has been done with short chain alcohols or low alcohols such as ethanol and methanol as additive to the proposed alternative fuel in CI engine systems. Nonetheless, longer chain or higher alcohols like n-butanol [7], [13], [14], n-pentanol [15] are getting growing focus on being used as a CI engine fuel by many researchers.

However, n-pentanol with five long carbon chain shows better fuel properties than ethanol, methanol and butanol. Furthermore, with its low polarity and hydrophobic nature the problem of phase separation in blends can be avoided [16]. With its excellent miscibility with diesel and vegetable oils, n-pentanol is becoming the researcher's choice in recent times. n-pentanol can also be a great green solution developed from renewable root. However, the reduced cetane number of higher alcohols is a limitation and it is important to enhance the same that for effective combustion and lower emission. Cetane number, one of crucial characteristic for the fuels of CI engines that ensure knocking-free combustion in the charge.

Thus, additives with a high cetane number fundamentally help in enhancing the overall efficiency of the engine [17]. The additive which is normally an oxygenated chemical, may also possess an added advantage of reducing the emission of hydrocarbon, CO and smoke of a CI system. Dimethyl ether, diethyl ether are such chemical substances comes under this category and offer wide range of benefits. Raza et al. [18] concluded in their work that the addition of pentanol along with Di-Methyl ether gave them better exhaust emissions in terms of reducing PM and NO<sub>x</sub>. Pan et al. [19] reported that the soot reduced drastically with pentanol blends with 2-EHN.

The fish oil methyl esters come up with reasonable cetane index that the cetane improvers can be ignored. This builds the scope for the novelty that the blends of fish oil biodiesel, n-pentanol with diesel as an alternative fuel option for a direct injection compression ignition engine. The prediction

of the experimental paradigm by an artificial intelligent model like ANFIS adds significance to the originality.

The auto mobile manufacturers and application engineers have thought that it was hard to run the engine for all conceivable working states of burden and mix which is a tedious, complicated and costly task [20]. Mathematical models particularly artificial intelligent models help in reducing manual effort and improves quality [21]. Subrata et al. [22] compared Neural Network model with a ANFIS model and reported the superiority of ANFIS model. Singh et al. [23] announced that their RSM model is dynamic in enhancing the info parameters for a petrodiesel engine fuelled with biodiesel and petrodiesel mixes. With a low percentage error, the model is a proficient framework recognizable proof device and equipped for foreseeing the actual engine conduct with a praiseworthy exactness. Yusaf et al. [24] compared ANFIS with Support Vector Machine (SVM) and published that the ANFIS is advantageous over SVM.

To this degree, an express investigation fundamentally tending to the level of enhancing performance, emission trade-off view accomplished by offline alignment practices on existing Direct Injection CI engines under the skyline of existing outflow guidelines with higher alcohols like n-Pentanol is yet to be addressed. It very well may be closed from the thorough literature survey, just a bunch of works have been done, and the present examination shows a potential strategy dependent on demonstrating and streamlining that could analyze various blend structures for a Direct Injection CI engine and prescribe an appropriate blend exposure to no engine adjustments with sensible accuracy.

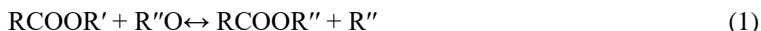
The present examination additionally conveys an ANFIS based prediction model using the engine responses of the DI engine with n-Pentanol percent, biodiesel percent, and load percent as inputs. The objective is to propose an appropriate fuel blend utilizing information factors, at the same time decreasing the engine responses like BTE, BSFC, NO<sub>x</sub> CO and UHC simultaneously has not been investigated yet. And thus an endeavor to investigate the emission performance paradigm of a single cylinder four stroke direct injection diesel engine, DICl naturally aspirated engine fuelled with different blends of diesel-biodiesel-additive blends is arranged to load this void.

## **Materials and methods**

### **Preparation of Test Fuels**

The transformation process of waste fish oil into fish oil methyl ester is done through a specific process called transesterification. The raw fish oil is heated to 50-60°C and maintained steady state conditions. The basic catalyst KOH is added to the preheated raw oil and whole mixed up. Preheating avoids

forming soap and thus allows to form pure methyl esters. The mixture is heated up to 70–80 °C during which the viscosity reduces drastically. The content which was allowed to settle overnight had a thick layer of glycerol at bottom separated by a mush of biodiesel, catalyst and some calculated measure of alcohol. To get the pure methyl ester, water wash with aqueous phosphoric acid (4% volume /volume%) is carried out. The content then was dried at 80 °C and observed for chemical stability before analysis. The transesterification process is depicted in the equation 1.



The methyl esters of fish oil, MEFO thus obtained is clear slightly orange yellow liquid with an intense smell. The methyl esters of fish oil, MEFO is kept under observation for 72 hours to check the phase separation issues before it is used to blend. The transesterification reaction [11], [25] is shown below. The test fuels were prepared with the diesel additive diethyl ether of analysis quality anhydrous DEE with 99.5% purity [15], n-pentanol of 99.9 % purity [26] and base fuel diesel are blended together in volume ratio as follows.

- m20p5= MEFO 20 % + 5% n-pentanol + 75 % Petrodiesel
- m20p10 = MEFO 20 % + 10 % n-pentanol + 70 % Petrodiesel
- m30p5 = MEFO 30 % + 5% n-pentanol + 65 % Petrodiesel
- m30p10 = MEFO 30 % + 10% n-pentanol + 60 % Petrodiesel
- Diesel= Diesel 100 %

The properties of the pilot fuels is demonstrated in Table 1.

Table 1: Properties of test fuels

Pilot Fuel	MEFO	m20p5	m20p10	m30p5	m30p10	ASTM
Density @ 20 °C, g/cm <sup>3</sup>	0.885	0.832	0.831	0.839	0.852	D4052
Kinematic Viscosity @ 20 °C, mm <sup>2</sup> /s	3.6	2.75	2.81	2.93	2.95	D445
Cetane number	52.6	49.995	49.5	50.125	49.73	D613
Calorific value, MJ/kg	40.1	43.03	42.87	42.76	42.16	D240

Table 2: Properties of base fuels [16], [18], [27]

Base Fuel	MEFO	Diesel	n-pentanol
Density @ 20 °C, g/cm <sup>3</sup>	0.885	0.82	0.815
Kinematic Viscosity @ 20 °C, mm <sup>2</sup> /s	3.6	2.5	2.89
Cetane number	52.6	51.3	20
Calorific value, MJ/kg	40.1	44	34.65

The engine selected for conducting the experiment is a 3.5 kW, Kirloskar make TV1 naturally aspirated engine water cooled model in the National Institute of Technology, Agartala. The engine is loaded with different mountings like an eddy current type dynamometer for measuring load, a crank angle sensor for measuring speed, a piezoelectric type pressure sensor to sense the in-cylinder pressures and an AVL five gas emission device that are detailed. The engine schematic diagram and valve timing diagrams were shown in Figure 1 and Figure 2 respectively.

The inlet valve opening is at 4.5° before Top Dead Centre and the exhaust valve is closing 4.5° after Top Dead Centre creating a valve overlap of 9° to the engine. Figure 2 illustrates the schematic diagram for the engine testing. The test rig is connected to a graphical user interface using a software “ENGINE SOFT” software was employed for estimating the temperatures of exhaust gas, water inlet and outlet, engine aspiration, fuel consumption, brake power, brake specific fuel consumption, etc.

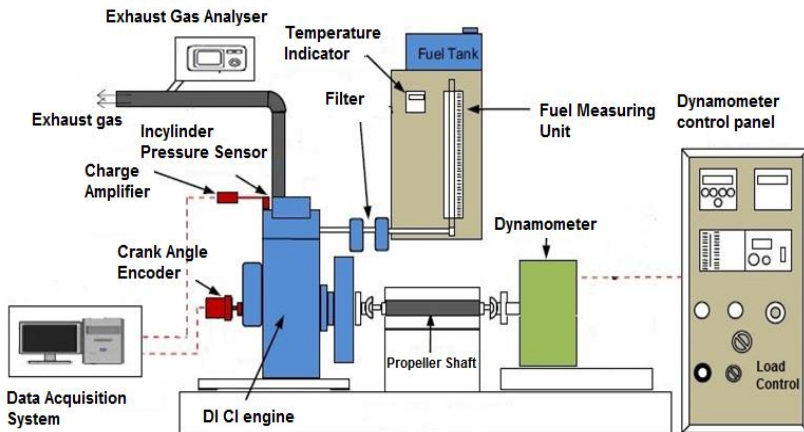


Figure 1: Schematic diagram of engine setup



An AVL 444 DI five gas analyzer is used to document the emission profiles. The test engine is fixed with the fuel injection at 27° before TDC. The technical details of the testrig are demonstrated in Table 3.

Table 3: Engine Specifications

Sl.	Engine Components	Specifications
1	Make	Kirloskar Oil Engine Ltd.
2	Model	TV1
3	No. of Cylinders	1
4	No. of Strokes	4
5	Bore Dia.	87.5 mm
6	Stroke Length	110 mm
7	Compression Ratio	17.5
8	Cylinder Volume	661 cc
9	Cooling System	Water Cooled
10	Fuel Oil	H. S. Diesel
11	Lubricating Oil	SAE 30/SAE 40
12	Fuel Injection	Direct Injection
13	Governing	Class "B1"
14	Start	Hand Start
15	Rated Output	3.6 kW
16	Rated Speed	1500 RPM
17	Overloading of Engine	10% of rated output
18	Lub. Oil Sump Capacity	3.7 Lt
19	Injection pressure	205 bar

## Results and discussions

### Performance analysis

#### BTE: Brake thermal efficiency

BTE is straight representation of the efficiency, which takes chemical energy present in the fuel converted into some form of work. It is also the ratio of engine brake power to the input of chemical fuel energy [28].

$$BTE = \frac{\text{Engine Brake Power}}{\text{Fuel consumed per second} \times \text{Calorific value}} \quad (2)$$

Figure 2 depicts the variation of the engine response concerning the brake power developed at different loads. All the pilot fuels are proved to be worthy with respect to the engine response. The test rig is fuelled with different pilot fuels prepared with the methyl esters of Fishoil MEFO and the

pentanol additive and a steady increase in thermal efficiency can be seen as the load increases. The m20p10 blend is giving maximum performance at all loads. The blend registered 6.28% more than petrodiesel at full loads. The reason for the rise in brake thermal efficiency is the oxygen portion in blend having pentanol and MEFO, which enhances the combustion.

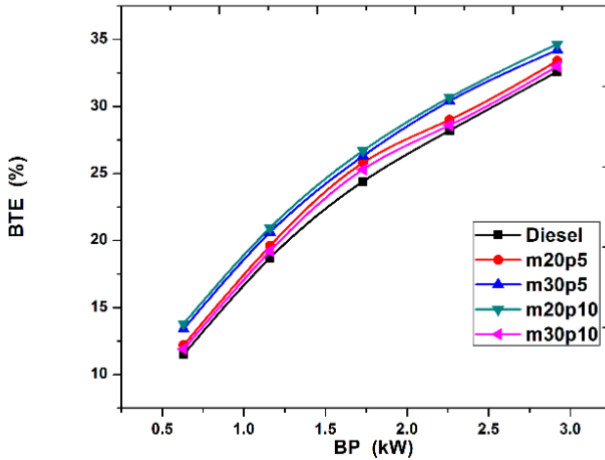


Figure 2: BTE versus BP

### BSFC: Brake Specific Fuel Consumption

The parameter signposts the quantity of fuel to be expended per unit power output [28].

$$BSFC = \frac{\text{Pilot fuel flow into the engine in kg/hr}}{BP} \quad (3)$$

Variation of the engine response concerning the brake power developed at different loads is shown in Figure 3. It can be perceived that it decreases gruffly with the increase in brake power for all blends. The primary foundation for the reduction in BSFC could be regarded to increment in brake power which is because of relatively less quantity of heat losses were recorded at higher loads. All the pilot blends and petrodiesel were confirmed decreasing with increasing brake power and hence load share. It is because of the higher part of the increase in brake power concerning load in comparison with the rise in fuel consumption. The effect of Fish oil methyl ester and n-pentanol on the engine responses depends on the association between the fuel properties like fuel oxidation time, kinematic viscosity of the sample, calorific values and proper fuel injection strategies. More amount of fuel enters into the cylinder due to higher density of the pilot fuels and increased

the fuel consumption. Lower heating values due to the addition of n-pentanol also increased the consumption. Figure 4 depicts that m20p10 recorded a 1.3 % higher consumption than other petrodiesel. The combined effects of density, cetane number, heating value and kinematic viscosity are the reason behind the higher BSFC [29].

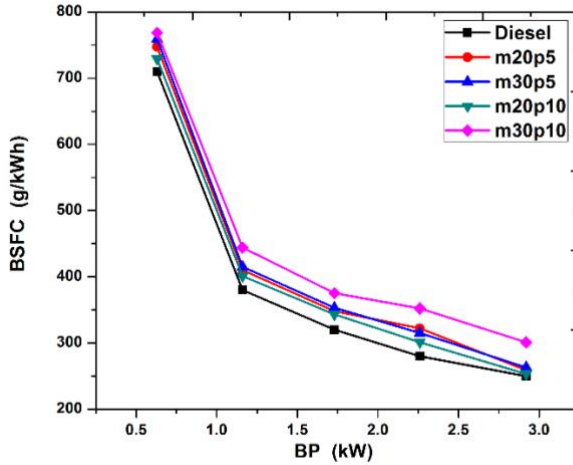


Figure 3: BSFC versus BP

#### NO<sub>x</sub>: Nitrogen emissions

NO<sub>x</sub> is one of the critical factors that are linked directly to environmental issues like global warming. In-cylinder temperature, oxygen quantity in fuel sample and, equivalence ratio are some crucial factors that influence the formation of NO<sub>x</sub>. Variation of the engine response concerning the brake power developed at different loads is shown in Figure 4. Around 5% reduction is seen with the m20p10 blend at full loads which was a significant achievement in the experiment. The main reason for this increase in NO<sub>x</sub> concerning its load conditions can be given by Zeldovich reaction mechanism [28] which says, by elevated combustion temperatures inside combustion chamber attributable to which the elements like oxygen and nitrogen dissociate within their natural atomic state, react chemically to form NO.

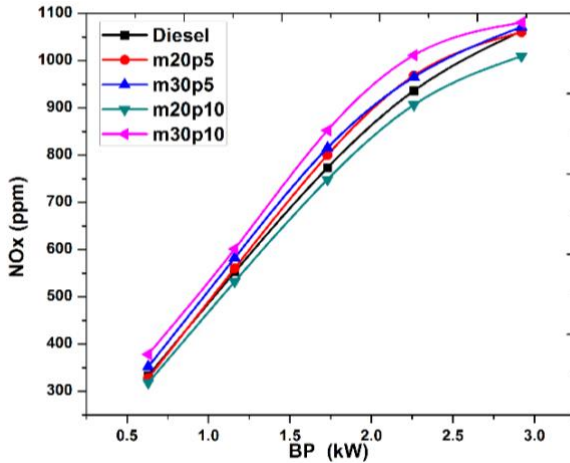


Figure 4: NOx versus BP

#### CO: Carbon monoxide

The variations of CO emission with respect to Brake Power for various fuel blends are shown in Figure 5. It can be understood from the graph that at low loading condition, the CO emission from the engine does not show any noticeable variations when compared to petrodiesel. An abrupt increase in the response is noticed in all fuel blends at higher loading conditions. The noble benefit of adding higher alcohol like n-pentanol can be seen. However, addition of n-pentanol in the pilot fuels decreased the CO emission significantly. Lower C/O ratio of n-pentanol benefited the fuel blend in producing lower CO as less carbon radicals participated in chemical combustion inside the cylinder. In addition to this, the decomposition of n-pentanol and higher oxygen in the also helped CO to oxidized to CO<sub>2</sub>. It was also observed that CO emission increased significantly with m30p10 blend having 10% pentanol. Adding pentanol with 10% pentanol was found to reduce CO emission significantly. It is a well-known fact that CO oxidizes to produce CO<sub>2</sub>.

In Figure 5, it is clear that the blend m30p10 is giving least CO emissions as it recorded 23% and m20p10 is producing 13.1% lesser CO emission than petrodiesel when compared.

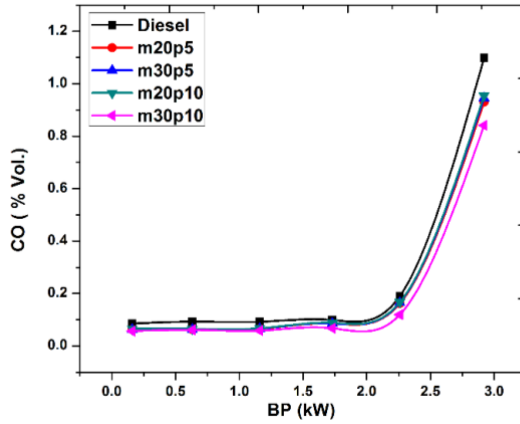


Figure 5: CO versus BP

### UHC: Unburnt hydrocarbons

Unburnt hydrocarbons are due to the absence of relatively limited oxygen present in the combustion chamber and excess quantity of fuel sample injected inside the combustion chamber at high loads. The production of unburnt hydrocarbons is a definite consequence of incomplete combustion and gets deposited on the walls of the combustion chamber. Variation of the engine response UHC concerning the brake power developed at different loads is portrayed in Figure 6 in which the addition of higher alcohols reduced the UHC production is depicted. The m30p10 is giving 25.2% lesser UHC and m20p20 is giving 17.3% lesser than petrodiesel.

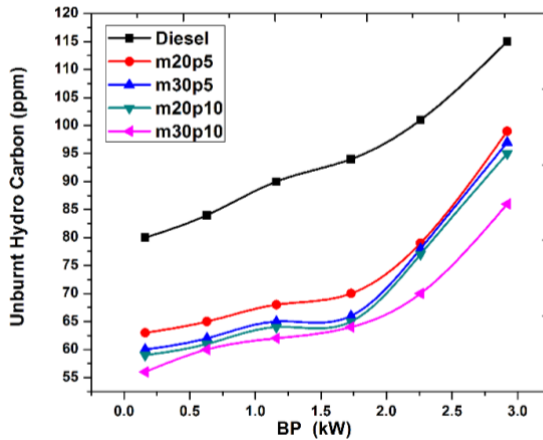


Figure 6: UHC versus BP

### Trade-off Study

Trade-off study is principally a relative appraisal among several parameters to discover the significance of a specified metric in the landscape of the other ones.

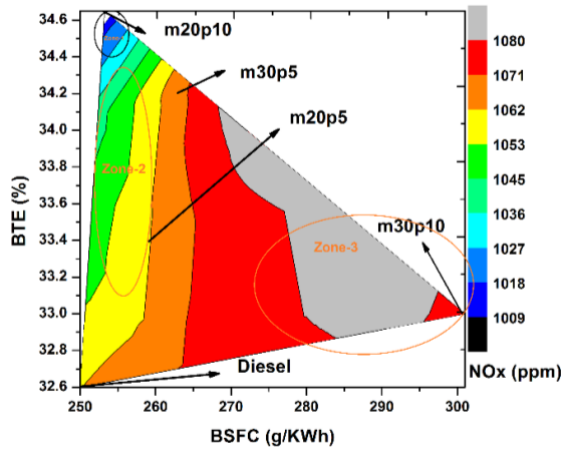


Figure 7: Trade-off among BTE, BSFC and NOx

The current trade-off analysis deals with an extensive investigation acknowledged on variations in NOx relating Brake Thermal Efficiency, and fuel consumption, and oxides of nitrogen, which has been shown in Figure 7. The tradeoff area is divided into three zones. In zone-1 the minimum NOx with bluish shades are considered, the greenish-yellow hues are considered as zone-2 representing medium NOx, and the reddish grey shades are regarded as higher NOx production in zone-3. For 20% MEFO blends with pentanol, the presence of pentanol in the pilot fuel considerably increased the BTE and reduced the BSFC and NOx simultaneously can be depicted in the trade-off area as m20p5 in zone-2 shifted to zone-1 for m20p10. The reason might be the optimum oxygen percentage in the pilot fuel, and the lower vapour pressure of the additive limited the peak temperature rise in the combustion chamber. It can be seen in 30% fish oil methyl ester blends that the addition of higher alcohol increased not only the fuel consumption but also the NOx formation. The BTE is also suffered drastically. It can be concluded from the trade-off study that the presence of higher alcohol not only benefited the 20% MEFO blends but also increased with the increase of higher alcohol percentage.

### ANFIS as a system identification tool

Fuzzy inference system (FIS) as the basis of ANFIS is a technique concerning with fuzzy rules that are engaged to derive a new approximated fuzzy-set inference while captivating fuzzy-set as a foundation [30],[31]. Fuzzy inference system is predominantly enforced to the circumstances that either the system is complex to be quite sculpted or the depiction about the reviewing issues are equivocal and confusing [27]. An ANFIS model has the following components

- A grid of some entailing IF-THEN rules.
- A decision-making component that executes the inference system of rules.
- A fuzzification system interface, transferring the input of the system to a fuzzy ruled set processed by fuzzy inference system unit.
- A defuzzification system interface, swapping the fuzzy ruled conclusion to the original output.

FIS is employed to converge input criterion to membership functions (MFs), later on these input MFs into a bunch of if-then rule metrics, rules into a grid of output responses, output responses into output MFs, and finally the output MFs to output or a decision linked with the output response [32]. A typical ANFIS model comprises of five layers with and a two input factors x, y and one response K is demonstrated in Figure 8. The very first one is a fuzzy layer in which membership functions are constructed. The following equation gives a membership function for a node I with a node function  $\Phi$ .

$$K_i^1 = \Phi_{F_i}(y) \quad (4)$$

where y is an input to the node I,  $F_i$  is a membership function for the output K. Triangular, and bell-shaped MFs are common. The second layer is the product layer in which it acts as a simple multiplier. The output of the node can be depicted as:

$$K_i^2 = \alpha_i = \Phi_{F_i}(y) \times \Phi_{F_i}(x) \text{ For } i=1, 2, 3, \dots \text{etc} \quad (5)$$

$\alpha_i$  are called the firing strengths of all rules framed. The normalised layer is the third layer and is given by the ratio of firing strength to the total strengths.

$$K_i^3 = \bar{\alpha}_i = \frac{\alpha_i}{\alpha_1 + \alpha_2} \text{ For } 1, 2, 3, \dots \text{etc} \quad (6)$$

The fourth layer being the defuzzifying layer in which the consequential parameters further process the output of the third layer and are given by:

$$K_i^4 = \bar{\alpha}_i g_i = \bar{\alpha}_i (a_i x + b_i y + r_i) \text{ For } i=1, 2, 3, \dots \text{etc} \quad (7)$$

The last and final layer is summing junction where all input signals were added up.

$$K_i^5 = \sum_{i=1}^2 \bar{\alpha}_i g_i = \frac{\sum_{i=1}^2 \alpha_i g_i}{\sum_{i=1}^2 \alpha_i} \quad (8)$$

In general, the two adaptable parameter criterion sets,  $\{a_i, b_i, c_i\}$  termed as premise parameter criterion and  $\{p_i, q_i, r_i\}$  termed as consequent parameter criterion are in practice. The goal of training algorithm intended for this particular architecture is to adjust the overhead parameter criterion sets to sort the ANFIS response output that maps the training data. The proposed ANFIS model supports the Sugeno-type architectures and should have the following properties:

1. The structure should be Sugeno type.
2. All rules should have equal and unit weightage value.
3. All membership functions should be either linear or constant type.
4. No rule sharing among membership functions.

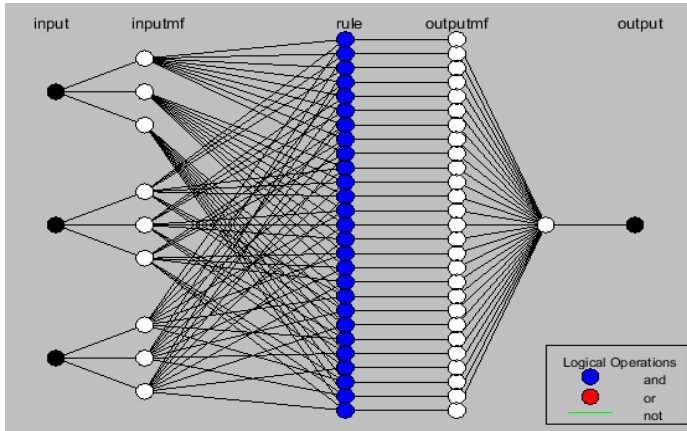


Figure 8: ANFIS Structure

The principal limitation of the ANFIS models is with the number of input factors. Beyond five inputs, the computational time and rules will increase, so ANFIS will not be prepared to model output concerning data. In this study, three input factors used and five output responses are used. Depending on the nature of the problem, the choice of various membership



functions, nature of MFs (triangular, Gaussian trapezoidal, sigmoid, and bell-shaped), type of output MFs (linear or constant), optimization approach (hybrid or back propagation) and finally the number of epochs produce a robust and competent model.

The entire experimental dataset is separated into two major classes explicitly training, and validation sets and therefore 70% of the entire experimental dataset is arbitrarily designated for training, and the residual data set is used for performance investigation of the generated ANFIS model. The MATLAB-16 toolbox is employed for building the designated ANFIS model. At this juncture, the grid partitioning practice is employed to create the Sugeno based FIS structure to launch a relationship among the input factors, and output responses contingent on specific framed rules and an optimum training of the neuro-fuzzy algorithm is contingent on hybrid learning technique. As the training program is completed the performance of the Sugeno is estimated by serving the input dataset to the fuzzy interface system, and the engine response can be characterized with reference to correlation matrix among the actual and predicted data.

### Performance evaluation

The performance of the network was evaluated using some special statistical error metrics like correlation coefficient (R), mean absolute percentage error (MAPE) and root mean square error (RMSE). These error metrics are often defined concerning the predicting error, the difference between actual response and the predicted response and that could be seen by commissioning Equation 8, 9, and 10.

$$R = \sqrt{1 - \left\{ \frac{\sum_{i=1}^n (e_i - p_i)^2}{\sum_{i=1}^n (p_i)^2} \right\}} \quad (9)$$

$$RMSE = \sqrt{\frac{\sum_{i=1}^n (e_i - p_i)^2}{n}} \quad (10)$$

$$MAPE = \sum_{i=1}^n \left| \frac{e_i - p_i}{e_i} \right| \times \frac{100}{n} \quad (11)$$

where  $p_i$  and  $e_i$  are individual predicted response and the actual response of the  $i_{th}$  iteration and  $n$  is the sample size of the dataset. By the previous literature, the values  $R > 0.98$ ,  $MSE < 0.001$  and  $MAPE < 5\%$  are healthy for a robust model [22]

### Evaluation of ANFIS model and Error Analysis:

The model seems to be robust as the mathematical parameters like R, RMSE and MAPE appear to be an acceptable threshold. Based on this research, the

Regression values are ranging from 0.9967 to 0.9999 (Very close to unity) that shows the agreement of the predicted data with the experimental data. The RMSE is ranging 0.000026 to 0.0000336 (shallow values) which shows the homogeneity among the data and MAPE is very low ranging from 0.0021 to 0.0028.

## **Conclusions**

The experimental investigation that was piloted to find the possibility of Fishoil methyl ester as an alternative to petrodiesel. Based on the experimental observations the following conclusions were drawn.

1. The pure fish oil methyl esters resulted in higher specific fuel consumption and lowered thermal efficiency when compared to petrodiesel. The reason is due to low volatility and higher kinematic viscosity of Fishoil biodiesel than conventional fuels.
2. Dilution of MEFO with petrodiesel in varying proportions resulted in reducing kinematic viscosity significantly, which was further reduced by adding n-pentanol in the blends.
3. MEFO along with n-pentanol, and its blends with petrodiesel oil were compatible with petrodiesel at higher loading conditions from the perspective of engine performance.
4. Physical and chemical properties test revealed that the Fishoil methyl ester blends have almost all properties similar or better than that of the petrodiesel fuel, except viscosity which is slightly higher than that of petrodiesel suitable as fuel for CI engines without any engine modification.
5. Brake thermal efficiency results show improvement for all MEFO blends and m20p10 shows better results among all with 6.28% higher than petrodiesel.
6. Emission test shows a reduction in per cent of CO and HC in exhaust gases for m30p10 and m20p10 fuels concerning diesel oil at higher power output.
7. The blends of fish oil methyl ester and diesel m20p10 proved promising as an alternative to petrodiesel fuel for running the CI engine with less emission of NOx, CO and HC and better engine performance.

The proposed model with ANFIS found robust as the mathematical parameters like R, RMSE and MAPE are located in an acceptable threshold.

## References

- [1] A. L. Paladugula et al., “A multi-model assessment of energy and emissions for India’s transportation sector through 2050,” *Energy Policy* 116 (January), 10–18 (2018).
- [2] International Energy Agency, “2018 World Energy Outlook: Executive Summary,” 2018.
- [3] “Energy Outlook 2035,” no. January, 2014.
- [4] G. Sakthivel, C. M. Sivaraja, and B. W. Ikua, “Prediction OF CI engine performance, emission and combustion parameters using fish oil as a biodiesel by fuzzy-GA,” *Energy*, 287–306 (2019).
- [5] A. I. El-Seesy, H. Hassan, and S. Ookawara, “Effects of graphene nanoplatelet addition to jatropha Biodiesel–Diesel mixture on the performance and emission characteristics of a diesel engine,” *Energy* 147, 1129–1152 (2018).
- [6] C. F. Borges, “On polynomial function approximation with minimum mean squared relative error and a problem of Tchebycheff,” *Appl. Math. Comput.* 258, 22–28 (2015).
- [7] I. M. Rizwanul Fattah, A. E. Atabani, M. A. Kalam, H. H. Masjuki, A. Sanjid, and S. M. Palash, “Biodiesel production, characterization, diesel engine performance, and emission characteristics of methyl esters from *Aphanamixis polystachya* oil of Bangladesh,” *Energy Convers. Manag.* 91, 149–157 (2014).
- [8] J. F. Reyes and M. A. Sepúlveda, “PM-10 emissions and power of a Diesel engine fueled with crude and refined Biodiesel from salmon oil,” *Fuel* 85 (12–13), 1714–1719 (2006).
- [9] G. Sakthivel, G. Nagarajan, M. Ilangkumaran, and A. B. Gaikwad, “Comparative analysis of performance, emission and combustion parameters of diesel engine fuelled with ethyl ester of fish oil and its diesel blends,” *Fuel* 132, 116–124 (2014).
- [10] K. Bhaskar, G. Nagarajan, and S. Sampath, “Optimization of FOME (fish oil methyl esters) blend and EGR (exhaust gas recirculation) for simultaneous control of NOx and particulate matter emissions in diesel engines,” *Energy* 62, 224–234 (2013).
- [11] F. Preto, F. Zhang, and J. Wang, “A study on using fish oil as an alternative fuel for conventional combustors,” *Fuel* 87 (10–11), 2258–2268 (2008).
- [12] T. Zhang, K. Munch, and I. Denbratt, “An Experimental Study on the Use of Butanol or Octanol Blends in a Heavy Duty Diesel Engine,” *SAE Int. J. Fuels Lubr.* 8 (3), 24–2491 (2015).
- [13] I. M. Monirul, H. H. Masjuki, M. A. Kalam, N. W. M. Zulkifli, and I. Shancita, “Influence of polymethyl acrylate additive on the formation of particulate matter and NOX emission of a biodiesel–diesel-fueled engine,” *Environ. Sci. Pollut. Res.* 24 (22), 18479–18493 (2017).

- [14] S. Godiganur, C. Suryanarayana Murthy, and R. P. Reddy, "Performance and emission characteristics of a Kirloskar HA394 diesel engine operated on fish oil methyl esters," *Renew. Energy* 35 (2), 355–359 (2010).
- [15] A. L. Paladugula et al., "Optimization of diesel engine performance and emission parameters employing cassia tora methyl esters-response surface methodology approach," *Renew. Sustain. Energy Rev.* 15 (8), 84–115 (2018).
- [16] L. Li, J. Wang, Z. Wang, and H. Liu, "Combustion and emissions of compression ignition in a direct injection diesel engine fueled with pentanol," 1–7 (2014).
- [17] M. Pan et al., "Effect of EGR dilution on combustion, performance and emission characteristics of a diesel engine fueled with n-pentanol and 2-ethylhexyl nitrate additive," *Energy Convers. Manag.* 176 (July), 246–255 (2018).
- [18] M. Raza, L. Chen, R. Ruiz, and H. Chu, "Influence of pentanol and dimethyl ether blending with diesel on the combustion performance and emission characteristics in a compression ignition engine under low temperature combustion mode," *J. Energy Inst.* February, 1–12 (2019).
- [19] C. S. Cheung, Y. Di, and Z. Huang, "Experimental investigation of regulated and unregulated emissions from a diesel engine fueled with ultralow-sulfur diesel fuel blended with ethanol and dodecanol," *Atmos. Environ.* 42 (39), 8843–8851 (2008).
- [20] M. Deb, A. Paul, D. Debroy, G. R. K. Sastry, R. S. Panua, and P. K. Bose, "An experimental investigation of performance-emission trade off characteristics of a CI engine using hydrogen as dual fuel," *Energy* 85, 569–585 (2015).
- [21] S. A. Fenjan, H. Bonakdari, A. Gholami, and A. A. Akhtari, "Flow Variables Prediction Using Experimental, Computational Fluid Dynamic and Artificial Neural Network Models in a Sharp Bend," *Int. J. Eng.* 29 (1), 14–22 (2016).
- [22] S. Bhowmik, R. Panua, S. K. Ghosh, D. Debroy, and A. Paul, "A comparative study of Artificial Intelligence based models to predict performance and emission characteristics of a single cylinder Diesel engine fueled with Diesosenol.," *J. Therm. Sci. Eng. Appl.*, no. c, (2017).
- [23] Y. Singh, A. Sharma, S. Tiwari, and A. Singla, "Optimization of diesel engine performance and emission parameters employing cassia tora methyl esters-response surface methodology approach," *Energy* 168, 909–918 (2019).
- [24] T. Yusaf et al., "SVM and ANFIS for prediction of performance and exhaust emissions of a SI engine with gasoline–ethanol blended fuels," *Appl. Therm. Eng.* 95, 186–203 (2015).
- [25] R. Gautam, N. Kumar, H. S. Pali, and P. Kumar, "Experimental studies

- on the use of methyl and ethyl esters as an extender in a small capacity diesel engine,” *Biofuels* 7 (6), 637–646 (2016).
- [26] J. Campos-Fernandez, J. M. Arnal, J. Gomez, N. Lacalle, and M. P. Dorado, “Performance tests of a diesel engine fueled with pentanol/diesel fuel blends,” *Fuel* 107, 866–872 (2013).
- [27] K. Yang, L. Wei, C. S. Cheung, C. Tang, and Z. Huang, “The effect of pentanol addition on the particulate emission characteristics of a biodiesel operated diesel engine,” *Fuel* 209 (July), 132–140 (2017).
- [28] J. K. Panda, G. R. K. Sastry, and R. N. Rai, “A Taguchi-Fuzzy-Based Multi-Objective Optimization of a Direct Injection Diesel Engine Fueled With Different Blends of Leucas Zeylanica Methyl Ester and 2-Ethylhexyl Nitrate Diesel Additive With Diesel,” *J. Energy Resour. Technol.* 139 (4), 042209 (2017).
- [29] A. Atmanli, “Effects of a cetane improver on fuel properties and engine characteristics of a diesel engine fueled with the blends of diesel, hazelnut oil and higher carbon alcohol,” *Fuel* 172, 209–217 (2016).
- [30] A. Bahramifar, R. Shirkhani, and M. Mohammadi, “An ANFIS-based approach for predicting the manning roughness coefficient in alluvial channels at the bank-full stage,” *Int. J. Eng. Trans. B Appl.* 26 (2), 177–186 (2013).
- [31] M. S. Lashkenari, A. Khazaiepour, S. Ghasemi, and M. Ghorbani, “Adaptive Neuro-fuzzy Inference System Prediction of Zn Metal Ions Adsorption by  $\gamma$ -Fe<sub>2</sub>O<sub>3</sub>/Polyrhodanine Nanocomposite in a Fixed Bed Column,” *Int. J. Eng.* 31 (10), 1617–1623 (2018).
- [32] B. Khoshnevisan, S. Rafiee, M. Omid, and H. Mousazadeh, “Development of an intelligent system based on ANFIS for predicting wheat grain yield on the basis of energy inputs,” *Inf. Process. Agric.* 1 (1), 14–22 (2014).

# Fatigue Life Assessment Approaches Comparison Based on Typical Welded Joint of Chassis Frame

Maksym Starykov\*  
Liebherr Container Cranes Ltd, Ireland  
m.starykov@gmail.com

## ABSTRACT

*There are many approaches to the durability calculation that are used in engineering practice. At the same time the existing accident studies show that the leading position is still hold by fatigue failures. This means that there is still no universal approach to fatigue problem solution, and the existing approaches have their limitations. In addition, there is lack of information about the comparison between the precision of the obtained results using different approaches. In this paper different fatigue life calculation methods, like nominal stress, hot spot stress, notch stress and fracture mechanics are used to calculate the durability of T-type welded joint. The obtained results are compared with the fatigue test ones and the approaches, which give the closest results, are found.*

**Keywords:** Metal Fatigue; Nominal Stress; Hot Spot Stress; Notch Stress; Fracture Mechanics

## Introduction

Time varying working loads are typical for metal constructions of chassis frames, material handling machines, ship hulls etc. According to accident studies for offshore structures [1], that took place in the North Sea, for period from 1972 to 1992, all reasons have been split into several groups according to their significance:

- fatigue 25%;
- structure collision with a ship 24%;
- dropping objects 9%;

- corrosion 6%

In spite of the existence of different guides and approaches that have being used for fatigue design the significant part of failures caused by fatigue reveals the imperfection of using analysis methods. That is why the development of a new methodology is the pressing issue.

Modern fatigue design approaches are based on stress information about designing joint received from the finite element analysis of a structure. This gives the possibility of using the local stress in the probable area of the fatigue crack appearance instead of using nominal stress in the joint and broadens horizons for further enhancements.

Metal fatigue phenomena have been attracting a lot of researchers' interest for a long time and with the welding invention this interest even increased. The main problem was that all of researches solved particular problems (i.e. the effect of mean stress on the durability etc.) but there was no general practical approach with thorough step by step recommendations for the practicing engineers how to perform the analysis. The situation is changed during last decade when International Institute of Welding [2]-[5], British Standard [6][7], and DNV [8][9] have represented researches that are summarized in particular guides for the fatigue analysis with detailed description of practical utilization of the approaches, starting from mesh description and finishing with recommendations about what type of S-N curve to use.

With the aforementioned guides in the place the question of the analysis result validation has appeared. Thus, many researches have their goal to compare the fatigue experiment and analysis results [10]-[13]. The main problem in our opinion is that in those researches only one method of the analysis is compared with the test results. But at the same time in engineering practice at least four of them are frequently used:

- nominal stress approach;
- hot spot stress approach;
- notch stress approach;
- fracture mechanics approach.

In this paper the comparison between main analytical approaches and test results for the fatigue life assessment has been done. This comparison could help to the practicing engineer to decide which approach to the durability analysis is more accurate for designing of similar joints.

For the analysis the T-type welded joint (Figure 1) is chosen. Despite the fact that this type of connection is typical for a chassis frame, it is not covered in the researches. All the existing analysis, done for the T weld connection [10]-[13], have their welded gusset plate serving for stress concentration purpose only, when in the T-weld connection that is studied, the force and moment are transmitted to the main plate (crossbeam) through the gusset plate (longeron).

In the following chapters, the durability of the joint is obtained using testing and different analysis approaches. The results are discussed in clause “Discussion of the obtained results”.

### Fatigue test results

The article objective is to define the approaches that give the closest result of fatigue life assessment to ones taken from fatigue test for T-type welded joint of a chassis frame [14].

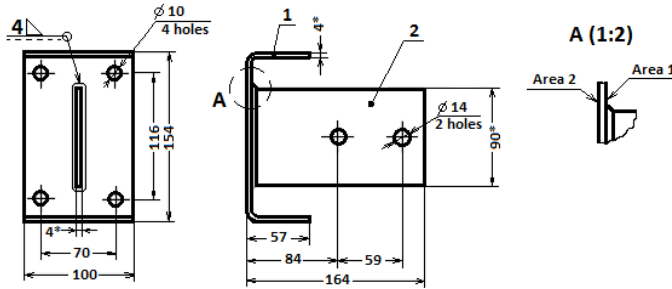


Figure 1: Crossbeam to longeron T-type welded joint from 93571 ODAZ trailer chassis frame (1 – crossbeam; 2 – longeron) acc. [14]

Specimens have been tested using symmetric stress cycle ( $R = -1$ ). The crossbeam was fixed using 4 holes of 10 mm in diameter and the 2 forces were applied using the 2 holes of 14 mm in diameter in longeron. The fact of the crossbeam vertical deformation amplitude increasing beyond 30% has been used as a collapse criterion to stop the fatigue tests. The six joints have been tested on 6 different stress levels (Table 1). The fatigue curve of Weibull type has been used:

$$m_w \cdot \lg(\sigma) + \lg N = C_w \quad (1)$$

where  $\sigma$  is the nominal stress, MPa;  $N$  – durability, cycles;  $m_w$  and  $C_w$  are empirical parameters. Using linear interpolation on test data (Figure 2), the following values of parameters in Equation (1) have been found:  $m_w = -2.489$ ;  $C_w = 3.3319$ .

Table 1: Fatigue test results for T-weld joint crossbeam to longeron acc. [14]

Max. nominal stress in the crossbeam (amplitude) $\sigma$ , MPa	160	140	120	100	80	60
Fatigue life $N$ , cycles	39800	63100	102300	182000	478600	2089300



Based on Equation (1), the fatigue life for stress amplitude  $\sigma_{a\_nom} = 81.5$  MPa with 50% failure probability is 425 100 cycles.

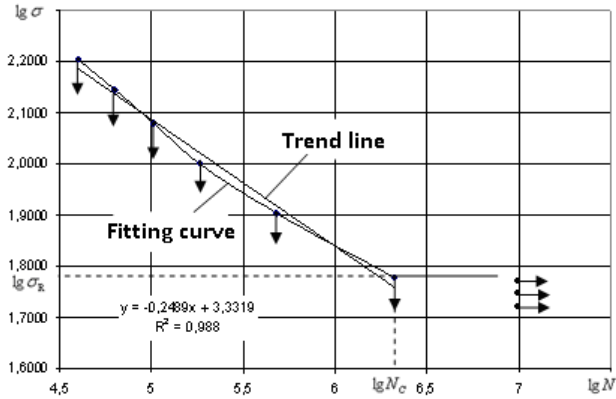


Figure 2: Nominal stress in crossbeam vs the number of stress cycles (S-N curve) obtained from fatigue tests acc. [14]

Fatigue life with failure probability of 2.3% has been calculated using next Equation (2):

$$lgN_{P=2.3\%} = lgN_{P=50\%} - z_{P=2.3\%} \cdot lg\sigma_N = 187\,280 \quad (2)$$

where  $d$  – standard deviation amount below mean value;  $z_{P=2.3\%} = z_{P=97.7\%} = 2$  (quantile for failure probability of 2.3%);  $lg\sigma_N$  - standard deviation of  $lgN$ , 0.178, p. 20 [2] for the specimen amount  $n < 10$ .

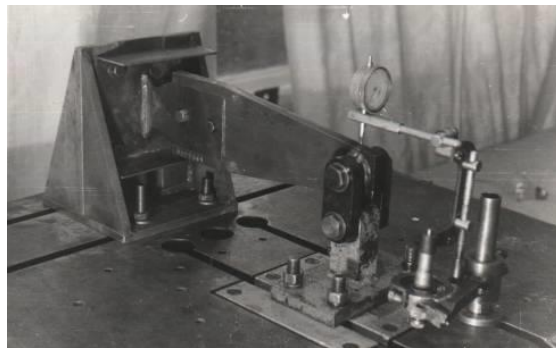


Figure 3: Test machine acc. [14]

Fatigue life with failure probability of 97.7% has been calculated using Equation (3):

$$\lg N_{P=97.7\%} = \lg N_{P=50\%} + z_{P=97.7\%} \cdot \lg \sigma_N = 964\,920 \quad (3)$$

Traditionally beam theory for nominal stress calculation is used for S-N curve. But that stress is not representative for current joint because the fracture happens not in the crossbeam outer layers but in the area of welding seam transition to the longeron (Areas 1 and 2, Figure 1).

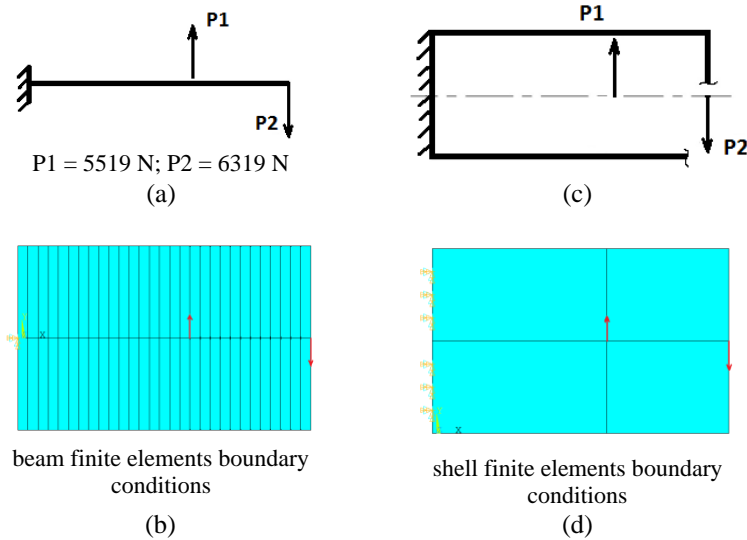


Figure 4: Crossbeam stress calculation using finite elements of beam and shell types

Using the shell finite elements gives realistic results. Maximum stress in crossbeam for the beam finite element (Figure 4(a) and (b)) is 81.5 MPa, and for shell finite element (Figure 4(c) and (d)) is 159 MPa. Moreover, stress state of crossbeam in the area of welding seam is not more uniaxial one but complex i.e. all three principal stresses have non zero magnitudes.

### **Nominal Stress approach**

The first step of nominal stress analysis [6] is to find among the variety of joint types with boundary conditions (showed in standard) the one that corresponds to the designing joint. But for currently calculating T-type welded connection the similar joint type does not exist. For the first look

Type 5.3 (class F2, Figure 5(a)), clause 2, Table 1 [6], could be taken, but its boundary conditions are different from analysing connection: unlike to the join from the standard the gusset plate (longeron) does not takes any load. That is why it cannot be used further on. The joint on Figure 5(b) cannot be used for calculating either, because its boundary conditions differ from designing joint's ones. It is also not clear stress in which element is taken for nominal (loading scheme is not shown).

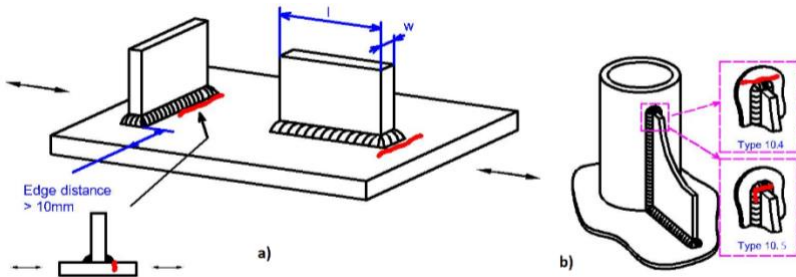


Figure 5: Nominal Stress approach joint classification

### Hot spot stress approach

This approach [3] allows calculating the joint fatigue life using its stress-strain state data obtained from the finite element analysis. The following joint modelling techniques are suggested to be used:

- Modelling using shell finite elements. In this case welding seam is to be create in such ways:
  - Model without welding seams;
  - Using oblique shell elements to model welding seams;
  - Using shell element with increased thickness for welding seams modelling;
- Solid modelling with volume finite elements. Idealized welding seam shape is used.

### Modelling using shell elements

#### Model without welding seams

According to IIW Recommendations [3] welded element durability is to be calculated based on stress that acts in the weld toe. However, because of using linear elastic metal behaviour and the fact that the real weld profile is unknown on design stage, there is no possibility to use directly the stress read from welding toe. Instead, it has been proposed to use stress extrapolated value based on stress in the welding seam vicinity, so called Structural Stress.

For our case (model consists of 4 node linear shell finite elements with edge of 1.6 mm near the stress concentration point) the hot spot stress is given by:

$$\sigma_{hs} = 1.67 \cdot \sigma_{0.4t} - 0.67 \cdot \sigma_{1t} \quad (4)$$

where  $\sigma_{0.4t}$  - stress value at the distance of  $0.4 \cdot t$  from the weld toe (the first extrapolation point);  $\sigma_{1 \cdot t}$  - stress value at the distance of  $1 \cdot t$  from the weld toe (the second extrapolation point);  $t$  – longeron thickness, 4 mm.

The finite element model of T-welded connection is shown in Figure 6. The minimum thickness of the plate the approach is applicable for is 5 mm. Area of the stress concentration has been meshed using two techniques (Figure 7).

In currently overlooking standard the fatigue life assessment is based on the principal stress biggest range during loading cycle. However, if the angle between this stress direction and normal to the welding seam line is more than 60 degrees, the stress perpendicular to the welding seam must be used. In our case  $S_y$  is used. Hot spot stress approach is much easier to use in comparison with the nominal stress approach because it is based only on two S-N curves to assess the fatigue life in a “hot spots”. They are known as FAT 90 and FAT 100.

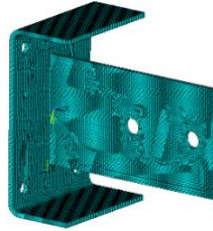


Figure 6: Finite element model

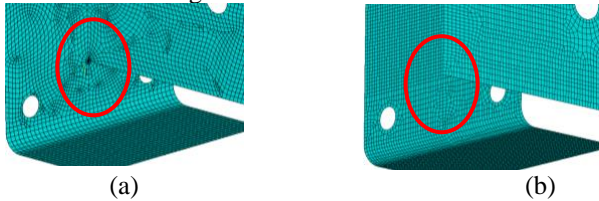


Figure 7: Stress concentrator area meshing. Concentrators are circled by red line

Results of finite element analysis are shown on Figure 8; hot spot stress extrapolation calculation is put into Table 2.

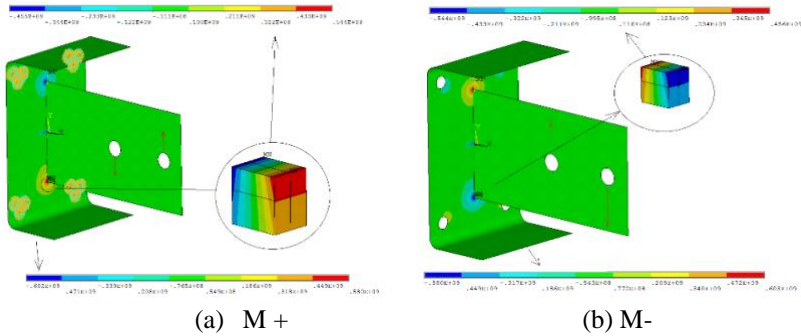


Figure 8: Sy stress graphical plots for the boundary conditions shown in Figure 4 (mesh is acc. Figure 7 (a))

Table 2: “Hot spot” stress approximation and durability assessment

Finite element mesh type in the concentrator vicinity	Hot spot stress calculated based on Sy, MPa		“ hot spot” stress, $\sigma_{hs\_max}(+M)$ , MPa	“ hot spot” stress, $\sigma_{hs\_max}(-M)$ , MPa	“ hot spot” stress range, $\Delta\sigma_{hs}$ acc. (4), MPa	Thickness correction <sup>1</sup>	Fatigue life		
	nearest to the welding seam point, $\sigma_{0.4-t}$	farthest from the welding seam point, $\sigma_{0.1.0-t}$					Failure probability 2.3%	Failure probability 50% *	Failure probability 97.7% <sup>2</sup> *
Figure 7(a)	497	355	592	-592	1184	Yes	1 205	2 735	6 209
						No	6 239	14 161	32 140
Figure 7(b)	439	281	545	-545	1090	Yes	1 544	3 508	7 962
						No	7 996	18 150	41 200

\*Durability corresponding to different failure probabilities than other than 2.3% are calculated acc. (2) and (3).

The numbers that come after letters “FAT” indicate stress level in MPa that corresponds to  $2 \cdot 10^6$  cycle durability. The general equation for these S-N curves is as follows:

<sup>1</sup> Thickness correction according to [3] could be calculated for as-welded T-joints as  $f(t) = \left(\frac{t_{ref}}{t_{eff}}\right)^{0.2} = 1.73$ , where  $t_{ref} = 25mm$ ,  $t_{eff} = 4mm$  is the joint plate thickness. This factor is used for FAT scaling, so for FAT 100 it will be FAT 173. This correction is used normally for plates thicker than 25 mm, but the guide says that „in the same way a benign effect might be considered, but this should be verified by component test“.

<sup>2</sup>Durability corresponding to different failure probabilities are calculated acc. (2) and (3).

$$\Delta\sigma_{hs}^m \cdot N = C \quad (5)$$

where  $\Delta\sigma_{hs} = \sigma_{hs\_max} - \sigma_{hs\_min}$  - stress range in the «hot spot»,  $\sigma_{hs\_max}$  - maximum hot spot stress of a cycle,  $\sigma_{hs\_min}$  - minimum hot spot stress of a cycle;  $m$  – index of power, 3.0;  $C$  – coefficient,  $2 \cdot 10^{12}$ ;  $N$  – life cycle.

Plane model with shell finite elements. Welding seam is modelled by oblique shell elements

The main concept of welding seam modelling is shown in Figure 9 and meshed model – in Figure 10 (a).

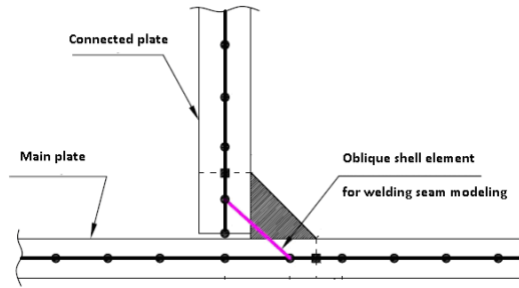
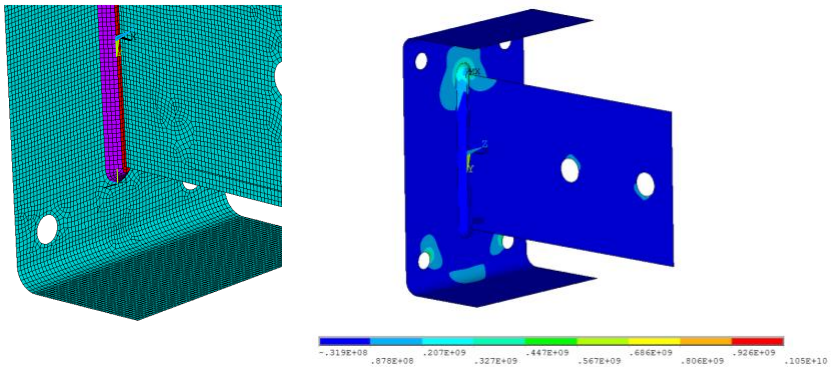


Figure 9: Welding seam modelling with oblique shell elements

For this case first principal stress is perpendicular to the welding seam. That is why it is used for the further analysis.



(a) Finite element model

(b) First principal stress graphical plot

Figure 10: Example of welding seam modelling with oblique shell elements.

Table 3: “Hot spot” stress approximation and durability assessment

Hot spot stress calculated based on S1, MPa		“ hot spot” stress range, $\Delta\sigma_{hs}$ acc. (4), MPa	Thickness correction†	Fatigue life		
nearest to the welding seam point, $\sigma_{0.4t}$	farthest from the welding seam point, $\sigma_{1.0t}$			Failure probability 2.3%	Failure probability 50 % *	Failure probability 97.7% *
274	194	328	Yes	56 680	128 500	291 700
			No	293 500	666 100	1 512 000

\*Durability corresponding to different failure probabilities than other than 2.3% are calculated acc. (2) and (3).

**Solid model with volume finite elements**

Solid model of the crossbeam-longeron welding connection is shown in Figure 11. To reduce the computation time during model stress analysis only one half of the model has been created. 20 node Solid finite element with decreased integration and edge size of 4 mm is used.

The distances from the weld toe to the extrapolation points are the same (0.4·t to the first (nearest to weld) extrapolation point and 1·t to the second extrapolation point). Stress analyses result is shown in Figure 12.

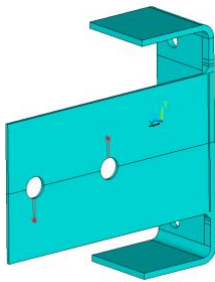


Figure 11: Crossbeam-longeron welding connection solid model.

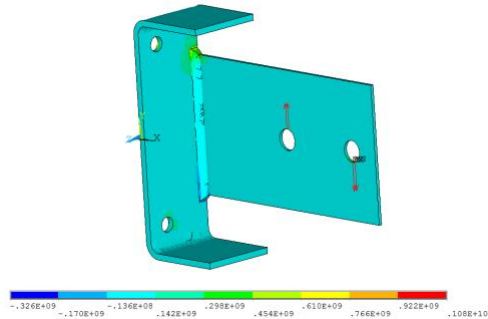


Figure 12: 1st principal stress graphical. Plots/ for the boundary conditions shown in Figure 4

Table 4: “Hot spot” stress approximation and durability assessment

Hot spot stress calculated based on S1, MPa		“hot spot” stress range, $\Delta\sigma_{hs}$ acc. (4), MPa	Fatigue life		
nearest to the welding seam point, $\sigma_{0.4-t}$	farthest from the welding seam point, $\sigma_{1.0-t}$		Failure probability 2.3%	Failure probability 50% *	Failure probability 97.7% *
335	228	407	29 670	67 300	152 800

\*Durability corresponding to different failure probabilities than other than 2.3% are calculated acc. (2) and (3).

### Notch Stress approach

This approach [4, 5] demands solid model creation and volume finite element mesh using. For the plate thickness less than 5 mm, the notch radius of 0.05 mm instead of 1 mm has to be used, special attention must be paid to a weld seam modelling particularly in the area where welding seam material merges to the main metal (Figure 13 b) because the stress in this area is used for the fatigue life estimation. Only one S-N curve uses for this analysis (FAT 630) which equation takes a form of:

$$\Delta\sigma^m \cdot N = C \quad (6)$$

where the equation parameters are  $m = 3$ ;  $C = (FAT)^m \cdot 2 \cdot 10^6$ . In addition to the weld toe modelling radius (Figure 14) the approach specifies the welding seam geometry creation method, finite element size etc.

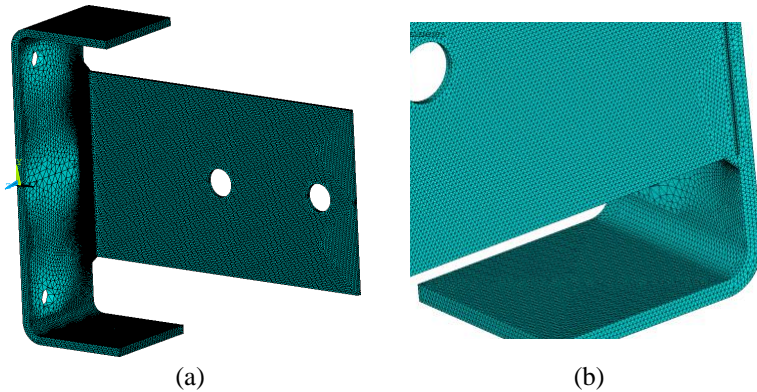


Figure 13: Crossbeam-longeron welding connection model for notch stress analysis



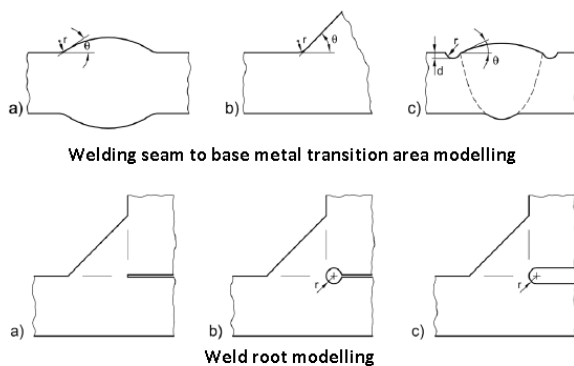


Figure 14: Welding seam modelling requirements

Due to the high level of detail needed for welding area modelling, the scope of problem increases with the growth of the joint complexity. That is why calculation time could increase from i.e. 20 minutes to several days. In this case, the sub-modelling feature is very useful. It helps to create more dense mesh and retrieve more precise solution for the smaller part of a model. For crossbeam-longeron joint welding seam area sub-model of a fatigue crack initiation is shown in Figure 15.

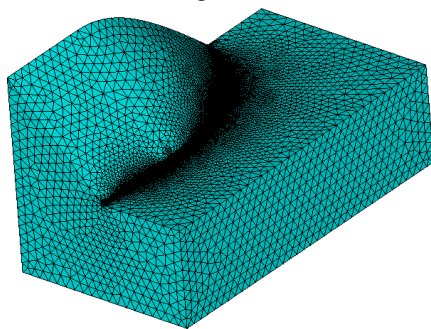
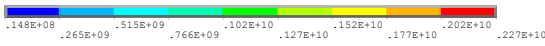
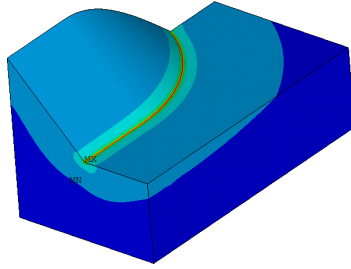


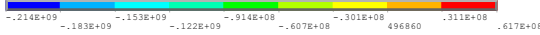
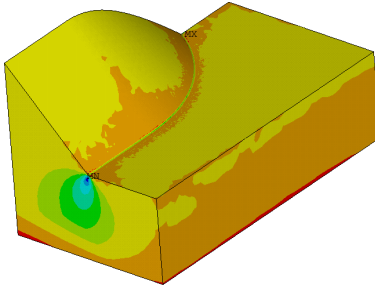
Figure 15: Crossbeam-longeron welding connection sub-model

S1 (AVG)  
DMX = .115E-03  
SMN = .148E+08  
SMX = .227E+10



+ M – bending  
force direction  
according Figure  
4

S1 (AVG)  
DMX = .115E-03  
SMN = -.214E+09  
SMX = .617E+08



- M – bending  
force direction  
according Figure  
4

Figure 16: First principal stress graphical plot for subassembly

Table 5: Principal stress variation during cycle and durability assessment

	Notch stress for +M (Figure 16a)	Notch stress for -M (Figure 16b)	$\Delta\sigma_{\text{notch}}$	N (failure probability 2.3%)	N (failure probability 50%)*	N (failure probability 97.7%)*
S1 (first principal stress)	-30	2110	2140	51 030	131 800	340 400

\*Durability corresponding to different failure probabilities than other than 2.3% are calculated acc. (2) and (3). According [5] standard deviation of the  $\lg N = 0.206$ .

### Fracture Mechanics based approach

The central idea of the approach [2, 3] consists in the using Paris equation for assessment of the joint fatigue stress cycles number till failure:

$$\frac{da}{dN} = A \cdot \Delta K^m \quad (7)$$

where  $a$  – half of crack length, mm;  $N$  – number of stress cycles;  $\frac{da}{dN}$  – crack growth speed, mm/cycle;  $\Delta K$  – stress intensity factor range (SIF)  $N/mm^{3/2}$ ;  $m$  – index of power, and  $A$  – coefficient of proportionality. According to [7], either of two types of the crack growth relationship (Figure 17) could be used.

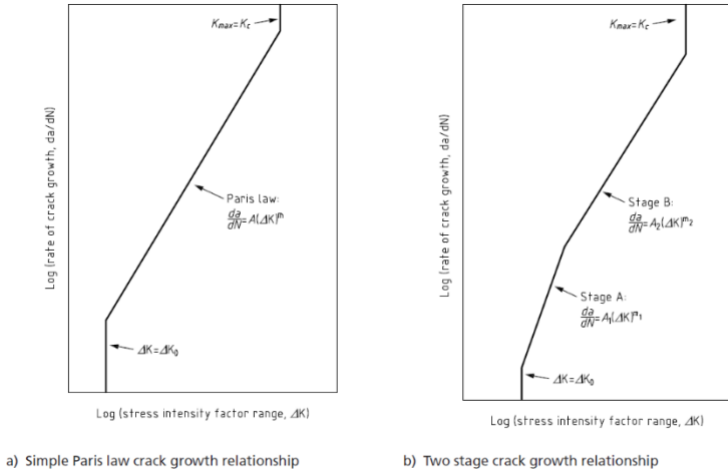


Figure 17: Crack growth relationship (taken from [7])

Using Equation (7), the crack length – stress cycle relationship could be obtained:

$$\int_{a_1}^{a_2} da = \int_{N_1}^{N_2} A \cdot \Delta K^m \cdot dN \quad (8)$$

After solving integral Equation (8) the stress cycle number could be defined ( $N = N_2 - N_1$ ) that is needed for crack growth from length  $2a_1$  to  $2a_2$ .

As per fracture mechanics theory a crack starts to grow if SIF range exceeds some threshold value ( $\Delta K_{TH}$ ), which is different for different grades. Only SIF ranges more than this threshold are considered in analysis. According to [7] for welded structures ( $R > 0.5$ ) it is  $\Delta K_{TH} = 2 MPa \cdot m^{-0.5} = 63 N/mm^{3/2}$ .

The failure criterion for the fatigue testing of the crossbeam-longeron welding connection is the 30% of longeron deformation range increasing.

This corresponds to the crack length of  $L = 2a = 35.5$  mm. The method of solving (8) is as follows:

- Define the SIF variation as the approximation  $\Delta K = \sum_{i=0}^3 c_i \cdot a^i$ . To do this the models of the joint with different crack lengths are created and for each crack length the SIF is calculated (calculation results are shown in Table 6 and Table 7).
- Substitute the obtained approximation into the integral Equation (8) and integrate.

$$\int_{a1}^{a2} \frac{da}{A \cdot [\sum_{i=0}^3 c_i \cdot a^i]^m} = \int_{N1}^{N2} dN \quad (9)$$

The initial limit,  $a1$  corresponds to SIF threshold value of the material ( $170 \text{ MPa}\sqrt{\text{m}}$  for R = -1, acc. (48 c), 8.2.3.6 [7]). Final limit,  $a2 = 17.75$  mm comes from the failure criterion during test.

As the life of crack initiation for welded joints is a small part of the total life [15], we will neglect it. The minimum crack length is defined for each case based on threshold SIF.

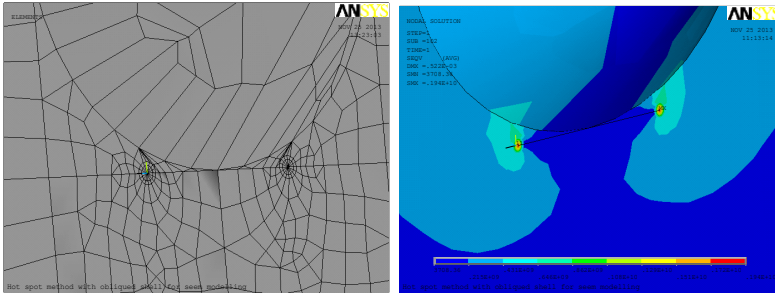


Figure 18: Crack modelling in the welding seam vicinity. The finite elements with shifted nodes have been used

After analysis it became clear, that SIFs for all three modes are nonzero. Next, Equation (10) and (11) have been used to calculate the effective SIF, corresponding to the complex loading, that takes into consideration SIFs for all three different modes. Linear elastic material model has been used.

Table 6: Crack growth modelling results

Crack length ( $L=2a$ ), mm	$a=L/2$ , mm	Bending Moment “+M”			K <sub>eff</sub> “+M” $MPa\sqrt{m}$	$\Delta K_{eff}$ based on (10), $MPa\sqrt{m}$	$\Delta K_{eff}$ , $N \cdot mm^{\frac{3}{2}}$
		K I, $MPa\sqrt{m}$	K II, $MPa\sqrt{m}$	K III, $MPa\sqrt{m}$			
0.1	0.2	0.27	0	0.83	1.03	2.06	64.26
1	0.5	0.61	0	1.73	2.16	4.31	134.74
2	1	0.77	0	2.45	3.03	6.06	189.24
5	2.5	1.18	0.45	4.64	5.69	11.38	355.49
10	5	1	0.87	7.37	8.91	17.82	556.75
20	10	0.55	1.32	9.54	11.49	22.98	718.24
30	15	0.32	1.36	13.5	16.20	32.39	1012.25
40	20	0.44	1.26	15.7	18.81	37.62	1175.78
50	25	0.73	1.44	18.082	21.67	43.34	1354.52
60	30	0.81	1.72	22.13	26.52	53.04	1657.42
71	35.5	0.76	1.28	31.85	38.10	76.19	2381.07

As all three SIF are not equal to 0 the equivalent SIF has to be used for further analysis. First model for equivalent SIF calculation:

$$K_{eff} = \sqrt{K_I^2 + K_{II}^2 + \frac{K_{III}^2}{1-\nu}} \quad (10)$$

Second model for equivalent SIF calculation:

$$K_{eff} = \sqrt[4]{K_I^4 + 8K_{II}^4 + \frac{8K_{III}^2}{1-\nu}} \quad (11)$$

First model for equivalent SIF calculation with one stage crack growth relationship. The SIF approximation is shown in Figure 19 as a trend line equation:

$$\Delta K = 0.1087 \cdot a^3 - 5.2974 \cdot a^2 + 115.64 \cdot a + 71.011 \quad (12)$$

After substituting Equation (12) into (7) and integrating, we have the durability with 2.3% of failure probability.

$$N = \frac{\int_{0.9}^{17.75} \frac{da}{[\sum_{i=0}^3 c_i a^i]^m}}{A} = 421 \text{ 900 cycles}$$

where m - index of power, 3, clause 8.3.3.5, [7]; A – coefficient of proportionality,  $5.21 \cdot 10^{-13}$ , clause 8.3.3.5 [7];  $a_1$  for this case equals to 0.9 mm.

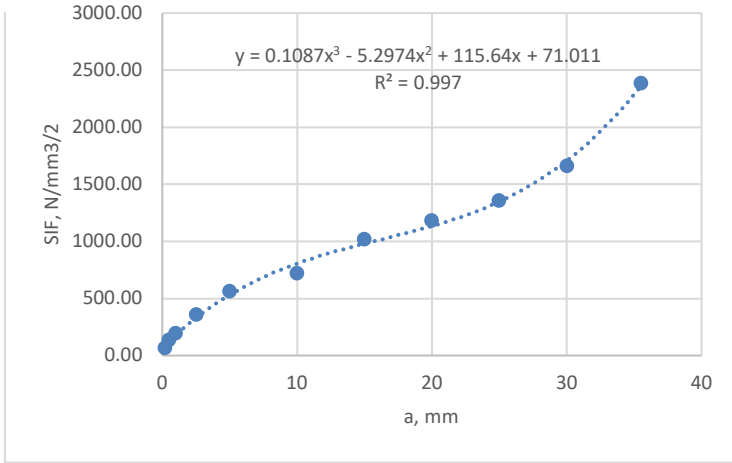


Figure 19: Approximation of SIF range vs. crack length relation (the polynomial approximation is shown above the trend line)

#### First Model for equivalent SIF calculation with two stage crack growth relationship

Total durability would consist of durability for two stages (stage A and stage B). For the Mean Curve (Table 10 [7]) the stage A/Stage B transition point is  $196N \cdot mm^{\frac{3}{2}}$ , which corresponds to  $a = 1.15$  mm.

$$N = N_A + N_B = \frac{1}{A_1} \int_{0.9}^{1.15} \frac{da}{[\sum_{i=0}^3 c_i a^i]^{m_1}} + \frac{1}{A_2} \int_{1.15}^{17.75} \frac{da}{[\sum_{i=0}^3 c_i a^i]^{m_2}} =$$

$$= 150\,300 + 496\,500 = 646\,800 \quad (13)$$

where  $A_1 = 4.8 \cdot 10^{-18}$ ,  $m_1 = 5.1$ ,  $A_2 = 5.86 \cdot 10^{-13}$ ,  $m_2 = 2.88$ . For the Mean Curve + 2SD (Table 10 [7]), the stage A/Stage B transition point is  $144N \cdot mm^{\frac{3}{2}}$ , which is smaller than the threshold value and that why during the Stage A the crack will not propagate.

$$N = N_A + N_B = 0 + \frac{1}{A_2} \int_{0.9}^{17.75} \frac{da}{[\sum_{i=0}^3 c_i a^i]^{m_2}} = 284\,200 \quad (14)$$

where  $A_1 = 2.1 \cdot 10^{-17}$ ,  $m_1 = 5.1$ ,  $A_2 = 1.29 \cdot 10^{-12}$ ,  $m_2 = 2.88$ .

### Second Model for equivalent SIF calculation with one stage crack growth relationship

The SIF approximation is shown in Figure 20 as a trend line equation:

$$\Delta K = 0.1834 \cdot a^3 - 9.1204 \cdot a^2 + 192.7821 \cdot a + 95.3933 \quad (15)$$

After substituting Equation (15) into (7) and integrating we have the durability with 2.3% of failure probability.

$$N = \frac{\int_{0.4}^{17.75} \frac{da}{[\sum_{i=0}^3 c_i \cdot a^i]^m}}{A} = 194\,300 \text{ cycles}$$

where m - index of power, 3, clause 8.3.3.5, [7]; A – coefficient of proportionality,  $5.21 \cdot 10^{-13}$ , clause 8.3.3.5 [7];  $a_1$  for this case equals to 0.4 mm.

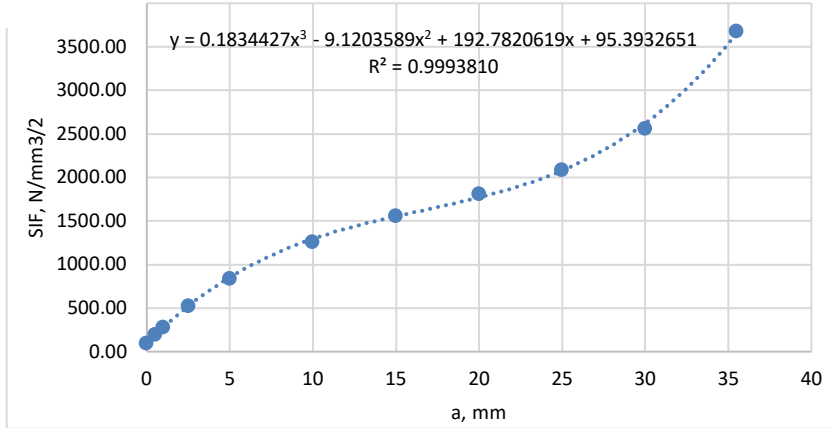


Figure 20: Approximation of SIF range vs. crack length relation (the polynomial approximation is shown above the trend line)

### Second Model for equivalent SIF calculation with two stage crack growth relationship

Total durability would consist of disabilities at two stages (stage A and stage B). For the Mean Curve (Table 10 [7]) the stage A/Stage B transition point is  $196N \cdot mm^{\frac{3}{2}}$ , which corresponds to  $a = 0.55mm$ .

$$N = N_A + N_B = \frac{1}{A_1} \int_{0.4}^{0.54} \frac{da}{[\sum_{i=0}^3 c_i \cdot a^i]^{m_1}} + \frac{1}{A_2} \int_{0.54}^{17.75} \frac{da}{[\sum_{i=0}^3 c_i \cdot a^i]^{m_2}}$$

$$= 84\,240 + 270\,700 = 354\,900 \quad (16)$$

where  $A_1 = 4.8 \cdot 10^{-18}$ ,  $m_1 = 5.1$ ,  $A_2 = 5.86 \cdot 10^{-13}$ ,  $m_2 = 2.88$ .

For the Mean Curve + 2SD (Table 10 [7]) The stage A/Stage B transition point is  $144N \cdot mm^{\frac{3}{2}}$ , which is smaller than the threshold value and that why during the Stage A the crack will not propagate.

$$N = N_A + N_B = 0 + \frac{1}{A_2} \int_{0.4}^{17.75} \frac{da}{[\sum_{i=0}^3 c_i a^i]^{m_2}} = 155\,900 \quad (17)$$

where  $A_1 = 2.1 \cdot 10^{-17}$ ,  $m_1 = 5.1$ ,  $A_2 = 1.29 \cdot 10^{-12}$ ,  $m_2 = 2.88$ .

Fatigue life assessment results for crossbeam to longeron welding connection using different methods are shown in Table 7.

Table 7: Crack growth modelling results

Crack length ( $L=2a$ ), mm	a=L/2, mm	Bending Moment “+M”			K <sub>eff</sub> “+M” $MPa\sqrt{m}$	$\Delta K_{eff}$ based on (11), $MPa\sqrt{m}$	$\Delta K_{eff}$ , $N \cdot mm^{\frac{3}{2}}$
		K I, $MPa\sqrt{m}$	K II, $MPa\sqrt{m}$	K III, $MPa\sqrt{m}$			
0.2	0.01	0.27	0	0.83	1.53	3.05	95.40
1	0.5	0.61	0	1.73	3.18	6.36	198.87
2	1	0.77	0	2.45	4.51	9.01	281.60
5	2.5	1.2	0.5	4.6	8.46	16.92	528.68
10	5	1.1	1	7.3	13.42	26.85	838.94
20	10	0.6	1.4	11	20.23	40.45	1264.13
30	15	0.3	1.4	13.6	25.01	50.01	1562.88
40	20	0.4	1.3	15.8	29.05	58.1	1815.68
50	25	0.7	1.4	18.2	33.46	66.93	2091.47
60	30	0.8	1.7	22.3	41.00	82.00	2562.63
71	35.5	0.8	1.2	32	58.84	117.67	3677.29

## Discussion of the obtained results

- It has been found that for the case of Hot Spot stress approach analysis without weld seam modelling the local orientation of 1st principal stress near the gusset plate to main plate connection ends is not perpendicular to the welding seam and that is the reason for using stress component perpendicular to the seam. At the same time for the cases where the welding seam is modelled (both shell and solid models) the first principal stress is perpendicular to the welding seam. Thus, the local stress strain



state in models without modelled seams does not reflect the reality and the fatigue analysis based on local stress in these areas is not correct.

- The thickness correction for 4 mm plate, applied with “Hot Spot” stress approach, when the higher FAT class is used, gives significant over estimation of the joint durability.
- For the case when weld seam is NOT modelled the lower stress is  $\sigma_{min} \approx |\sigma_{max}|$ , but for models with welding seam  $\sigma_{min} \approx 0$ . As the result the stress range for the models without welding seam is approximately twice bigger than for model with seam modelled.

Table 8: Fatigue life assessment comparison of crossbeam-longeron welding connection for different methods and testing results

Life assessment approach			Stress range, MPa	If thickness correction applied	Durability $N_{2.3\%}^{test}$ , cycles (failure probability 2.3%)	Durability $N_{50\%}^{test}$ , cycles (failure probability 50%)	Durability $N_{97.7\%}^{test}$ , cycles (failure probability 97.7%)	$\frac{N_{cur}^{cur}-N_{2.3\%}^{test}}{N_{2.3\%}^{test}}$ , %	$\frac{N_{cur}^{cur}}{N_{2.3\%}^{test}}$
Fatigue test			81.5	N/A	187280	425100	964920	0	1
Nominal stress approach (BS 7608:1993, FEM 1.001, EN 1993-1-9)			Assessment is impossible. There are no data in Codes that utilize this approach complying to the crossbeam-longeron connection boundary conditions being analysed.						
Hot Spot Stress Analysis	Plane modelling with shell finite elements without welding seam modelling		1184	Yes	1205	2735	6209	-99.36	0.6
				No	6239	14161	32140	-96.67	3.3
			1190	Yes	1544	3508	7962	-99.18	0.8
	No	7994		18150	41200	-95.73	4.3		
	Plane modelling with shell finite elements modelled by oblique shell		328	Yes	56680	128500	291700	-69.74	30.3
No				293500	666100	1512000	56.71	156.7	
Solid modelling with volume finite elements		407	N/A	29670	67300	152800	-84.16	15.8	
Notch Stress Analysis			710	N/A	51300	131800	340400	-72.61	27.4
Fracture mechanics-based approach	One stage crack growth relationship	Keff acc. Eq.10		N/A	421900	-	-	-125.28	225.3
		Keff acc. Eq.11		N/A	194300	-	-	<b>3.75</b>	<b>103.8</b>
	Two stage crack growth relationship	Keff acc. Eq.10		N/A	284200	646800	-	51.75	151.8
		Keff acc. Eq.11		N/A	155900	354900	-	-16.76	83.2

## **Conclusion**

Having analysed obtained results for crossbeam-longeron welding connection and compared them with the fatigue test following conclusion has been done:

1. Fatigue life assessment based on nominal stress approach could be utilized only if the geometry and boundary conditions (type of joint fixation and applying loads) of the analysing joint comply with the one from the existing schemes of the codes, for which data has been originally obtained by fatigue testing. The biggest problem is that the codes do not cover all possible types of boundary conditions. For example, in the case of crossbeam-longeron joint analysis this method could not be used because the appropriate loading scheme could not be found in the standard.
2. The closest to the fatigue test results are given by the fracture mechanics approach based on equivalent Stress Intensity Factor calculated acc. (11) in combination with:
  - a. One stage crack growth relationship (difference with test is 3.75%; the result is NOT conservative as the calculated durability is more than the test results);
  - b. Two stage crack growth relationship (difference with test is - 16.75 %; the result is conservative as the calculated durability is less than the test results).
3. The worst correlation with the test shows the “Hot Spot” stress-based approach without the seam modelling.
4. “Notch Stress” analysis result is close to the one obtained using “Hot Spot” stress analysis.
5. Regarding to the “Notch Stress” approach its main merit is that only this method among described above could predict the durability for the cases where the crack initiates from the weld root. Thus, sometimes it is only one option for analysis.

## **Acknowledgement**

I would like to express my gratitude to the following my colleagues from Liebherr Mining Equipment, USA, for their valuable comments to my paper: James Witfield PE, Dr. Vladimir Pokras, Michael Karge. Special appreciation is to my teacher, Doctor of technical science, Prof. Konoplyov A. V., Odessa National Maritime University, Ukraine, for his permission to use the fatigue test results he has carried out [14].

## References

- [1] Review of Repairs to Offshore Structures and Pipelines, Publication 94/102 Marine Technology Directorate, UK, 1994.
- [2] W. Fricke, Guideline for the fatigue design of welded joints and components XIII-1539-96/XV-845-96, 2010.
- [3] E. Niemi, W. Fricke and S.J. Maddox, Fatigue Analysis of Welded Components. Designer guide to the structural hot-spot stress approach, IIW-1430-00, 2007.
- [4] W. Fricke, IIW Guideline for the Assessment of Weld Root Fatigue IIW-Doc. XIII-2380r3-11/XV-1383r3-11, 2012
- [5] Guideline for the Fatigue Assessment by Notch Stress Analysis for Welded Structures IIW-Doc. XIII-2240r2-08/XV-1289r2-08 Wolfgang Fricke, 2010.
- [6] BS 7608-1993 Fatigue design and assessment of steel structures, 1993.
- [7] BS 7910 Guide on methods for assessing the acceptability of flaws in metallic structures, 1999.
- [8] RP-203: Fatigue Design of Offshore Steel Structures, DNVGL-RP-0005:2014-06.
- [9] Fatigue assessment of ship structures DNVGL-CG-0129, 2015.
- [10] B. Baik, K. Yamada, T. Ishikawa, Fatigue Strength of Fillet Welded Joint subjected to Plate Bending, Steel Structures, 8, 163-169 (2008).
- [11] T. Lassen, N. Recho, Fatigue life analysis of welded structures, ISTE, 2006.
- [12] Comparison of hot spot stress evaluation methods for welded structures J-M. Lee, J-K. Seo, M-H. Kim, S-B. Shin, M-S. Han, June-Soo Park, and M. Mahendran, Inter J Nav ArchitOcEngng 2, 200-210 (2010).
- [13] I. Lotsberg, Fatigue design of plated structures using finite element analysis, Ships and Offshore Structures, 45-54 (2006).
- [14] General classification creation: Doctor of technical science thesis: 05.02.02/ Konoplyov A. V; Odessa National Polytechnical University. – O., 2013. – 39p. [inUkrainian] (Експериментально-розрахункові методи визначення границі витривалості деталей машин. Створення їх єдиної класифікації [Текст] : автореф. дис. ... д-ра техн. наук : 05.02.02 / Конопльов Анатолій Васильович ; Одес. нац. політехн. ун-т. - O., 2013. - 39 с. : рис.)
- [15] J. Draper, Modern Metal Fatigue Analysis, Birchwood Park, Warrington: EMAS Pub, 2008.